UNIVERSIDADE FEDERAL DE SANTA CATARINA
PROGRAMA DE PÓS-GRADUAÇÃO EM
ENGENHARIA MECÂNICA

Deteção e Caracterização de Defeitos Internos por Termografia Infravermelha Pulsada

Tese submetida ao
Programa de Pós-Graduação em Engenharia Mecânica
Universidade Federal de Santa Catarina

para a obtenção do grau de
Doutor em Engenharia Mecânica

Fernando de Jesús López Rodríguez

Vicente de Paulo Nicolau, Dr. - Orientador
Departamento de Engenharia Mecânica
Universidade Federal de Santa Catarina

Xavier Maldague, PhD. - Co-orientador
Departamento de Engenharia Elétrica e Computação
Université Laval (Cidade de Quebec, QC, Canadá)

Florianópolis
Maio de 2014

UNIVERSIDADE FEDERAL DE SANTA CATARINA
PROGRAMA DE POS-GRADUAÇÃO EM
ENGENHARIA MECÂNICA

DETECÇÃO E CARACTERIZAÇÃO DE DEFEITOS INTERNOS
POR TERMOGRAFIA INFRAVERMELHA PULSADA

FERNANDO DE JESÚS LÓPEZ RODRÍGUEZ

Esta tese foi julgada adequada para a obtenção do título de
DOUTOR EM ENGENHARIA MECÂNICA
ESPECIALIDADE ENGENHARIA MECÂNICA
sendo aprovada em sua forma final.

Vicente de Paulo Nicolau, Dr. - Orientador

Xavier Maldague, PhD. (Université Laval) - Co-orientador

Armando Albertazzi Gonçalves Jr., Dr .Eng. - Coordenador do Curso

BANCA EXAMINADORA

Vicente de Paulo Nicolau, Dr. - Presidente

José Ricardo Tarpani, Dr. Eng. (USP/São Carlos) - Relator

Sérgio Damasceno Soares, Dr. Eng. (PETROBRAS)

Márcia Barbosa Henriques Mantelli, PhD. (UFSC)

Armando Albertazzi Gonçalves Jr., Dr. Eng. (UFSC)

Saulo Güths, Dr. (UFSC)

Detection and Characterization of Subsurface Defects by Infrared Pulsed Thermography

by

Fernando de Jesús López Rodríguez

This doctoral thesis was judged adequate as partial requisite to the degree of

Doctor in Mechanical Engineering

and approved on its final version by the Graduate Program of Mechanical Engineering

Vicente de Paulo Nicolau, Dr. - Advisor
Department of Mechanical Engineering
Federal University of Santa Catarina

Xavier Maldague, PhD. - Co-Advisor
Department of Electrical and Computer Engineering
Université Laval (Quebec City, QC, Canada)

Federal University of Santa Catarina
Florianópolis
May 2013

Acknowledgement

During those years working in my PhD I received the support from many people. To all of them I am deeply grateful.

I would like to express my sincere gratitude and appreciation to my supervisor and mentor, Professor Vicente Nicolau, for providing me the guidance, his caring and encouragement. In addition to his valuable advices, Professor Vicente taught me through his example the value of the humility and the reason.

I would also like to express special considerations to my co-supervisor, Professor Xavier Maldague, who provided me the opportunity to work in such a nice and professional environment. I enjoyed a lot our talks, which provided me a strong critical sense of the applications of infrared thermography.

I also want to extend my gratitude and appreciation to the thesis committee members for their time to read this dissertation and for their valuable recommendations that contributed for the enrichment of the final version of the Thesis.

I would like to thanks Dr. Clemente Ibarra-Castanedo, my friend from the MiViM, always willing to help, listen and discuss new ideas. Many thanks to Henrique Coelho Fernandes, my Brazilian colleague and friend, who since the beginning of my research internship in Canada offered me his friendship. Both of you contributed to the days - even with cold weather - were enjoyable. I also want to acknowledge my deep appreciation to Edevaldo Brandílio Reinaldo (from the LabTermo) for his sincere friendship and collaboration during my PhD.

I would like to thanks my colleagues from the LabCet - Renzo Figueroa, Alvaro Restrepo, Nury Nieto Garzón and Talita Possamai - for their contributions and recommendations during the preparation of the presentation.

I am very grateful with the Graduate Program of Mechanical Engineering (POSMEC) of the Federal University of Santa Catarina (UFSC) for the opportunity to grow up professional and as person. Thanks to the different Brazilian agencies that provided the financial support for my PhD, including the National Council of Scientific and Technological Development (CNPq) and the Sciences Without Borders Program (Programa Ciências Sem Fronteiras). I also want to acknowledge the Emerging Leaders in the Americas Program (ELAP) of the Foreign Affairs, Trade and Development Canada (FATD) who provided me the opportunity to participate in the research internship at Laval University in Quebec.

I would like to make a special mention to my parents: Fernando and Dalis. Your love, your care and support was the light that illuminated my path during this long journey. Thanks to my third mon, *minha Didiu*, for her kindness and for providing me the pleasant moments during my stay in Itabuna while I was working in the writing of the thesis. Thanks to my brother and sister, Cyntia and Fernando Javier, always beside me and giving me support and encourage.

Finally, I want to ex press my gratitude to my wife and inspiration. Rafaela, this work couldn't be possible without you, this work is also yours since you are my strength, you are my voice, you are eyes ...

Dedicatory

I dedicate this work to my mother-in-law, Thelma Y. Pinheiro.

Contents

List of Figures

List of Tables

Nomenclature

Greek Symbols	Quantity	Units
α	thermal diffusivity;	m^2/s
ε	emissivity	-
ε_o	vacuum permittivity	F/m
η	wavenumber;	cm^{-1}
θ	angle	rad
λ	wavelength	μm
μ	thermal diffusion length	μm
μ_o	vacuum permeability	N/A^2
ν	momentum diffusivity;	m^2/s
	electromagnetic wave frequency	Hz
π	Pi	-
ρ	density,	kg/m^3
	reflectivity	-
σ	Stefan-Boltzmann constant;	$W/(m^2 \cdot K^4)$
	standard deviation	-
τ	transmissivity	-
ϕ	volume fraction	-
ω	angular frequency;	rad/s
Ω	spatial direction	sr
δ	thickness	mm
∇	gradient	-

Latin Symbols	Quantity	Units
A	area	m^2
a	number of components	-
B	coefficient matrix	-
C	thermal contrast	^oC
	correlation coefficient	-
C_1	first radiation constant	$W \cdot m^2$
C_2	second radiation constant	$\mu m \cdot K$
C_3	third radiation constant	$\mu m \cdot K$
c	speed of light	m/s
c_o	speed of light in vacuum	m/s
c_p	specific heat	$J/(kg.\mathrm{K})$
D	lateral size	mm
d	diameter	mm
E	residual matrix	-
e	thermal effusivity;	$W/(m^2 \cdot K \cdot s^{1/2})$
	photon energy	eV
f	frequency	Hz
f_{blind}	blind frequency	Hz
f_s	sampling frequency	Hz
Fo	Fourier number	-
G	irradiation	W/m^2
H	height	m
h	Planck's constant;	$J \cdot s$
	convection heat transfer coefficient	$W/(m^2 \cdot \mathrm{K})$
I	radiation intensity	$W/(m^{-2} \cdot sr^{-1})$
i, j, k	grid points	-
J	radiosity	W/m^2
	Joules	

K	Kelvin - temperature scale	-
k	thermal conductivity	$W/(m.\mathrm{K})$
k_b	Boltzmann's constant	J/K
L	length	m
n	simple refractive index	-
	serial number of discrete data	-
Nu	Nusselt number	-
P	perimeter	m
	loading matrix	^oC
Pr	Prandlt number	-
q	heat rate	W
q''	heat flux	W/m^2
r	radius	m
r_H	radius of Gaussian distribution	m
Ra	Rayleigh number	-
S	thermographic signal	-
s	seconds	-
T	temperature	^oC or K
	score matrix	-
t	time	s
	score vector	
W	width	m
	weights matrix	-
$w(t)$	truncation window	m
z	depth	m
X	predictor matrix	-
x, y, z	Cartesian coordinates	-
Y	predicted matrix, fitted response	-

Subindex

abs	absorved
amb	ambient
ar	air
atm	atmosphere
b	blackbody
cam	camera
$comp$	component
$cond$	conduction
$conv$	convection
d	defect
e	energy-derived
eff	effective
exp	experimental
f	final, fiber
i	incident
lat	lateral
$lock-in$	modulated
low	lower
λ	spectral-dependence
m	matrix
mat	material
max	maximum
N	total data elements
n	single data element
new	new
o	initial
old	old
$omset$	onset
P	current point

ref	reflected
rad	radiation
s	surface
sa	sound area
sim	simulated
upp	upper
t	transmitted
θ	directional-dependence
$\parallel$	parallel
$\perp$	perpendicular

Acronyms

CFRP	Carbon Fiber Reinforced Polymer
CVSL	Computer Vision System Laboratory
DAC	Differential Absolute Contrast
DFTM	Discrete Fourier Transform
DWT	Discrete Wavelet Transform
FFT	Fast Fourier Transform
FPA	Focal Plane Array
FRP	Fiber Reinforced Polymer
FVM	Finite Volume Method
GFRP	Glass Fiber Reinforced Polymer
IR	Infrared
IRT	Infrared Thermography
LT	Lock-in Thermography
LV	Latent Variable
LWIR	Long Wavelength Infrared
MLR	Multivariate Linear Regression
MRI	Magnetic Resonance Imaging
MWIR	Medium Wavelength Infrared
MIVIM	Multipolar Infrared Vision Multipolaire
NIR	Near Infrared
NDT	Nondestructive Testing
NDT&E	Nondestructive Testing and Evaluation
NIPALS	Nonlinear Iterative Partial Least Squares
NIR	Near Infrared
PCR	Principal Component Regression
PCT	Principal Component Thermography
PDE	Partial Differential Equation
PLSR	Partial Least Squares Regression
PPT	Pulsed Phase Thermography

PT	Pulsed Thermography
PPT	Pulsed Phase Thermography
RMSE	Root Mean Square Error
SNR	Signal-to-Noise Ratio
SWIR	Short Wavelength Infrared
TSR	Thermographic Signal Reconstruction
TNDT	Thermal Nondestructive Testing
VLWIR	Very Long Wavelength Infrared
VT	Vibrothermography
WT	Wavelet Transform

Resumo

A termografia pulsada (TP) é uma técnica promissora para a avaliação não-destrutiva de materiais. O protocolo de inspeção consiste na aplicação de um pulso térmico no espécime e monitorar a resposta térmica da superfície via radiação infravermelha (IV). Descontinuidades internas aparecem na sequência térmica como 'hot spots' ou padrões térmicos irregulares, os quais são prodruzidos por alterações na taxa interna de difusão de calor. Apesar de ser uma das técnicas mais usadas e atrativas para a avaliação não-destrutiva, sua aplicação apresenta grandes desafios especialmente durante a inspeção de materiais anisotrópicos. 'Blurring', a perda de visibilidade devido aos efeitos da condução lateral de calor e a não-uniformidade produzida durante a excitação térmica representam as maiores limitações da TP. Esta tese é focada na otimização da inspeção por TP em laminados compósitos. Para tal propósito, foi desenvolvido um modelo termo-numérico para a análise da resposta térmica da material devido a presença de defeitos internos. Um estudo paramétrico foi desenvolvido com o objetivo de estudar o impacto do aquecimento não-uniforme, da intensidade da radiação e da geometria dos defeitos em vários parâmetros informativos da inspeção por TP. Uma análise das três técnicas mais usadas para o tratamento de sinais termográficos foi realizada e os seus desempenhos foram avaliados em função da relação sinal-ruído no ponto de maior contraste entre região com defeito e região sem defeito. Neste trabalho foi desenvolvida uma nova técnica de processamento e análise de imagens térmicas. A nova técnica – baseada no método de regressão dos mínimos quadrados parciais (PLSR) – de-

compõe a sequência térmica em variáveis latentes, permitindo assim a separação das diversas fontes de ruído que afetam a qualidade das imagens. A partir deste método de correlação foi desenvolvido um modelo empírico para a quantificação da profundidade e tamanho lateral dos defeitos empregando dados experimentais. Ambos os métodos - de tratamento de sinais e quantificação de defeitos - foram analisados e comparados com técnicas tradicionais, apresentando uma melhoria substancial na relação sinal-ruído e na precisão no processo de inversão de profundidade e forma dos defeitos.

Palavras-chave: termografia pulsada; simulação térmica; materiais compósitos; análise quantitativa; tratamento de sinais termográficos.

Abstract

Pulsed thermography (PT) is a novel and promissory technique for the nondestructive and evaluation (NDT&E) of materials. The inspection protocol consists in pulse heating the specimen while monitoring the resulting thermal response via infrared (IR) radiation. Subsurface discontinuities appear as transient hot spots or irregular thermal patterns in the thermogram sequence, which are produced by the alterations in the internal heat diffusion fluxes. In spite of being one of the most used and attractive methods for the NDT&E, its application still presents challenges specially when inspecting anisotropic materials. 'Blurring', the lost of defect visibility due to the effects of lateral heat conduction and the non-uniform heating produced during the application of the thermal excitation, represent the major drawbacks of PT. This thesis is focused on the optimization of the PT inspection of laminated composites. A thermal-numerical model is developed in order to analysis the thermal response of the material due to the presence of subsurface defects. A parametric study was performed aiming to study the impact of the effects of non-uniform heating, irradiation density and defects geometry on several informative variables of the PT inspection. An in-depth analysis of three of the most used PT sinal processing techniques was carried out and their performance was evaluated in terms of the signal-to-noise (SNR) at maximum signal contrast. In this work was also developed a new promissory technique for the processing and analysis of thermographic data. The new method - based on partial least squares regression (PLSR) - decomposes the thermal sequence into latent variables, allowing to separate several sources of

noise affecting the quality of the images. From the statistical correlation method an empirical model was developed for the quantification of the depth and lateral size of defects using experimental data. Both methods - for the signal processing and for the inversion of depth and lateral size - were analyzed and compared with traditional techniques, achieving a substantial improvement in the signal-to-noise ratio and in the accuracy in the prediction results of depth and lateral size of the defects.

Keywords: pulsed thermography; thermal simulation; composites materials; quantitative analysis; thermographic signal processing.

Resumo Estendido em Português

Sobre a Termografia Infravermelha Pulsada

A termografia infravermelha, como técnica de ensaios não-destrutivos (ENDs), é dividida em dois grupos − termografia passiva e termografia ativa − a qual depende do uso ou não de uma excitação externa para produzir um fluxo de calor no interior do material em estudo. Atualmente existem vários tipos (óptica, mecânica e eletromagnética) e modos (pulsada, modulada e burst) de excitação externa, cada um possuindo diferentes rendimentos em função do tipo de material. Este trabalho está focado nas técnicas de termografia ativa que empregam excitação óptica, especificamente, a termografia pulsada (TP).

Ao contrário da outras técnicas em que a função de excitação temporal é da ordem de vários segundos, minutos ou inclusive dias, a termografia pulsada utiliza um pulso térmico de curta duração ($\sim 10^{-3}$ s) o qual é aplicado no material, enquanto o subsequente processo de resfriamento é monitorado utilizando uma câmera infravermelha. A Figura 1 mostra os princípios básicos da termografia pulsada. O processo de inspeção inicia com a aplicação do pulso térmico - através da transferência de calor por radiação - no corpo de prova (sinal de entrada ou input signal). A quantidade de energia absorvida pela superfície do material cria uma frente térmica que se propaga por condução no seu interior até encontrar defeitos internos, alterando desta forma a taxa de difusão de calor. A iteração entre o fluxo de calor e as irregularidades internas - regiões com propriedades termofísicas distintas ao do resto material - produz um comportamento

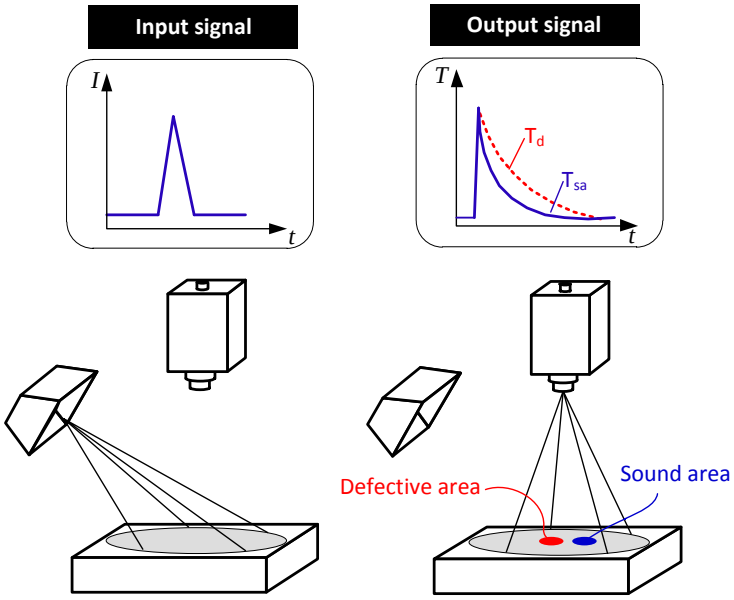

Figure 1: Princípios da termografia pulsada como técnica de ensaios não-destrutivos.

irregular na curva de decaimento térmico durante o processo de resfriamento, observado através da câmera infravermelha (sinal de saída ou output signal). A inspeção por termografia pulsada é desenvolvida em regime transiente (em contraste com a termografia modulada a qual é implementada em regime permanente) possibilitando assim a análise dos dados obtidos de forma rápida e direta.

A TP possui várias vantagens, sendo as mais importantes sua rapidez e facilidade, assim como sua capacidade de ser aplicada em vários tipos de materiais. Entretanto, devido à natureza do processo de medição, os sinais adquiridos com a câmera infravermelha estão quase sempre contaminados com sinais de ruídos e artefatos das reflexões externas, variação de emissividade e não-uniformidade na radiação aplicada sobre o material. Esta última é um problema inevitável da configuração do sistema de radiação e é provavelmente o mais prejudicial fator que afeta negativamente a ad-

equada detecção de defeitos. Por esta razão, o processamento de sinais termográficas representa a linha de frente para reduzir os efeitos negativos das distintas fontes de ruído e especialmente, da excitação não-uniforme.

Motivações

Apesar de ser uma das técnicas mais promissoras para a avaliação não-destrutivas de materiais, a TP apresenta limitações especialmente na inspeção de materiais anisotrópicos. Devido à natureza física do processo de mediação, a TP está altamente contaminada por diversas fontes de ruídos, tais como reflexões do ambiente, variação da emissividade do material e a não-uniformidade decorrente da aplicação da excitação térmica. Adicionalmente, a perda de visibilidade dos defeitos devido aos efeitos da difusão de calor nas laterais, constitui mais uma limitação para a detecção de defeitos mais profundos. Este fenômeno é conhecido como 'bluring" e afeta principalmente os defeitos que requerem um maior tempo de observação para serem detectados.

O mencionado anteriormente representa só um exemplo das dificuldades que a TP enfrenta. A análise da técnica é complexa e envolve muitas variáveis. Por esta razão exista a necessidade de examinar e estudar os diversos mecanismo que possam ajudar a diminuir os efeitos da excitação não-uniforme e da perda de visibilidade devido à condução de calor nas laterais. Geralmente a abordagem experimental não é a mais adequada para realizar uma análise profunda de como as variáveis mais importantes da TP são afetadas pelos fenômenos já mencionados. Neste contexto, a abordagem numérica constitui uma importante ferramenta para estudar os diferentes processos que participam durante o ensaio térmico, e concluir, na base de conceitos físicos, o caminho a seguir para melhorar a performance desta técnica.

A maioria dos modelos matemáticos disponíveis na literatura para a análise teórica da TP estão baseados na solução analítica da equação de condução de calor em 1D. Infelizmente, estes modelos simplificados não reproduzem com precisão os diferentes processos que se dão durante o

ensaio térmico. Adicionalmente, existe a necessidade de formular apropriadamente a anisotropia do material, sendo os modelos disponíveis de hoje limitados a casos em que as propriedades termofísicas do material são homogêneas.

Outro ponto-chave da termografia pulsada é o processamento de sinais. A inspeção por TP é limitada na sua forma básica à defeitos rasos. A análise quantitativa usando imagens sem processar dificulta o processo de recuperação da profundidade e geometria dos defeitos. Por esta razão, o processamento de sinais termográficas é um dos assuntos que recebe uma especialmente atenção neste trabalho. Atualmente existem diversos algoritmos para o processamento das imagens térmicas obtidas no processo de inspeção. As técnicas mais usadas estão baseadas na solução da equação 1D de condução de calor: contraste absoluto diferencial (DAC), reconstrução de sinais termográficas (TSR) e termografia de fase pulsada (PPT). Apesar da melhoria na qualidade das imagens obtidas após a aplicação destas técnicas, seu escopo de aplicação esta restrito a casos em que o processo de condução de calor é 1D.

Objetivos

O objetivo geral desta tese é otimizar a capacidade de inspeção por termografia pulsada, para detectar e caracterizar defeitos internos em materiais compósitos, a partir da análise térmica, do processamento de sinais e da análise quantitativa. Para atingir esta meta, os seguintes objetivos específicos são definidos:

1. Revisar os conceitos fundamentais da termografia pulsada como técnica de END de materiais, colocando especial atenção as limitações da técnica na inspeção de materiais anisotrópicos;

2. Desenvolver, testar e validar experimentalmente uma ferramenta computacional com o objetivo de analisar a processo de difusão interno de calor e a resposta térmica da superfície devido à presença de defeitos;

3. Identificar através de um estudo paramétrico, as variáveis mais sensitivas à excitação não-uniforme, intensidade da radiação e características associadas aos defeitos internos;

4. Realizar uma revisão crítica das técnicas de processamento de imagens em TP e desenvolver uma metodologia para avaliar o desempenho destas técnicas;

5. Desenvolver um método robusto de processamento de imagens utilizando o método de regressão dos mínimos quadrados parciais e avaliar o seu desempenho usando a metodologia desenvolvida no Capítulo 4.

6. Desenvolver uma metodologia para a análise quantitativa de defeitos internos (inversão de profundidade e tamanho lateral) empregando o método dos mínimos quadrados parciais e avaliar o desempenho através da comparação com técnicas empregadas hoje em dia para tal fin.

Metodologia e Organização da Tese

Este trabalho está focado na otimização da inspeção por termografia pulsada. A metodologia desenvolvida para tal propósito consistiu em uma abordagem teórica e uma experimental. A abordagem teórica foi focada no desenvolvimento de uma ferramenta numérica utilizada para simular a inspeção de materiais compósitos por termografia pulsada. Através da simulação numérica foi estudado e analisado primeiramente o processo de difusão de calor decorrente da aplicação da excitação no material e a resposta térmica da superfície devido à presença de defeitos internos. Esta análise foi particularmente importante devido a que até então, não se tinha instrumentos laboratoriais para reproduzir um pulso térmico de alta potência e curta duração. Uma vez os conceitos físicos da TP foram compreendidos adequadamente, a seguinte etapa consistiu na identificação dos parâmetros mais importantes durante o processo de resfriamento. Estes parâmetros (máximo contraste térmico, tempo de ocorrência do contraste

máximo e tempo de início de aparição dos defeitos) foram exaustivamente estudados com o objetivo de determinar os mais sensitivos aos efeitos da excitação não-uniforme.

Graças ao Acordo de Cooperação entre a Universidade Federal de Santa Catarina e Laval Université (em Cidade de Quebec, QC, Canadá) foi possível realizar um estágio de pesquisa no Canadian Research Chair Multipolar Infrared Vision. Durante este estágio foi desenvolvida a abordagem experimental desta pesquisa além da validação da ferramenta computacional. Também foi possível atualizar o algoritmo numérico com informação detalhada dos corpos de prova disponíveis no laboratório. Durante a abordagem experimental foi dada especial atenção à necessidade do processamento de sinais termográficos com o objetivo de melhorar a visibilidade dos defeitos bem como para a posterior etapa de análise quantitativa. Nesta etapa foram analisadas diferentes técnicas de processamento de imagens térmicas e foi desenvolvida e implementada com êxito uma nova técnica de tratamento baseada no método de regressão dos mínimos quadrados parciais.

Esta tese é dividida em seis capítulos principais e dos apêndices. O Capítulo 2 se apresentam os conceitos fundamentais da termografia como técnica de inspeção e avaliação não-destrutiva bem como os aspectos teóricos mais relevantes da termografia pulsada, o sistema de inspeção e a aquisição e análise de sinais. Neste capitulo também é feita uma análise das maiores limitações da termografia pulsada, utilizando o enfoque térmico.

O Capítulo 3 trata sobre a simulação do ensaio por TP. Primeiramente é apresentada uma revisão bibliográfica dos modelos matemáticos utilizados atualmente para o estudo teórico da TP. Seguidamente é desenvolvido um modelo termo-numérico e uma metodologia para a simulação computacional do ensaio por TP em materiais compósitos. O modelo proposto está baseado na equação de condução de calor para meios anisotrópicos em 3D e regime transiente e a solução foi realizada utilizando o Método dos Volumes Finitos. Um estudo paramétrico foi realizado com o obje-

tivo de estudar os efeitos na não-uniformidade da excitação, intensidade da irradiação e geometria dos defeitos em variáveis informativas obtidas durante o processo de resfriamento.

O Capitulo 4 apresenta uma revisão geral de métodos de processamento de sinais aplicados aos ensaios térmicos não-destrutivos além de uma análise crítica dos métodos mais usados para o processamento de imagens por TP. Neste capítulo foi desenvolvida uma metodologia para estudar o rendimento das técnicas DAC, TSR e PPT (respetivamente, differential absolute contrast, thermographic signal reconstruction e pulsed phase thermography). A metodologia de avaliação calcula a relação sinal-ruído no máximo nível de contraste do sinal de vinte e cinco defeitos antes e depois do processamento. Foram analisados imagens térmicas obtidas experimentalmente através do ensaio por TP em corpos de prova de fibra de vidro e fibra de carbono. As vantagens e limitações das técnicas em questão foram também discutidas neste capítulo.

No Capítulo 5 o método de regressão dos mínimos quadrados parciais (PLSR) é proposto como uma nova técnica de processamento de imagens térmicas obtidas por TP. Os conceitos fundamentais e a formulação matemática do PLSR são apresentados, bem como a metodologia para a aplicação à inspeção não-destrutiva por TP. Dentro deste capítulo foi realizada uma análise exploratória das variáveis latentes obtidas através do processo de regressão, permitindo desta forma um estudo mais profundo da correlação entre as variáveis e amostras. O desempenho da nova técnica de processamento de sinais foi avaliada empregando a metodologia previamente desenvolvida no Capítulo 4.

O Capítulo 6 apresenta um novo método de inversão da profundidade e tamanho lateral dos defeitos internos. Uma revisão e análise dos métodos usados atualmente para a quantificação de defeitos internos é apresentada. Na sequência, os fundamentos da nova técnica de quantificação são apresentados e aplicados na determinação da profundidade e tamanho lateral através de dados experimentais e numéricos do corpo de prova de fibra de carbono. Os valores obtidos com o novo método são comparados com

valores calculados empregando o método proposto por Balageas et al. (1987), o qual correlaciona a profundidade dos defeitos com o máximo nível de contraste térmico.

As conclusões, contribuições e as recomendações para trabalhos futuros são apresentados no Capítulo 6.

Chapter 1

Introduction

1.1 Background: Infrared and Thermal Testing

Nowadays the term *quality control* gains more importance in an increasingly competitive market, controlled by the globalization of services and products. Additionally, safety and reliability are key-issues on constant demand especially in products which involve the life of thousands of people. These facts has brought the necessity to promote the development of techniques and methods to guarantee the market superiority, not only in terms of quality, but also in terms of productivity. In this scenario, nondestructive testing and evaluation (NDT&E) techniques play an important role in the complex task of continuously improving the quality of products and processes.

Nondestructive testing (NDT) is defined as an examination, test, or evaluation performed on any type of test object without changing or altering its physical integrity, in order to determine the absence or presence of conditions that may have an effect on the usefulness or serviceability of that object (Hellier, 2003). In NDT, as opposed to those methods that subject the specimen to large amounts of stress and measure its resistance, the determination of the presence −or not− of defects is done through complex analysis that requires multiple stages of information processing. NDT techniques can be classified into seven major categories (Hung et al., 2009):

1. Visual (visual inspection using borescope);
2. Penetrating radiation (X-ray and neutron imaging);
3. Magnetic-electrical (magnetic particles, Eddy current);

4. Mechanical vibration (ultrasonic, acoustic emission);
5. Chemica/electromechanical (chemical spot testing);
6. **Infrared and thermal testing (infrared thermography);** and
7. Other optical methods (interferometry, holography and shearography).

Each category and method can be completely characterized in terms of five principal factors: (1) energy source or medium used to probe object (such as X-rays, ultrasonic waves and thermal radiation); (2) nature of the signals, image and/or signature resulting from interaction with the object (attenuation of X-rays or reflection of ultrasound, for example); (3) means of detecting or sensing resultant signals (photoemulsion, piezoelectric crystal or inductance coil); (4) method of indicating and/or recording signals (meter deflection, oscilloscope trace or radiograph); and (5) basis for interpreting the results (direct or indirect indication, qualitative or quantitative and pertinent dependencies).

As a NDT technique, infrared and thermal testing (which are of the major concern in this thesis) involve the measurement (by noncontact means such as infrared thermometers, infrared line scanners and infrared thermal imaging/equipment) and subsequent analysis of the emitted IR thermal radiation - energy that emit all the bodies with $T > 0\,K$ ($-273.15\,^{o}C$) - to predict and evaluate the presence of anomalies within a certain material specimen. The techniques in this category are known as thermal nondestructive testing (TNDT) methods. The term TNDT refers internationally to the detection of subsurface defects in materials using transient or, more rarely, steady-state one- and two-side procedures (Vavilov, 1992) and includes several measurement techniques. The application of these techniques require a fundamental knowledge of heat transfer and the thermal behaviour of materials in order to understand the significance of temperature changes on a test sample.

Figure 1.1 shows the TNDT techniques associated to the IR spectrum band. Each technique is characterized by a particular thermal phenomena and depends on the wavelength associated with the radiation emitted by the object under study. This thesis is concerned to infrared thermography (IRT), which is a noncontact and real-time sensing method that provides the surface temperature through the measurement of the IR radiation emitted by the material surface (Maldague, 2001).

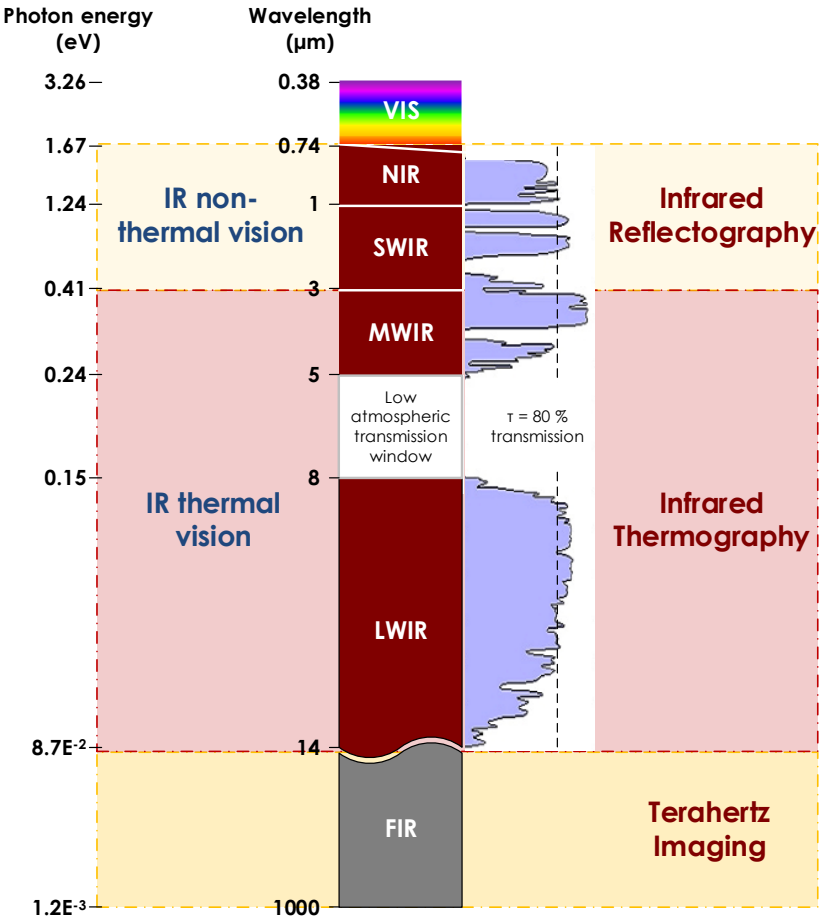

Figure 1.1: IR bands in the electromagnetic spectrum and sensing techniques associated to each IR region. IRT corresponds to the mapping of the surface temperature through the measurement of IR radiation. Adapted from López et al. (2013)

The basis of IRT is the analysis of contrasts in the temperature field which are produced by alterations in the internal heat flux. These irregular patterns of the surface thermal maps allow the detection and characterization of internal anomalies, such as cracks, delamination and voids. As will be discussed in next section, IRT can be deployed using two approaches: passive and active thermography.

1.2 Active Infrared Thermography for the NDT&E

As a NDT technique, IRT is divided in two groups: passive and active thermography. In *passive thermography approach*, no external stimulation is employed to provoke a heat flux within the material. Its analysis is based on abnormal temperature behaviors that reveal potential problems, and a key term is *temperature difference* with respect to a reference or *hot spot* (Maldague, 2001). Meanwhile, in *active thermography approach*, an external stimulation is induced to the material in order to produce a heat diffusion flux within the sample test. As depicted in Figure 1.2, currently exist several methods of external stimulations used to provoke the internal heat flux. Each method has its own particularity in terms of application scope and the way how the information is processed and analyzed.

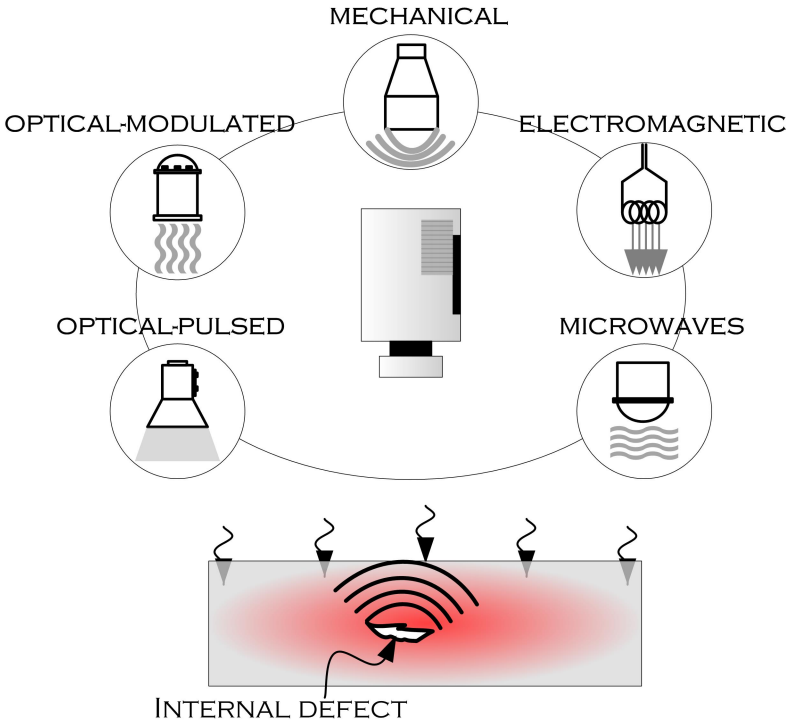

Figure 1.2: Current state of the art of excitation methods in active thermography for the NDT&E of materials.

In general terms, the excitation methods in active IRT can be categorized into four major groups: mechanical, electromagnetic, microwave and optical excitation. From these methods, mechanical and optical excitation stand as the most traditional excitation sources for IRT due to their simplicity and scope of applications. In mechanical stimulation a transducer is used to inject mechanical vibrations in the form of ultrasound waves to the specimen. Due to the direct conversion from mechanical to thermal energy, heat is released by friction precisely at locations where defects as cracks and delaminations are located (Maldague, 2001). There are basically two configurations using mechanical excitation: lock-in vibrothermography (or amplitude modulated VT) and burst vibrothermography (Ibarra-Castanedo et al., 2007b).

On the other hand, in optical excitation methods thermal energy is delivered to the specimen − via radiation heat transfer − by means of optical devices, such as photographic flashes (for pulsed heat stimulation) and halogen lamps (for periodic heating) (Ibarra-Castanedo et al., 2009). Once the thermal energy is absorbed by the material surface, a thermal front propagates trough the specimen by heat diffusion until it reaches discontinuities − regions having different thermal properties than the surroundings − affecting the heat flux rate and producing abnormal thermal patterns on the surface which are monitored via IR radiation. Within this category, pulsed thermography (PT) is one of the most attractive technique for the NDT&E of materials. One reason for this is the quickness of the inspection in which a short thermal stimulation pulse lasting from a few milliseconds for high-conductivity materials to a few seconds for low-conductivity specimen is used (Maldague, 2001). The application of this technique to inspect composites materials represents the core of this thesis.

Besides PT, lock-in thermography (LT) is also one of the techniques belonging to the group that uses thermal excitation. In this method the specimen is submitted to a periodical excitation while monitoring the resulting temperature field. The *lock-in* refers to the necessity to monitor the exact time dependence between the resulting temperature signal and the reference input signal (the modulated heating). Contrary to PT, LT is deployed in steady-state regime and its principal attraction is the analysis in the frequency domain and plase delay images (or phasegrams). It has been reported that phasegrams are less affected by reflections from the environment, emissivity variations and non-uniform heating (Ibarra-Castanedo et al., 2009; Maldague and Marinetti, 2002).

1.3 Motivations

In spite of being one of the most promissory techniques for the NDT&E of materials, the inspection by pulsed thermography still presents great challenges specially when inspecting highly-anisotropic specimens such as composite materials. Due to the physical nature of the measurement process, PT is highly sensitive to external reflections, emissivity variations and also non-uniform heating caused during the application of the external excitation. Non-uniform heating is probably the major drawback of the PT inspection and it is an unavoidable problem in the configuration of the irradiation sources. Moreover, the lost of defect visibility due to the effects of lateral heat diffusion constitutes a restriction in the depth probing capabilities of PT (Balageas, 2011). This phenomenon is known as blurring and is associated to longer observation times (affecting deeper defects), when takes place the transition from a wider (1D-like) to a narrower heat diffusion process (3D-like).

The mentioned above represents just an example of the difficulties that PT has to deal with. The analysis is complex and involve several variables. There is therefore the necessity to examine and study the different mechanisms that could help to overcome the harmful effects of non-uniform heating and blurring. Mostly, the experimental approach is not the most suitable to perform an in-depth study of how important variables in PT (such as thermal contrast and onset time) are affected by the phenomenons already mentioned. In this context, numerical approach represents a means to address the most important processes and variables that take place during the PT inspection and to conclude in terms of physical-based concepts, the path to increase the performance of this promissory technique.

Most of the mathematical models currently available in the literature for the theoretical analysis of the PT inspection are based on the analytical solution of the 1D (Chatterjee et al., 2011; Lau et al., 1991; Mayr et al., 2011) and 2D (Omar and Zhou, 2008) heat conduction equation. Unfortunately, these are simplified models that do not reproduce with accuracy the different physical processes involved during the thermal inspection. Moreover, there is a lack of information in regard to the mathematical formulation of the material anisotropy, limiting the analysis to cases when the thermophysical properties of the material are homogeneous.

Another key-issue in PT is the signal processing. The inspection by PT is in its basic form, generally limited to qualitative applications on large, near-surface defects. Performing quantitative analysis using raw data is a difficult - if not impossible - task. For this reason signal processing is one of topics that has received more attention and has been investigated extensively over the years. Currently exits several techniques applied to processing PT data with a wide range of reported effectiveness. The most used and traditional techniques are derived from the 1D solution of the heat conduction equation: differential absolute contrast (Pilla et al., 2002), thermographic signal reconstruction (Shepard, 2001) and pulsed phase thermography (Maldague and Marinetti, 2002). In spite of the improvement in the image quality with these techniques, their span of applicability is restricted to the cases where the heat conduction regime is 1D.

1.4 Research Objectives

The main objective of this thesis is stated as follows: *to optimize the capabilities of the pulsed thermography inspection, to detect and characterize subsurface defects in laminated composites*.

In order to achieve this goal, the author has defined the following specific objectives:

1. Review the fundamental concepts of pulsed thermography for the NDT&E of materials, with particular emphasis on the limitations when inspecting anisotropic specimens (Chapter 2);

2. Develop, test and validate experimentally a computational tool aiming to analyse the heat diffusion process and the surface thermal response due to the presence of internal defects (Chapter 3);

3. Perform a parametric study aiming to identify the most sensitive variables to non-uniform heating, radiation intensity and characteristics associated to the subsurface defects (Chapter 3, section 3.5.1);

4. Provide a critical review of the most used processing methods for PT data and to develop a methodology to study the performance of these techniques (Chapter 4, sections 4.2 to 4.3);

5. Develop a robust processing method for PT data using partial least squares regression (PLSR) and evaluate its performance using the methodology proposed in Chapter 4 (Chapter 5);

6. Propose and test a methodology for the quantitative analysis of subsurface defects (inversion of depth and lateral size) using PLSR and evaluate its performance over traditional methods currently available (Chapter 6).

1.5 Methodology and Thesis Organization

This works focuses on the optimization of the PT inspection. The methodology carried out to perform this task consisted on two approaches: theoretical and experimental approaches. The theoretical approach was concerned to the development of the numerical model, which was used to simulate the PT inspection on laminated composites. Through numerical simulation, it was first studied the heat diffusion process resulting from the thermal excitation of the material and then analyzed the response of the surface thermal pattern due to the presence of internal defects. This analysis was particulary important since until then, there were not available experimental instruments to reproduce a high-power short thermal pulse. Once the physical concepts of the PT inspection were understood, the next stage was to identify the most important parameters that arise from the cooling process regime followed the thermal excitation. These parameters were exhaustively studied in order to determine the most sensitive to the harmful effects of non-uniform heating.

Thanks to a cooperation agreement between *Universidade Federal de Santa Catarina* and *Laval University* (in Quebec City, Canada) it was possible to perform a research internship at the Canadian Research Chair Multipolar Infrared Vision. The experimental approach was carried out during this research internship and also it was validated the computational tool. Moreover, it was updated the algorithm with more detailed information concerning to the specimens. Special attention was paid to the necessity of processing the PT raw data in order to enhance defect visibility and also for further analysis (such as defect characterization). During this stage, the different processing methods were analysed and applied to experimental data. The application of a statistical regression technique (PLSR) as a signal processing method was also considered and successfully implemented.

This memory is divided into six main chapters and two appendixes. Chapter 2 is concerned to the fundamentals concepts of pulsed thermography as a nondestructive testing and evaluation technique. In this chapter are addressed theoretical aspects of the technique as well as the experimental setup and the acquisition and analysis of the data. This chapter

also presents the inspection system used during the experimental approach of this thesis and put into discussion the major drawbacks of the PT inspection.

Chapter 3 is concerned to the simulation of the PT inspection. First is presented a bibliography review concerning to the state-of-art of mathematical models applied to the study of the PT inspection. Then is developed a thermal-numerical model and a methodology for the computational simulation of the PT inspection on laminated composites. The proposed model is based on the 3D heat conduction equation for anisotropic medium and the solution was carried out using the finite volume method (FVM). A parametric study was performed aiming to study the effects of non-uniform heating, irradiation density and defects geometry on several informative variables of the PT inspection.

Chapter 4 provides a review of the current methods for data processing in thermal nondestructive testing and an in-depth analysis of three of the most attractive processing techniques for PT data. The theoretical aspects of each technique are revised as well as their application to PT data. This chapter also presents a methodology to study the performance of each technique. The methodology computes the signal-to-noise ratio at maximum signal contrast of twenty-five signals (one for each defect) before and after the application of the processing techniques to the PT raw data. The advantages and limitations of each technique are also discussed in this chapter.

In Chapter 5 the regression method partial least squares is proposed as a new technique for the processing of PT data. The fundamentals concepts and mathematical formulation of PLSR are first reviewed and then, the application to PT is presented. Special attention is given to the analysis of the latent variables of the reconstructed sequence. This analysis will provide insights for the enhancement of the detection capabilities of PT. The performance of the new processing method is evaluated in terms of SNR at maximum signal contrast, using the same methodology developed in Chapter 4.

Chapter 6 presents a new method for retrieving depth and lateral sizes of defects. A review and analysis of the current methods to characterize subsurface defects is presented and then are exposed the fundamental concepts of the new technique for quantitative analysis. Interestingly, this new method results from the integration of numerical and experimental results and also, represents an extension of PLSR to the analysis of PT data. In order to evaluate the performance of the proposed inversion

method, quantitative results obtained from the new method are compared when to the obtained with one of the most traditional procedures in pulsed thermography.

The conclusions, contributions and recommendations for future works are presented in Chapter 7.

Chapter 2

Fundamentals and Application of Pulsed Thermography

This chapter attempts to address the most relevant concepts concerned to pulsed thermography as a NDT&E technique. The discussion begins with the basic theory behind the pulsed thermography inspection followed by the experimental setup, the acquisition and analysis of the thermographic signals obtained during the inspection process. Special emphasis will be placed on the drawbacks of this technique, such as non-uniform heating and lateral heat diffusion. Furthermore, this chapter will also present the experimental system and relevant information concerning to the specimens used during the development of the research.

2.1 Fundamentals of Pulsed Thermography

The application of infrared thermography has received vast and growing attention for diagnostics and monitoring in the last few decades. This is mainly due to the fact that commercial infrared or thermal cameras, the main instrument for performing infrared thermography are continuously improving in both, sensibility and in spatial resolution, and they are getting faster and relatively less expensive. In similar manner, the computational resources required for control, data acquisition, storage and processing are continuously updated, providing thus more computing power to perform complex processing tasks. These factors have revolutionized the NDT inspection methods, furnishing more reliable results and widening the application scope of these techniques. As a matter of fact, pulsed thermography is one of these technique that has emerged from the continuous improving of both - IR cameras and computational resources.

PT is based on the application − via radiation heat transfer − of a short and high power thermal pulse ($\sim 10^{-3}$ s) to the specimen surface. This energy is then absorbed by the material surface and converted into heat, triggering the creation of a thermal front which propagates through diffusion within the material. The interaction of heat diffusion between regions having different thermal properties will produce dissimilar behaviors of the temperature decay during the cooling process, which can be observed with an infrared camera. This approach is characterized in transient regime − contrary to lock-in thermography in which its deployment is carried out in steady-state condition − providing thereby a fast and straightforward acquisition. Moreover, the brief heating (generally a few degree above the initial component temperature) prevents damage to the component.

Figure 2.1 shows the necessary steps that should be performed for the proper implementation of PT as a nondestructive testing and evaluation technique. A pre-analysis stage is conceived to assess characteristics associated to the material under study. Consideration concerned to the shape and thermophysical properties of the material, ambient conditions and instrumentations should be accounted. Computational simulation represents a valuable tool to perform an in-depth analysis of the expected material response due to the applied thermal excitation. Once the pre-analysis stage is concluded, the next step consists on the system excitation, which is applied in order to generate a thermal contrast on the surface thermal pattern. In general terms several experiment must be conducted in order to produce a strong (and reliable) enough signal which leads to the detection of internal defects.

Signal processing is a necessary step in order to enhance defect visibility. Through the application of different methods to the obtained thermal sequence it is possible to eliminate most of the background noise produced by non-uniform heating and external artifacts (from external reflections and emissivity variations). Furthermore, the ‘de-noising’ of the temporal signals constitutes an important achievement when processing the thermographic signals. It is important to mention that signal processing also improve the depth proving capabilities of the inspection. Defects with a reduced thermal contrast (often the deeper defects) are the most sensitive to spatial noise.

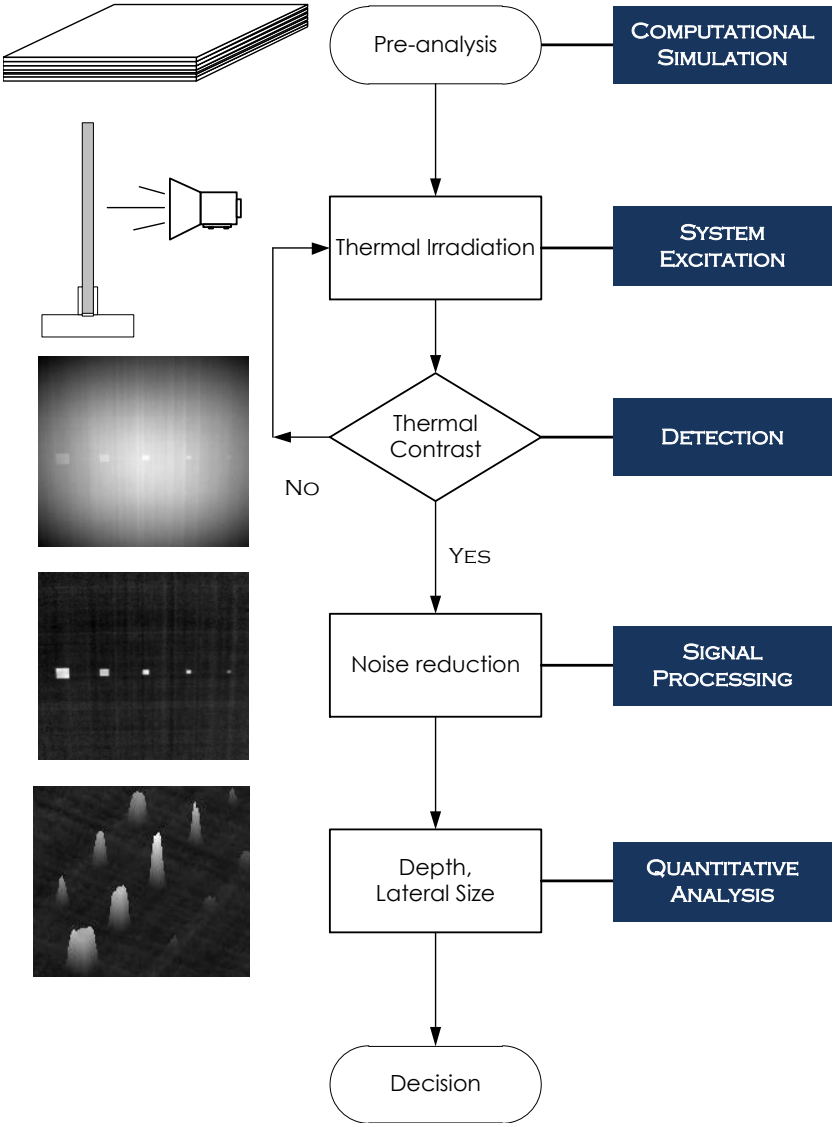

Figure 2.1: Process chain in NDT&E by pulsed thermography.

Once the defects has been detected, the next step is the characterization of the internal anomalies. This step is necessary since it will provide the basis for the actions (or decisions) to be taken: rejection or reparation (replacement or other). The depth and shape of the defects are often the variables to be assessed. However, other parameters such as thermal resistance (Krapez et al., 1991) or thermophysical properties (Rodriguez and Nicolau, 2012) can be identified.

2.1.1 Advantages and disadvantages of PT

All NDT techniques - depending on their applications - present advantages and limitations. In the case of PT, some of the advantages are its **fast** inspection rate; **contactless**, no coupling is need as in the case of conventional ultrasound and vibrothermography, both methods require a coupling media between the transducer and the specimen. It is also important to mention that in induction thermography (IT) the coils have to be relatively close to the inspected surface. **Security** of personal is another important advantage of PT since there is no harmful radiation involved as in the case of X-ray radiography; and the **imaging** capabilities, in which the results are relatively easy to interpret since they are (often) obtained in image or video formats (Ibarra-Castanedo et al., 2007b; Maldague, 2001);

On the other hand, one of the main disadvantages of PT compared to other NDT techniques is the **cost** associated to the IR equipments (IR camera and thermal stimulation units). In this context, the inspection by PT is relatively more expensive than others NDT techniques, such as visual inspection and ultrasound. Furthermore, the detection capabilities of PT are limited to defects resulting in a measurable change of the **thermal properties** from the inspected surface. Another comparison can be made in regards to the acquisition and analysis of pulsed and lock-in thermography (both techniques using optical stimulation). PT is fast - only a few seconds are required to perform the acquisition and analysis. However, the processing stage is more complex specially when compared to LT (which is straightforward). As will be further reviewed, signal processing in PT is a fundamental stage in order to enhance image quality. Without this stage, the detection capabilities of PT is limited to near-surface defects because the thermal signals are highly contaminated by several sources of noise, such as non-uniform heating, emissivity variations and environmental reflections among others.

2.2 Application and Experimental Pulsed Thermography

2.2.1 Modes and configurations in PT

The inspection by PT can be deployed using several configurations and modes. As depicted in Figure 2.2, there are three basic configurations for heating and testing the specimen: point-, line- and surface-heating. Point testing is heating with a laser or a focused light beam. Its advantages are uniform and repeatable heating. However, this configuration needs to move the test heat to fully inspect a surface, hence slowing down the test process.

Line testing involves heating by lamps, heated wire or scanning laser. Advantages include fast testing rate (up to 1 $m^2.s^{-1}$ is reported) and good uniformity thanks to the lateral motion. A drawback is that only part of the history curve is available because of the lateral motion of the specimen and the fixed distance between thermal stimulation and temperature signal pickup. To conclude, surface inspection uses heating by lamps or flash lamps. Advantages include the complete analysis of the phenomenon because the whole temperature history is recorded. A drawback is the anisotropy of heating by lamps and flashes.

Point and line heating methods are favorable only when defect detection is limited to cases where the defect depth is known and constant: for example, in bonded assemblies where the defects are located between layers of known thickness, presumably at the bonding interface (Maldague, 2001).

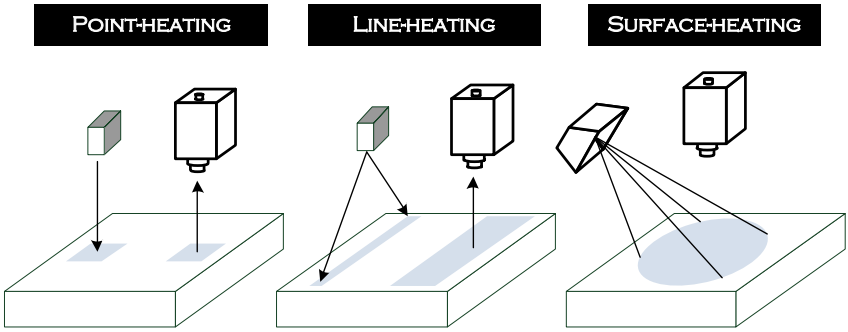

Figure 2.2: Configurations for PT inspection [Adapted from Maldague and Ibarra-Castanedo (2013, chap. 10)]

Pulsed thermography can also be deployed using two modes or observation methods: transmission and reflection mode. In the transmission mode the heat flux is applied by radiation over the surface of the material, so the infrared radiation received by the IR camera is a function of the amount of heat that is transferred by conduction from one side of the material to another. As is illustrated in Figure 2.3, the heating source and the detector (or IR camera) are located one on each side of the component to inspect.

In the reflection mode the heat front produced by the thermal stimulation propagates through the material until it reaches zones with different thermal properties (or defective zones), 'reflecting' back part of the thermal energy applied. Generally, the reflection approach is used for detection of discontinuities located close to the heated surface whereas the transmission approach allows detection of discontinuities close to the rear surface because of the spreading effect of the thermal front. Moreover if the rear surface is not accessible, the transmission approach is not possible.

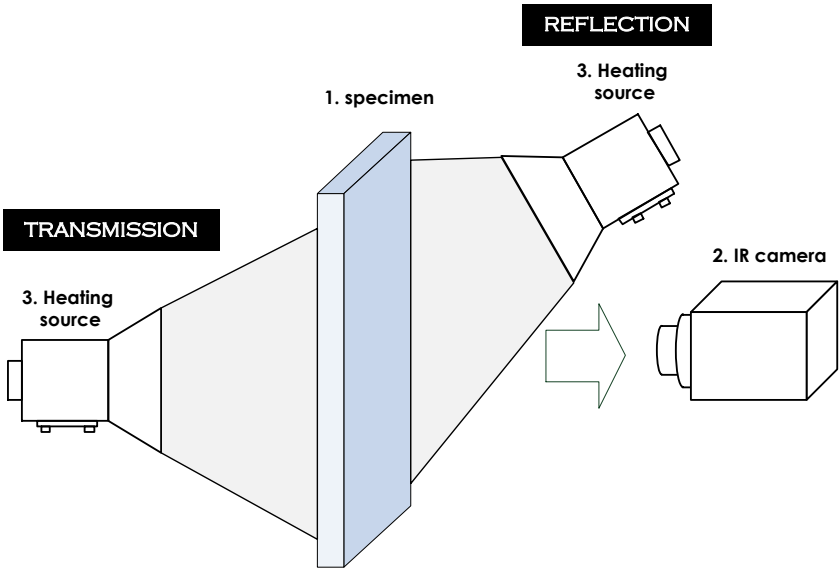

Figure 2.3: Modes or observation methods in pulsed thermography inspection.

2.2.2 Experimental Approach

In this research, the application of the pulsed thermography inspection is carried out using the surface-heating configuration and reflection mode. As depicted in Figure 2.4, the inspection system consists on the use of two photographic flash lamps (Balcar FX60, each giving 6.4 *kJ* for 15 *ms*, 2 *ms* at full width half maximum) to produce a high-power short pulse used to stimulate the specimen surface. Once the pulse is delivered to the specimen surface, the acquisition of thermal images is carried out straightaway using an FPA infrared camera (Santa Barbara FPA SBF125, 3 to 5 μm, with a 320×256 pixel array).

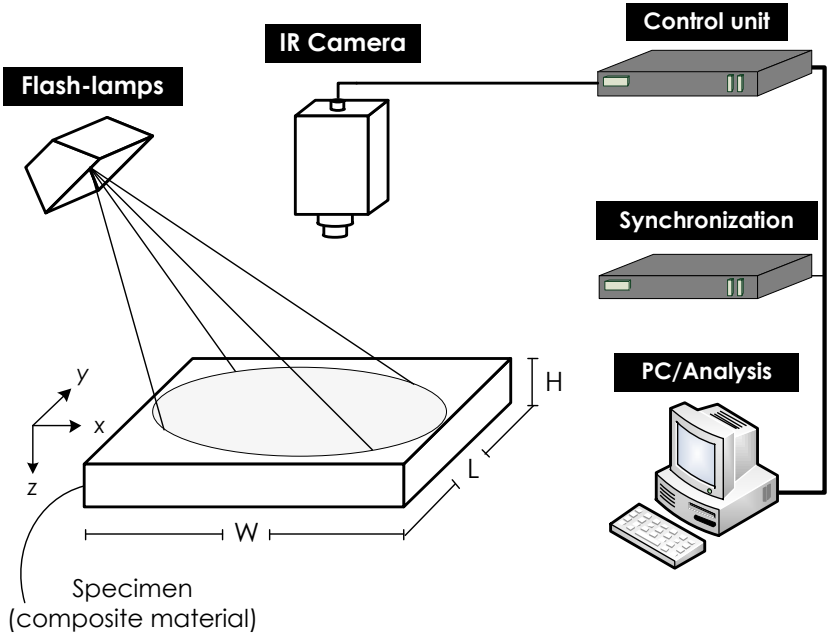

Figure 2.4: Experimental configuration of the pulsed thermography system.

As already shown in Figure 2.4, a synchronization unit is necessary in order to accurately control the time between the launching of the thermal pulse and the recording with the IR camera. Moreover, two power amplifiers (one for each flash lamp) are required to increase the power of the irradiation. The laboratorial instruments (available at the Canadian Research Chair MiViM) used for the PT inspection are illustrated in Figure 2.5.

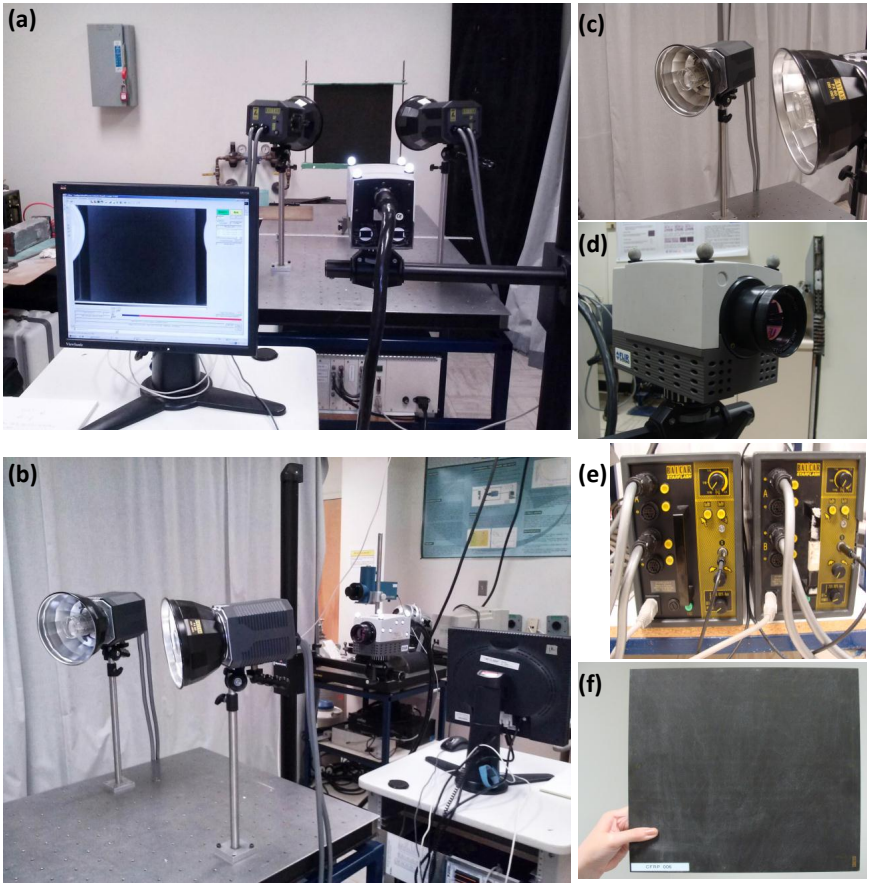

Figure 2.5: Experimental system for the PT inspection: (a) front view, (b) rear view, (c) photographic flash lamps, (d) IR camera, (e) power amplifiers, and (f) plate specimen.

In this thesis is investigated the PT inspection on two academic specimens (Carbon Fiber Reinforced Polymer CFRP006 and Glass Fiber Reinforced Polymer GFRP006). Both specimens consist of a 10-plies fiber reinforced polymer with 25 Teflon square insertions located at different depths and having different lateral sizes. The thickness of the Teflon inserts is 0.1 *mm*. The configuration of both specimens is depicted in Figure 2.6.

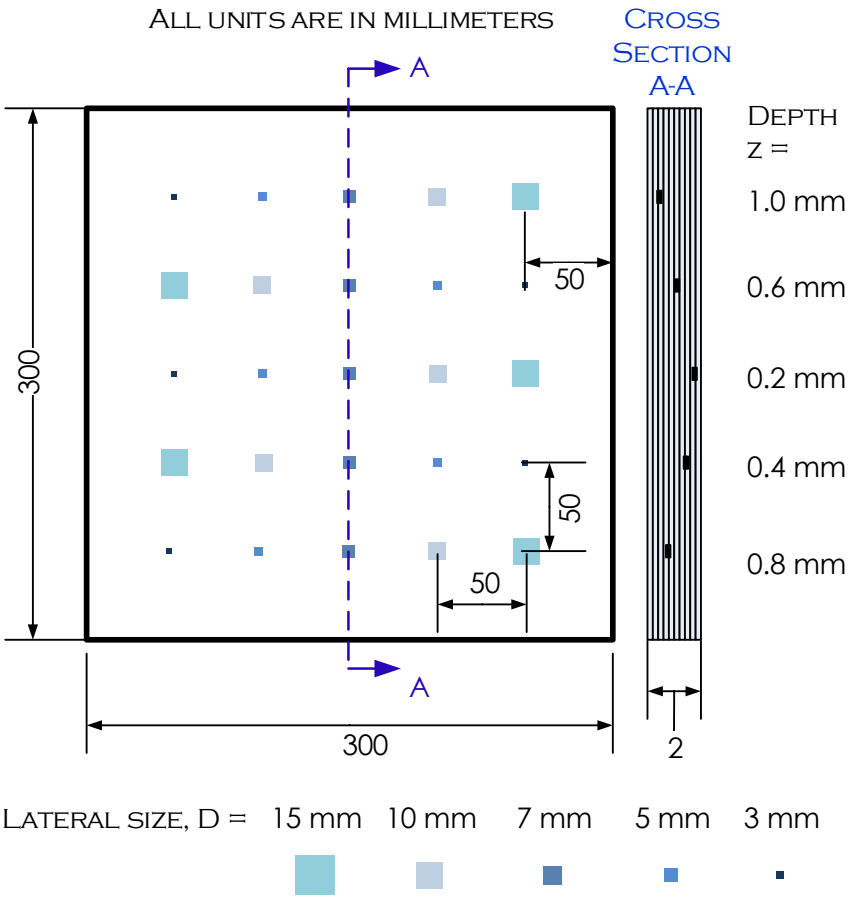

Figure 2.6: Composite plates specifications.

In order to enhance the emissivity to a values near to 1, the specimens were painted with a black paint prior to the PT inspection. This procedure also contributes to dimmish the emissivity variations on the surface and to eliminated reflections from the environment.

2.2.3 Data acquisition and analysis

As discussed earlier, the analysis of subsurface defects in PT is concerned to the imposed cooling process followed the thermal excitation. Once the material is stimulated, an IR camera records the surface temperature decay, then the thermal images acquired are stored as a 3D matrix (see Figure 2.7a). The spatial $x-$ and $y-$ coordinates correspond to the pixel numbers in the I and J directions, respectively, whilst the $z-$ coordinate represents time. In order to exploit all the resources of the IR camera (and to avoid loss of information), a fixed acquisition frequency f_s = 157 Hz ($\Delta t = 1/f_s = 0.00637$ s per image) was used, which is the maximum full-frame rate achieved for a 320×256 pixel array. Furthermore, a total of $N = 1000$ frames (maximum storage capacity of the IR camera) were collected during the cooling regime, being the acquisition window $w(t) = 6.37$ s. All the results showed in further chapters are based on these acquisition parameters.

The analysis of the PT sequence is shown in Figure 2.7b. The temperature decay curves for the defective and sound areas behave similarly at the beginning of the cooling process. Once the thermal front reaches the internal defect, the accumulation of heat produced by the defective region originates an increase in temperature over the defective area on the surface. This 'breaking point' between T_d and T_{sa} (respectively, the temperature evolution curves of defective and sound area) represents the onset time, t_{onset} (see Figure 2.7b), initiating the temporal detection window (the period during which the defect is visible). As time elapses, the visibility of the defects (C_{max}) decreases until t_{blind}, the time at which the defect vanishes from the thermal images. All of these parameters (onset time, moment of maximum thermal contrast and blind time) are dependent on the thermal properties of the material and geometry (depth and lateral sizes) of the defects.

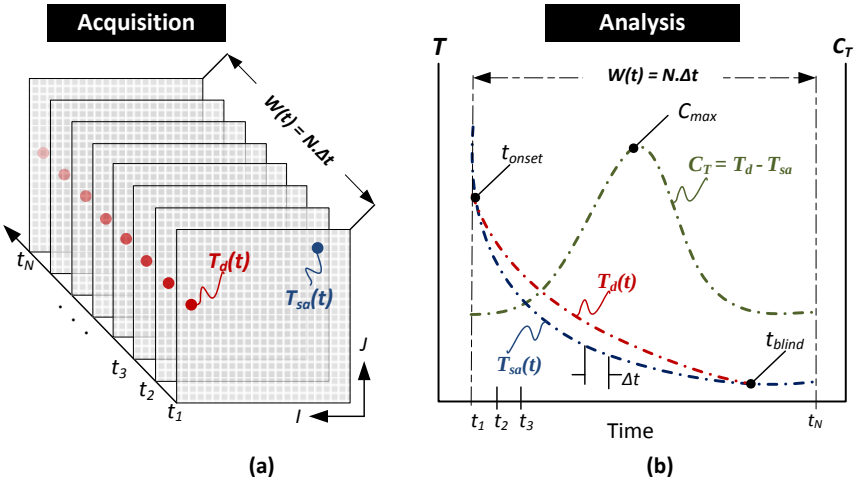

Figure 2.7: Acquisition and analysis of IR thermal images obtained during the PT inspection. (a) Acquisition of the 3D temperature matrix obtained during the PT inspection; and (b) analysis of temperature evolution curves considering $\alpha_{def} < \alpha_{sa}$, being α the thermal diffusivity.

2.2.4 Thermal contrast

Thermal contrast (C) is the variable used to characterize the level of visibility (in the thermogram) of the defects. Moreover, it is the variable traditionally used to describe defect features; in fact, most of the quantitative methods used nowadays for inversion of depth and lateral size are based on the computation of the maximum values of C (or C_{max}) (Balageas et al., 1987; Krapez et al., 1991).

The basic form of thermal contrast is the *absolute thermal contrast*, which is defined by the following expression (Maldague, 2001):

$$C_a(t) = T_d(t) - T_{sa}(t) \tag{2.1}$$

with $T_d(t)$ and $T_{sa}(t)$ defined as the temperature as function of time t for defective and non-defective regions. Eq. (2.1) is the simplest way to quantify the signal strength of the defects. There are other formulations intended to estimate the detection level of the defects while reducing the impact of optical artifacts and non-uniform heating, for instance the *run-*

ning contrast defined by the Eq. (2.2) (Grinzato et al., 1995):

$$C_r(t) = \frac{C_a(t)}{T_{sa}(t)} \tag{2.2}$$

with parameters defined as before. Eq. (2.2) considers that defective and non-defect points are located in the area with the same absorptivity-emissivity. As summarized by Maldague (2001), there are other formulations for thermal contrast (i.e. normalized contrast, running contrast); however, the application of those expressions are restricted to specific cases. All the results and discussions presented in this thesis will be based upon Equations (2.1) and (2.2).

2.3 Major Drawbacks in Pulsed Thermography

It was mentioned in previous sections some of the main limitations of pulsed thermography. Some of them are consequence of the nature of the IR measurement, while others are produced by the experimental setup and the thermal process within the specimen. In this section will be discussed the major limitations of the PT inspection.

2.3.1 Optical reflections

The IR camera converts the radiative energy received at the detectors J_{cam} into a signal proportional to the radiant energy emitted by the object under study (for instance, the specimen), which according to the Planck's Law, depends on the object temperature T_o (see Appendix A for the fundamental concepts of thermal radiation). The total radiant power incident on the detector J_{cam} can be written as a function of several sources of energy:

$$J_{cam} = \underbrace{\tau_{atm}\,\varepsilon_o\,I_o(T_o)}_{\text{specimen}} + \underbrace{\tau_{atm}\,(1-\varepsilon_o)\,I_{amb}(T_{amb})}_{\text{amb}} + \underbrace{(1-\tau_{atm})\,I_{atm}(T_{atm})}_{\text{atm}} \tag{2.3}$$

In Eq. (2.3), ε_o is the emissivity of the specimen; τ_{atm} is the spectral transmission window of the atmosphere and; T_o, T_{amb} and T_{atm} are respectively the temperatures of the specimen, ambient and atmosphere. It can be noted in Eq. 2.3 that along with the IR radiation emitted by the specimen (I_o), J_{cam} is composed by contributions from the ambient (I_{amb}) and the atmosphere (I_{atm}).

It can be deducted from Eq. (2.3) that the inspection by PT is limited to low reflectivity materials (or high absorptivity). Furthermore, ambient conditions can impose limitations when measuring at low temperatures (just below the equilibrium temperature of the specimen). The ambient term I_{amb} also considers the reflection from the surrounding; thus, any body that emits IR radiation will reflect this energy on the specimen surface, producing what is known as 'reflection artifacts'; i.e., localized hot spots in the thermal images that can leads to false-positive or misinterpretation.

2.3.2 Non-uniform heating

Non-uniform heating is one of the major - if not the most - source of uncertainty in pulsed thermography. Even when a flat surface is inspected, several factors as heating source locations (related to the IR radiation sources), equipment aging, external heating or cooling sources (both related to ambient conditions), uneven optical properties of the surface, etc., will produce irregular patterns of heating. These irregular patterns often superimpose on the contrasts produced by internal defects, consequently resulting in the reduction of spatial resolution (affecting smaller defects) and the limit of detection (affecting deeper defects). Moreover, given that defect detection principle is based on temperature differences, non-uniform heating may produce confusion, specially for defect quantification.

To illustrate the negative effects of non-uniform heating, Figures 2.8 shows two thermograms for the CFRP006 specimen at different times (0.0191 s and 0.3185 s). The thermograms correspond to the 3^{rd} and 50^{th} images of the complete thermal sequence. It can be observed the presence of a completely irregular pattern at $t = 0.0191\ s$; this image does not reveal the presence of the any internal irregularity. Additionally, the temperature disparities between different regions reach 16^oC. At $t = 0.3185\ s$ (when at least defects located at 0.8 mm should be detected) only defects located at 0.2 and 0.4 mm are visible. In spite that non-uniform heating is less significant, the image still preserves an irregular pattern of temperature especially at the edges of the specimen where the deepest defects - and the more challenging - are located.

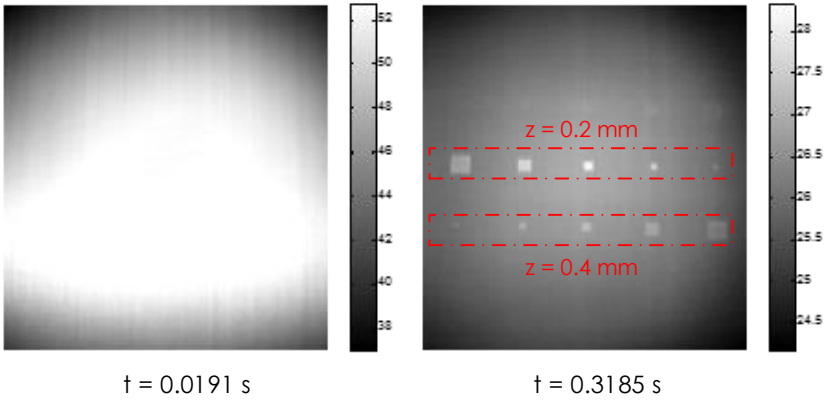

Figure 2.8: Impact of non-uniform heating. Thermograms at different times corresponding to the PT inspection on the CFRP006 specimen.

2.3.3 Lateral heat diffusion

Lateral heat diffusion is an unavoidable problem in the PT inspection. It is inherent to the heat diffusion process that takes place within the specimen and is dominated basically by the thermal properties of the material and characteristics associated to the defects (depth and lateral size). Blurring is the signal degradation and represents the major negative effect affecting mostly the deepest defects. It comes out when the heat conduction in the lateral direction becomes predominant in the diffusion process.

Considering the 3D heat diffusion problem in anisotropic media, the Fourier number for each directions (x, y and z) can be written as follows:

$$x - diffussion \rightarrow Fo_{xx} = \frac{\alpha_{xx} t}{D^2} \tag{2.4a}$$

$$y - diffussion \rightarrow Fo_{yy} = \frac{\alpha_{yy} t}{D^2} \tag{2.4b}$$

$$z - diffussion \rightarrow Fo_{zz} = \frac{\alpha_{zz} t}{z^2} \tag{2.4c}$$

In Equations (2.4), α_{xx}, α_{yy} and α_{zz} are respectively the thermal diffusivity in the $x-$, $y-$ and $z-$directions. Furthermore, D and z are the defect lateral size and depth and t is the variable time. The degradation of signal (or thermal contrast) takes place when the heat diffusion in the

$x-$ and $y-$ directions becomes predominant (Fo_{xx}, $Fo_{yy} >> Fo_{zz}$). By analysing each of the terms of Equations (2.4), it can observed that deeper defects (or those with smaller aspect ratio D/z) are more likely to suffer signal degradation. Furthermore, the thermal diffusivity plays an important role in this case, since in both specimens (CFRP006 and GFRP006) α_{yy}, $\alpha_{yy} >> \alpha_{zz}$.

The mentioned above is illustrated in Figure 2.9, where is shown two distinct regimes of heat conduction ($z_1 >> D_1$ and $z_2 << D_2$). On the bottom of Figure 2.9 is also shown an example of the level of signal degradation for defects with different aspect ratio. It can be observed that the defect with the largest aspect ratio $D/z = 15/0.2$ clearly preserves the square shape of the Teflon® delamination. In this case is predominant the conduction in the $z-$direction (at least at $t = 0.190\ s$). On the other hand, for the defect with $D/z = 7/0.6$ the heat conduction in the lateral direction produces lost of visibility because of the narrower thermal front.

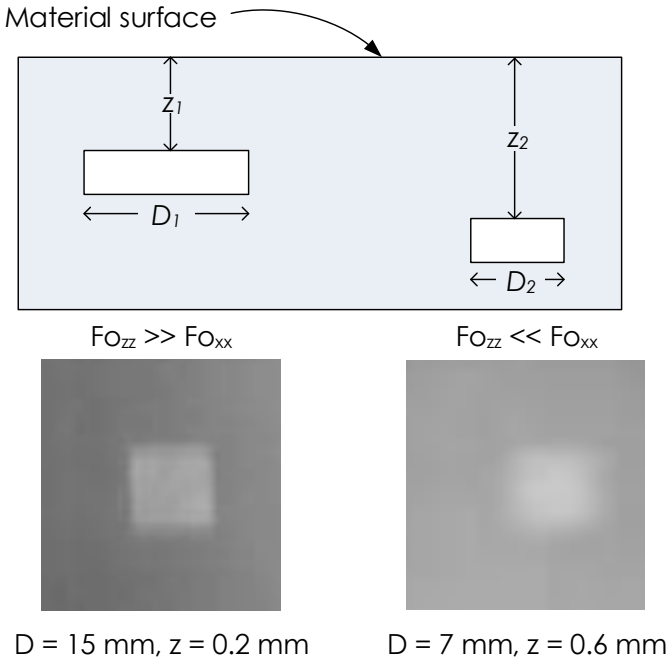

Figure 2.9: Illustration of two different regimes of heat conduction as a function of the aspect ratio of the defects, resulting in the presence of blurring.

2.4 Summary

Pulsed thermography is an attractive NDT&E technique that allows the non-contact inspection of materials. Based on the analysis of irregular thermal patterns, PT requires the application of a thermal excitation in order to provoke an internal heat flux. Due to the difference between thermophysical properties of non-defective and defective regions, variations in the internal heat flux produce irregular patterns on the surface thermal map.

PT is fast and easy to deploy. Compared to lock-in thermography - which analysis is straightforward - PT requires an additional processing stage in order to overcome the harmful effects of several sources of noises such as non-uniform heating, blurring and external reflections.

Non-uniform heating is one of the major source of uncertainty in pulsed thermography. It is an inherent problem of the configuration of the irradiation sources and it is also associated to uneven optical properties of the surface. In the other hand, lateral heat diffusion is an unavoidable problem in the PT inspection and is associated to the heat diffusion process that takes place within the specimen. Its major consequence is the blurring, which is the signal degradation that arises when the heat diffusion in the lateral direction becomes predominant in the diffusion process.

Most of the constraints present in the PT inspection can compensated thanks to the implementation of several signal processing algorithms. As will be further discussed, signal processing constitutes the core of the investigations to enhance image quality in PT.

Chapter 3

Modeling and Numerical Simulation

The objective of this Chapter is to propose and test a thermal-numerical model and to develop a methodology for the simulation of a pulsed thermography inspection on carbon laminated composites. Through the numerical approach proposed in this Chapter, it is investigated the physics of the heat transfer process that take place during the pulsed thermography inspection. Furthermore, it is analyzed the response of the surface thermal pattern due to the presence of internal discontinuities in order to conclude in terms of physically-based parameters, the efficiency and applicability of the pulsed thermography inspection technique. The analysis of the results is focused on parameters commonly used to describe the thermal behaviour of defective zones, such as the thermal contrast and onset time.

3.1 Motivations

The use of numerical techniques for the solution of complex problems in engineering and physics is nowadays a reality thanks to the dramatic advance of computers with high speed and large storage capacity. As a function of this evolution which increases exponentially, a new approach − along with new professionals − to study complex problems has emerged as a prediction method: the computational simulation.

Nowadays numerical simulation plays an important role in the analysis of TNDTs techniques as a mean to understand the involved phenomenology and to study the applicability of a given TNDT method in cases where the experimental approach is almost impossible to perform. In this regards, the effort directed toward investigations on the computational simulation of pulsed thermography inspection has increased in

recent years [Susa et al. (2007) provides a brief summary of various simplifications of the method to describe the heat transfer phenomenon during inspection by PT], encouraged mainly by the widening of the application sphere of PT to include more complex and challenging situations . This has allowed the application of PT in situations in which, until recently, inspection was not possible.

Most of the models available in the literature for the simulation of TNDT problems are based on simplified equations obtained from the solution of the 1D heat conduction equation, considering that the thermal pulse has the same temporal shape as the Dirac delta function (Almond and Patel, 1996; Lau et al., 1991). Although most of the works use this formulation to describe the thermal behaviour of the material in PT inspection, those simplified models only apply when the heat conduction regime is 1D, which in general terms is only valid for small temporal windows and shallower defects. In the other hand, the extension to 2D models has been also investigated, as reported by Krapez et al. (1991) and Vavilov et al. (1993). Both works used the 2D heat conduction equation in cylindrical coordinates to model the PT inspection problem, allowing thus to perform a more detailed analysis which included the geometry of the defects. The use of computational softwares, such as Comsol, ThermoCal-3D and ThermoHeat-3D Pro, has also been investigated as a reliable tool for the study of complex TNDT situations, including 3D problems and the inspection of 30 types of anisotropic materials [see for instance, Avdelidis and Almond (2004); Weiser et al. (2010) and Vavilov (2012)].

In spite of the advance in the simulation of TNDT problems, yet there are several pending variables (e.g., non-uniform heating, irradiation power, location and geometry of the defects) that have not been studied in details and that might affect the thermal response of the material during the PT inspection. Furthermore, given that most inversion methods of subsurface defects are based on thermal parameters (such as thermal contrast and onset time), the precision of the quantitative analysis may also be affected. For these reasons, it has been included in this research a thermal-numerical approach in order to carry out an in-depth analysis of the thermal response of the material when varying several parameters associated to both, the defects and the thermal excitation. This analysis will allow to obtain more detailed information concerning to the dependence of the maximum thermal contrast, its time of occurrence and onset time of defects, as function of the intensity and surface irradiation function, and; thickness, depth and lateral size of the defects.

3.2 Thermal Modeling

Figure 3.1 shows the description of the inspection by pulsed thermography and the physical domain under study. The specimen under investigation (with geometry W x L x H) is a composite material possessing internal delamination defects. Each defect is located at different depths and has different lateral sizes (for complete details of the specimen, see Appendix 4.1). At the beginning of the PT inspection ($t = t_o$), the specimen is in thermal equilibrium with the environment; at time $t = t_1$ an external stimulation is applied to the surface, causing the propagation of a thermal front through the material by diffusion. The resulting thermal response of the specimen to this stimulation is monitored via infrared thermal emission.

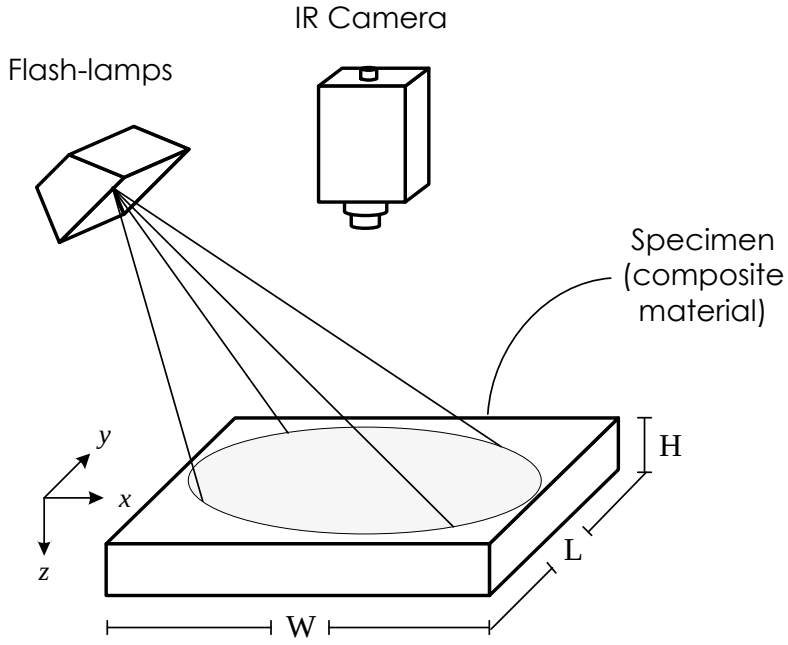

Figure 3.1: Proposed thermal model for the PT inspection and physical domain under study.

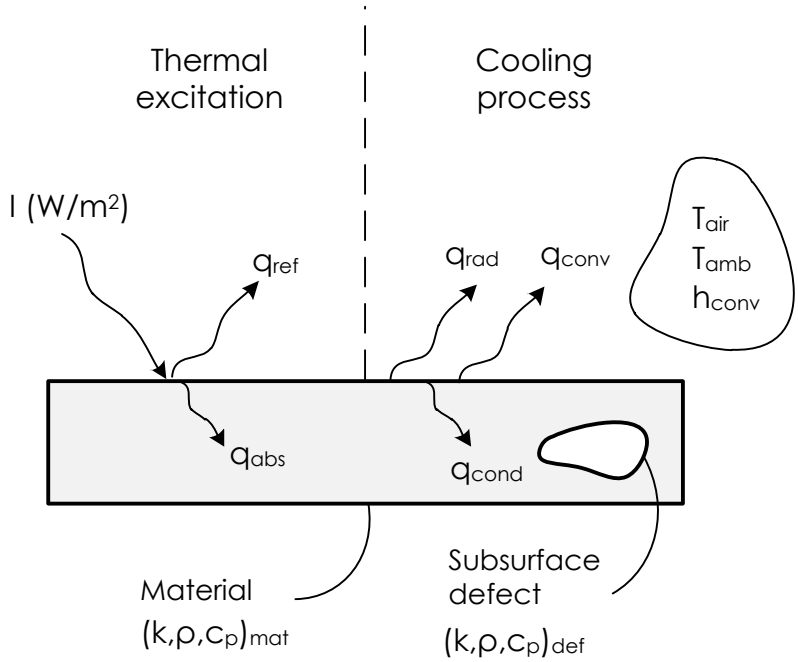

Figure 3.2: Cross-section view of the specimen with the heat flow paths participating during the PT inspection.

The participating heat fluxes considered in the thermal model are depicted in Figure 3.2. The external excitation is applied by radiation heat transfer. Part of the incident energy is absorbed and the rest is reflected by the material surface. Due to the sudden increase in temperature caused by the thermal excitation, a thermal front is created and this propagates through the rest of the material by heat conduction. Heat transfer by convection and radiation also take places between the material surfaces and the environment. Internal discontinuities are resistive defects: regions of the material with different thermal properties which affect the heat flux rate.

In order to derive a mathematical model to describe the physical process of the PT inspection, the following simplifying assumptions are considered:

1. The inspection is carried out in transient regime;

2. The heat transfer within the material occurs in 3D with Cartesian coordinates;
3. The applied heat flux (thermal pulse) is unidirectional in the z-direction;
4. The material is opaque;
5. The penetration of radiation within the material is neglected;
6. No chemical reaction occurs as a consequence of the heat irradiation;
7. The thermophysical properties of the medium remain constant during the inspection and are independent of temperature;
8. The composite is macroscopically homogenous;
9. The fibers are homogeneously distributed within the matrix;
10. The thermal resistance between the fiber and matrix phases is negligible;
11. The fibers and matrix are homogeneous and isotropic; and
12. The fibers are equal and uniform in shape and size.

Based on assumptions 1 to 7, the governing equation that describes the heat transfer in an anisotropic media is:

$$(\rho c_p)_{eff}\frac{\partial T}{\partial t} = \frac{\partial}{\partial x}\left(k_{xx}\frac{\partial T}{\partial x}\right)+\frac{\partial}{\partial y}\left(k_{yy}\frac{\partial T}{\partial y}\right)+\frac{\partial}{\partial z}\left(k_{zz}\frac{\partial T}{\partial z}\right) \tag{3.1}$$

The initial condition is given by:

$$T(x,y,z,t_o) = T_{amb} \tag{3.2}$$

Boundary conditions, including heat transfer by radiation and convection between all the specimen surfaces and the environment, are defined by the following expression:

$$n\cdot(k\nabla T) = h_{conv}(T_{amb}-T)+\sigma\varepsilon(T_{amb}^4-T^4) \tag{3.3}$$

In Equations (3.1) to (3.3), ρ and c_p are, respectively, the effective density and specific heat of the medium; T represents the temperature of

the material along coordinates x, y and z; and T_{amb} is the ambient temperature considering that the air and the external environment are at the same temperature. The surface emissivity is represented by ε and σ is the Stefan-Boltzmann constant. The convection heat transfer is given by h_{conv} and t represents the variable time. In addition, k_{xx}, k_{yy} and k_{zz} are the thermal conductivities for the x, y and z coordinates, respectively.

The methodology adopted in this research to calculate the thermophysical properties in Eq. (3.1) is discussed in the next section.

3.2.1 Thermal properties for heterogeneous media

One of the most important concerns when modeling heat transfer in composite materials is finding an appropriate formulation to determine the thermophysical properties of the medium. When sufficient information related to the material is available, it is possible to develop a strategy and obtain a mathematical formulation to describe the thermal properties.

As depicted in Figure 3.3, the composite material under study consists of a 10-ply panel of carbon fiber-reinforced polymer laminates, with 0.2 *mm* thickness each. Each ply is modeled as a porous material, the matrix being represented by epoxy-resin and the pores by the fibers (see top of Figure 3.3).

Taking into consideration assumptions 8 to 12, for a two-component system and based on the rule-of-mixtures the effective heat capacity of the composite medium can be estimated from the weighted average of the specific properties of each phase based on the volume fractions:

$$(\rho c_p)_{eff} = \phi_f(\rho c_p)_f + (1-\phi_f)(\rho c_p)_m \tag{3.4}$$

In Eq. (3.4), ϕ_f denotes the volume fraction of the fiber and is given by:

$$\phi_f = \frac{V_f}{V_T} = \frac{V_f}{V_f + V_m} \tag{3.5}$$

The subscripts in Equations (3.4) and (3.5) denote, respectively, the fiber and epoxy-resin. As in the case of the heat capacity, a common approach to determining the thermal conductivity of a heterogeneous material consists of combining structural models using empirical weighting (Pan and Hocheng, 1996). The basic model for thermal conductivity is the series-parallel model, which calculates the effective thermal conductivity

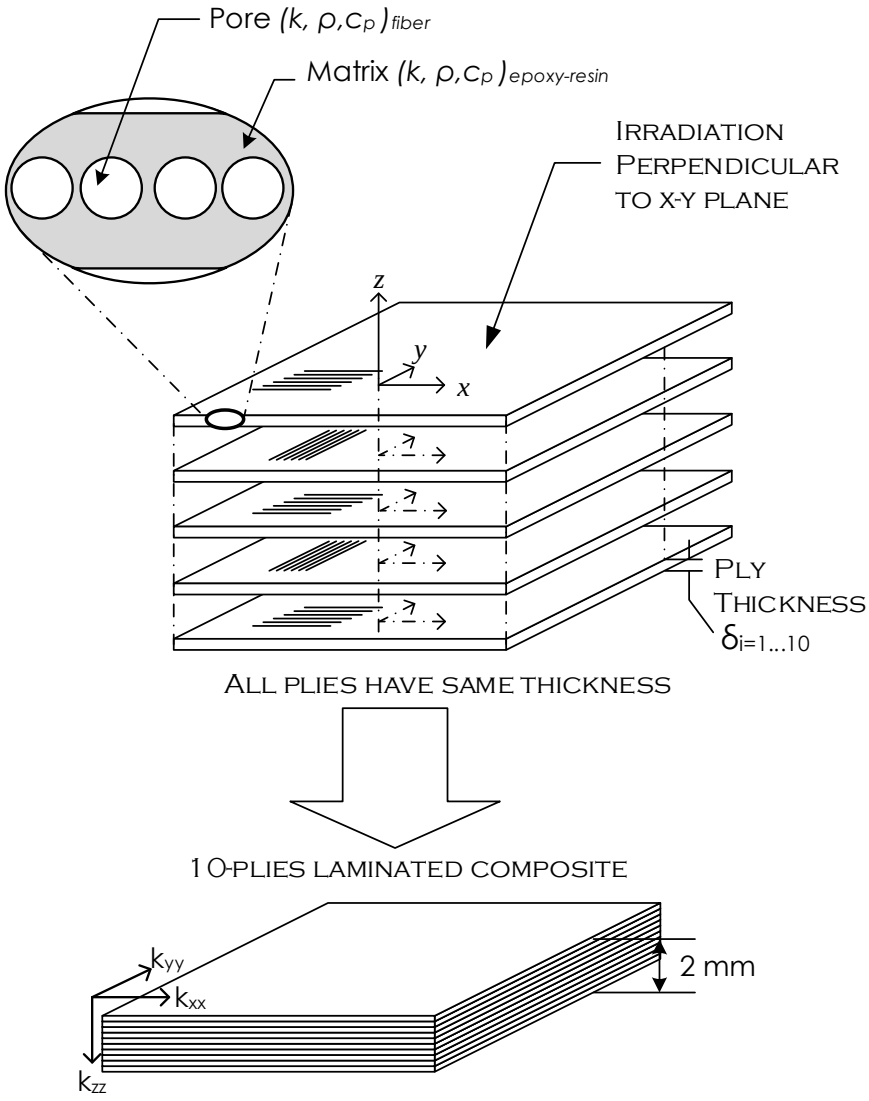

Figure 3.3: Schematic representation of the composite medium and its constituent.

based on the volume fraction and thermal conductivity of each component. This model is valid only when both quantities are precisely known and conduction is the only mechanism of heat transfer (Wang et al., 2006).

In the series-parallel model the fiber and matrix are modeled as thermal resistors, or a mixture of series and parallel structures whose values are inversely proportional to the thermal conductivity. The expressions for the equivalent thermal conductivity in the longitudinal and transverse direction to the $x-y$ plane are:

$$k_{\parallel} = k_f \phi_f + k_m(1-\phi_f) \tag{3.6a}$$

$$k_{\perp} = \frac{k_f k_m}{k_m \phi_f + (1-\phi_f) k_f} \tag{3.6b}$$

In Equations (3.5) and (3.6), k_f and k_m represent the thermal conductivities of the fiber and matrix, respectively. In this research, a more detailed model for the longitudinal thermal conductivity is proposed and tested; this model is a modified equation that takes into consideration the geometrical disposition of the fiber and matrix. For circular filaments, the Behrens-theoretical model for transverse thermal conductivity is given by:

$$k_{\perp} = k_m \left[\frac{k_f(1+\phi_f) + k_m(1-\phi_f)}{k_f(1-\phi_f) + k_m(1+\phi_f)} \right] \tag{3.7}$$

Once the parallel and transversal thermal conductivities ($k_{\parallel}$ and $k_{\perp}$) have been obtained, the global conductivities of each ply (k_x, k_y and k_z) are straightforwardly calculated through the following expressions:

$$k_{xx} = (k_{\parallel} \cos\theta) + (k_{\perp} \sin\theta) \quad [in-plane] \tag{3.8a}$$

$$k_{yy} = (k_{\parallel} \sin\theta) + (k_{\perp} \cos\theta) \quad [in-plane] \tag{3.8b}$$

$$k_{zz} = k_{\perp} \quad [out-of-plane] \tag{3.8c}$$

where θ is the fiber orientation angle with respect to the global $x-axis$. So far, the discussion has been focused exclusively on the determination of the global thermal conductivities of a single laminated composite. Since in this case the configuration of the panels under study is comprised of more than one ply (see Figure 3.3), the global thermal conductivities of the specimen can be obtained using, once again, an electrical analogy.

Considering that the applied heat flux (thermal excitation) is perpendicular to the $x-y$ plane, it is possible to model the plies as thermal resistances which are in series and parallel to the heat flow direction. The resulting global conductivity components are expressed as:

$$k_{xx} = \frac{\sum_{i=1}^{N} (k_{xx}\delta)_i}{\sum_{i=1}^{N} \delta_i} \quad [in-plane] \tag{3.9a}$$

$$k_{yy} = \frac{\sum_{i=1}^{N} (k_{yy}\delta)_i}{\sum_{i=1}^{N} \delta_i} \quad [in-plane] \tag{3.9b}$$

$$k_{zz} = \frac{\sum_{i=1}^{N} \delta_i}{\sum_{i=1}^{N} \left(\frac{\delta_i}{k_{zz}}\right)_i} \quad [out-of-plane] \tag{3.9c}$$

Equations (3.9) represents the global thermal conductivities that are used to obtain the solution of the conduction heat equation for anisotropic materials. In Equations (3.9), δ and N represent the thickness of each ply and the total number of single laminates comprising the composite structure. Furthermore, the summations appearing in these equations are carried out using the thermal conductivity for a single-laminated composite [Equations (3.8)].

3.2.2 Irradiation power density function

Several authors have concluded that one of the most undesirable factors affecting the detection of defects in pulsed thermography is non-uniform heating (Ibarra-Castanedo and Maldague, 2004; Ibarra-Castanedo et al., 2009). For this reason, in order to perform a detailed study on the impact of non-uniform heating on the detection of defects through computational simulation, in this research the spatial distribution of the irradiation on the surface was modeled using a Gaussian distribution function.

Since it was considered that the specimen is opaque and there is no penetration of radiation into the material (see assumptions 4 and 5), and considering a Gaussian power density distribution function, the portion of the energy absorbed when a thermal pulse is applied over the material surface is given by the following expression:

$$q(x,y) = \frac{I_{rad}}{\delta(t)} \cdot (1-\rho) \cdot \frac{8}{\pi d^2} exp\left[-\left(\frac{2\sqrt{2}}{d} \right)^2 \cdot (x^2+y^2) \right] \tag{3.10}$$

where I_{rad} is the radiant heat, ρ the surface reflectivity, $\delta(t)$ the duration of the thermal pulse and d the diameter of the power density distribution. Figure 3.4 shows the power density function obtained using Eq. (3.10), observing that most of the applied energy is concentrated in the middle of the test sample.

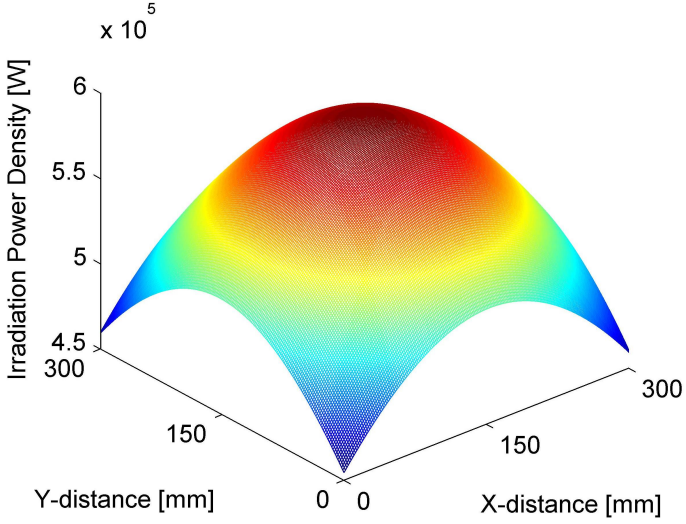

Figure 3.4: Irradiation power distribution function

3.2.3 Natural convection heat transfer coefficients

The last term to be derived is the natural convection heat transfer coefficient that appears in Eq. (3.3) which needs to be computed in order to account for the amount of thermal energy transferred to the external environment by the sample surfaces. The approach that will be used in this study considers an independent convection coefficient as a function of the position of each surface, as proposed Rodriguez and Nicolau (2012). Thus, for the lateral surfaces of the sample (four surfaces in the vertical position), the convection coefficient $\overline{h}_{lat}$ is given by Eq. (3.11):

$$\overline{h}_{lat} = \frac{k}{H}\overline{Nu}_H \tag{3.11}$$

being $\overline{Nu}_H$ the *Nusselt number* based on H, which is computed via the following expression (Bergman et al., 2011):

$$\overline{Nu}_H = 0{,}68 + \frac{Ra_H^{1/4}}{[1+(0{,}492/Pr)^{9/16}]^{4/9}} \tag{3.12}$$

In Eq. (3.12), Ra_H is the *Rayleigh number* based on H, defined by:

$$Ra_H = \frac{g\beta(T_s - T_{ar})H^3}{\alpha\nu}, \tag{3.13}$$

where T_s and T_{ar} represent the temperature of the sample surface and the air, respectively. In this model, the air and the ambient are considered to be at the same temperature. The *Prandtl number* is given by the Eq. (3.14).

$$Pr = \frac{\nu}{\alpha} \tag{3.14}$$

In Eqs. (3.11) - (3.14), k represents the thermal conductivity of the air; α and ν are, respectively, the thermal and momentum diffusivities; β is the thermal expansion coefficient. The convection coefficient for the upper surface of the sample is defined by (Bergman et al., 2011):

$$\overline{h}_{upp} = 0{,}15\frac{k}{A_s/P}\overline{Ra}_L^{1/3} \tag{3.15}$$

Finally, the convection coefficient for the lower surface is calculated by the following expression (Bergman et al., 2011):

$$\overline{h}_{low} = 0{,}27\frac{k}{A_s/P}\overline{Ra}_L^{1/4} \tag{3.16}$$

In Eqs. (3.15) - (3.16), A_s/P is the characteristic length defined as the relation between the area and the perimeter of the surface under consideration. Once all the variables present in the governing equations have been defined, the next step is the solution of the heat conduction equation [Eq. (3.1)], using the initial and boundary conditions [Equations (3.2) and (3.3)] over the domain represented by H x L x W. In this regard, the solution approach used is described in the next section.

3.3 Numerical Formulation

The solution of the governing equations was carried out employing the Finite Volume Method (FVM), which was successfully used to investigate different parameters during a thermal non-destructive test carried out by infrared thermography [see, for instance, Rodriguez and Nicolau (2012) and Lopez et al. (2012)]. This method consists of the integration of space and time, over an elemental volume, the energy equation in the conservative form, which is equivalent to performing energy balances over all the elemental volumes (Maliska, 2004). Thus, the conservation of energy is guaranteed on each elemental volume, this being one of the most notable advantages of the FVM.

Figure 3.5 shows an energy balance over a generic elemental volume with dimensions dx x dy x dz, which was the methodology used to obtain all of the local equations of temperature. The quantities q_x, q_y, and q_z represent the incoming and outgoing heat fluxes to the control volume, considering any of the three heat transfer process: conduction, convection and radiation.

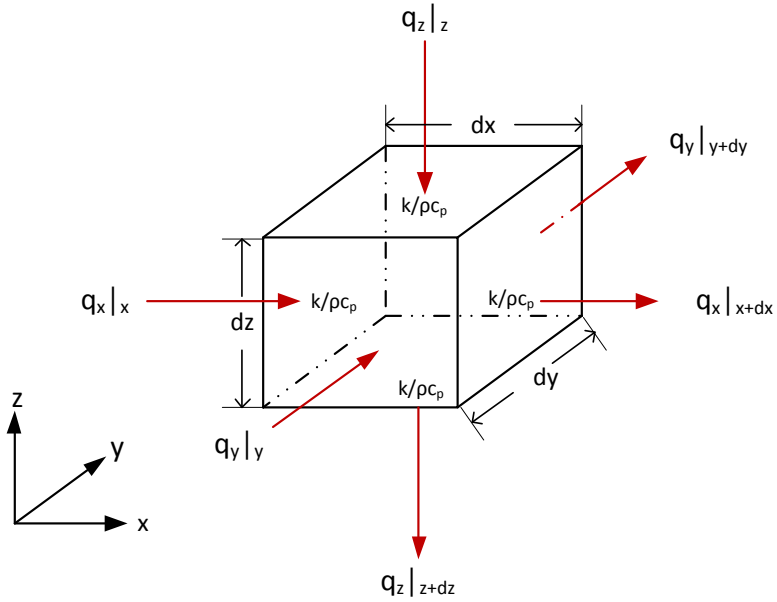

Figure 3.5: Energy balance for an elemental volume for a cell-center mesh.

As depicted in Figure 3.6, the domain under study was divided into twenty-seven (27) types of elemental volumes, according to the position and the heat transferred to the external environment and its neighborhoods. The energy balances provide the local temperature equation at the center of the volume (cell-center mesh), while the material thermal properties (thermal conductivity and specific heat) remain stored at the interface of the control volume.

Integrating Eq. (3.1) in space and time over the control volume shown in Figure 3.5:

$$\int_t^{t+\Delta t} \int_\Omega \rho c_p \frac{\partial T}{\partial t} = \int_t^{t+\Delta t} \int_\Omega \nabla.(k \nabla T) \tag{3.17}$$

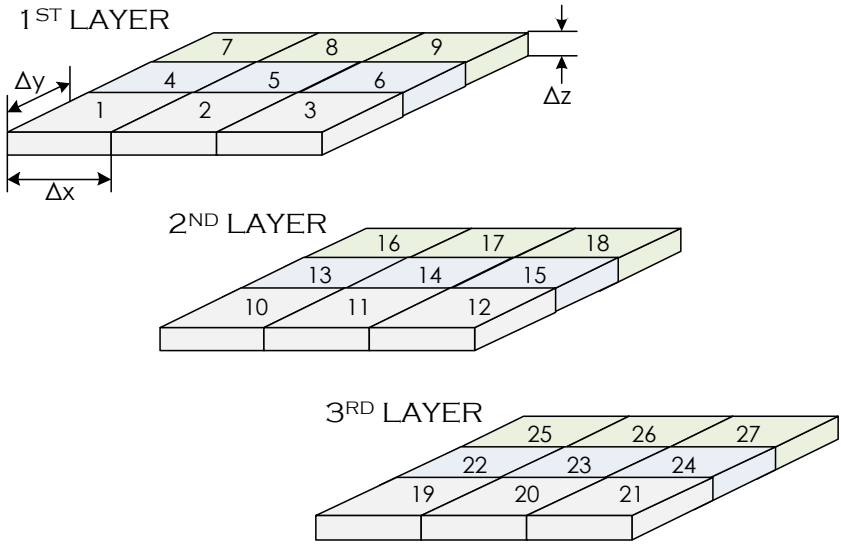

Figure 3.6: Discretization of the domain into twenty-seven (27) types of volumes, according to the position and the heat transferred to external environment and their neighborhoods.

the discrete energy balance for the internal volumes is obtained,

$$\begin{aligned}
\frac{\rho c_p \Delta x \Delta y \Delta z}{\Delta t}\left(T_P^{t+1} - T_P^t\right) &= \frac{k}{\Delta x}\left(T_W^t - T_P^t\right)\Delta y \Delta z \\
&+ \frac{k}{\Delta x}\left(T_P^t - T_E^t\right)\Delta y \Delta z \\
&+ \frac{k}{\Delta y}\left(T_N^t - T_P^t\right)\Delta x \Delta z \\
&+ \frac{k}{\Delta y}\left(T_P^t - T_{S)}^t\right)\Delta x \Delta z \\
&+ \frac{k}{\Delta z}\left(T_B^t - T_P^t\right)\Delta x \Delta y \\
&+ \frac{k}{\Delta z}\left(T_P^t - T_F^t\right)\Delta x \Delta y
\end{aligned} \tag{3.18}$$

The first term in Eq. (3.18) corresponds to the transient (or thermal inertia) term, followed by the incoming and outgoing conduction heat fluxes in each of the spatial coordinates. Due to the diffusive nature of the internal heat conduction process within the sample test, the derivatives present in the energy equation were approximated using the central difference scheme. It should also be noted that the implicit formulation is used as the temporal interpolation function. Thus, the convergence of the iterative process will not suffer the consequences of limitations in the time step Δt.

Similarly, integrating Eq. (3.3) over space and time,

$$\begin{aligned}\int_t^{t+\Delta t}\int_\Omega n.(k\nabla T) &= \int_t^{t+\Delta t}\int_\Omega h_{conv}(T_{amb}-T)+ \\ &\int_t^{t+\Delta t}\int_\Omega \sigma\varepsilon(T_{amb}^4-T^4)\end{aligned} \tag{3.19}$$

gives the discrete energy balance for the external surfaces of the sample, which is obtained as follows:

$$\begin{aligned}\frac{k}{\Delta x/2}(T_W-T_P)\Delta x\Delta z &= h_{conv}(T_{amb}-T_P)\Delta x\Delta z+ \\ &\varepsilon\sigma\left(T_{amb}^4-T_P^4\right)\Delta x\Delta z\end{aligned} \tag{3.20}$$

It is important to mention that the numerical formulation used in this work uses entire volumes at the boundaries of the domain, thereby eliminating difficulties in the application of the boundary conditions, such as non-uniformities of the volumes (which in the case of three-dimensional problems results in greater difficulties in the computational structure) and the increment of the linear system when using fictitious volumes.

The last step in the numerical approach is the treatment of the resistive defects, since the thermal conductivities present in the Equations (3.18) and (3.20) only refer to the case when their values remain constant over the whole domain. This issue is discussed in the next section.

3.3.1 Model for internal defects: the interface conductivity

It was mentioned during the description of the formulation of the thermal model that internal defects are regions or discontinuities with different thermal properties in relation to their surroundings. Since in Eq. (3.1), k_{xx}, k_{yy} and k_{zz} do not take into consideration the variation of the thermal conductivity in the x-, y- and z-directions respectively, an appropriate prescription is necessary for evaluating the thermal conductivity at the interface of the elemental volume.

Considering the grid represented in Figure 3.7, Patankar (1980) proposed the following expression for calculating the value for the thermal conductivity at the e (east) interface:

$$k_e = \frac{2k_P k_E}{k_P + k_E} \tag{3.21}$$

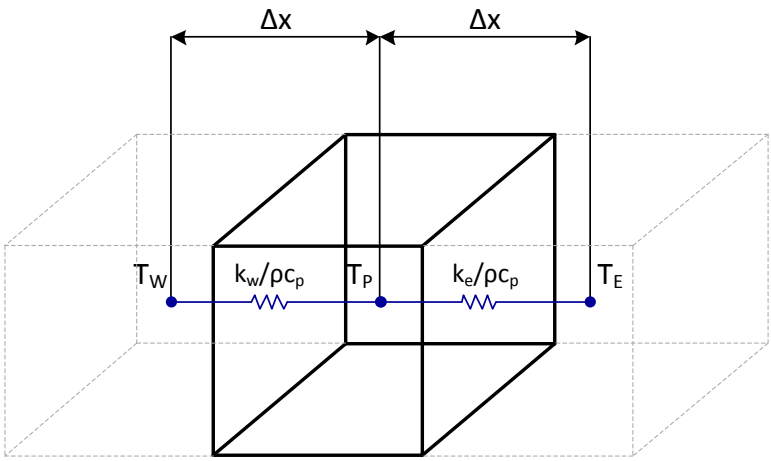

Figure 3.7: Representative model for resistive defects, as proposed by Patankar (1980).

The approximation given by Eq. (3.21) can be easily obtained for the rest of the interfaces (w, n, s, b, and f) using the thermal resistance method and this is of particular interest since, as in the FVM, it evaluates the thermal conductivity at the interface of the elemental volume.

3.3.2 Solution and convergence

In order to calculate the temperature field within the bulk of the material and at its surface, it is necessary to solve the set of energy balance equations developed in the last section. Because of the implicit formulation used as a temporal interpolation function, this set of discrete equations was solved using the Gauss-Seidel iterative method. This iterative method requires successive iterations within the same time level, until a convergence criteria is reached. In this study the following criterion was adopted:

$$RMSE(T_{sim}) \sim \sigma(T_{exp}) \tag{3.22}$$

As in Eq. (3.22), the iterative process is stopped when the root mean square error of the surface mean temperature $RMSE(T_{sim})$ is of the same order as the standard deviation of the experiment $\sigma(T_{exp})$. Both quantities are respectively computed using the following expressions:

$$RMSE(T_{sim}) = \sqrt{\frac{\sum_{i=1}^{n}(T_{sim,i} - T_{sim,i-1})^2}{n}} \tag{3.23}$$

and,

$$\sigma(T_{exp}) = \sqrt{\frac{\sum_{i=1}^{N}(T_{exp,i} - \bar{T}_{exp})^2}{N-1}} \tag{3.24}$$

In Equations (3.23) and (3.24), n and N are, respectively, the total number of iterations and experimental measurements. Figure 3.8 shows the evolution of the *RMSE* as a function of the number of iterations. The number of iterations required to satisfy Eq. (3.22) was twelve. On the other hand, Figure 3.9 shows the evolution of the surface mean temperature over time considering different numbers of iterations (1, 5 and 12), showing an unrealistic solution with higher-order oscillations when the solution is carried out with only one iteration.

A computational program called *PulsedThermography*® was developed to compute and analyze the thermal response of the material when an optical/thermal excitation is applied to the sample surface. The program was developed using the MatLab® platform (MathWorks, 2010)

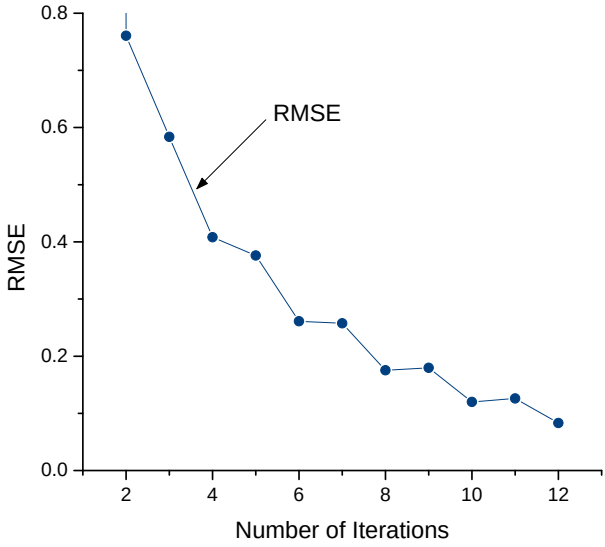

Figure 3.8: Root mean square errors as function of Gauss-Seidel iteration numbers.

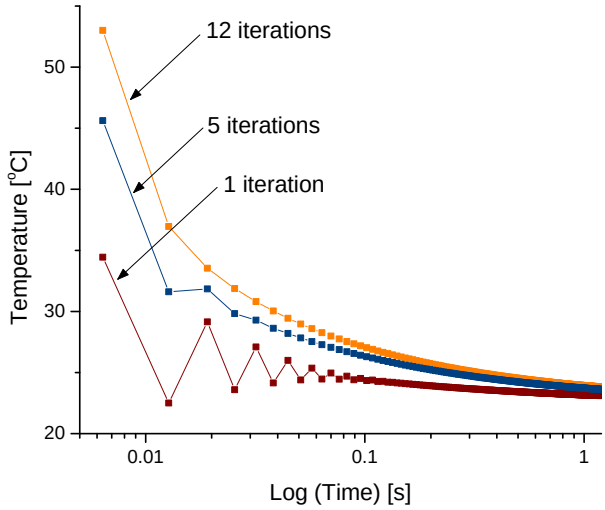

Figure 3.9: Surface mean temperature evolution curves for different Gauss-Seidel iterations numbers.

and it provides the temperature field over time and the thermal map of the surface of the material, in a similar way as in a real NDT carried out by infrared thermography. In this way, several parameters can be studied, including the characteristics related to the thermal excitation (intensity and non-uniform heating) and internal defects. The simulation parameters and thermophysical properties of the inspected material are presented in Table 3.1. All the numerical results reported below were obtained using the same mesh and time step, assuring the consistency of the results.

3.4 Experimental Validation

Although information on a physical process is often obtained through actual measurements, theoretical calculation is considered a reliable prediction method and a means to obtain valuable information in a straightforward, fast and low-cost way. However, since theoretical prediction is carried out using a mathematical model rather than a physical model (Patankar, 1980), an experimental validation has been included in order to validate the mathematical model and the hypothesis upon which the governing equations are based.

The experimental validation was performed using qualitative and quantitative approaches. The qualitative verification consisted of carrying out a pulsed thermography inspection of the carbon fiber-reinforced polymer specimen (described in Appendix 4.1) and comparing the temperature decay curves of different defective zones with that obtained through numerical simulation. A total of five experiments were carried out in order to calculate the standard deviation for the measurements. Details concerning to the experimental approach are found in Section 2.2.3.

The thermal decay curves for the defective and non-defective regions, obtained either by numerical simulation or experimental tests, were computed using the following expressions:

$$T_d(t) = \sum_{i=1}^{nx} \sum_{j=1}^{ny} \frac{T(i,j)_d}{nx \cdot ny} \tag{3.25a}$$

$$T_{sa}(t) = \sum_{i=1}^{nx} \sum_{j=1}^{ny} \frac{T(i,j)_{sa}}{nx \cdot ny} \tag{3.25b}$$

Table 3.1: Simulation parameters and thermophysical properties used in the numerical simulation.

Symbol	Simulation Parameter	Value
$nx \times ny \times nz$	number of elements	$202 \times 202 \times 42$
$dx \times dy \times dz$	dimension of volumes	$1.5 \times 1.5 \times 5E^{-2}$
Δt	time sept	$6.37E^{-3}\ s$
T_o	initial temperature	$22.5\ ^oC$
T_{amb}	ambient temperature	$22.5\ ^oC$
T_{air}	air temperature	$22.5\ ^oC$
$H \times L \times W$	sample dimension	$300\ mm \times 300\ mm \times 2\ mm$
δ	ply thickness	$0.2\ mm$
δt	pulse duration	$15E^{-3}\ s$
I_{rad}	radiant heat	$12.8\ J$, $25.6\ J$
h_{lat}	convection heat transfer coefficient (lateral)	$30\ W/(m^2 \cdot \mathrm{K})$
h_{upp}	convection heat transfer coefficient (upper)	$5\ W/(m^2 \cdot \mathrm{K})$
h_{lower}	convection heat transfer coefficient (lower)	$5\ W/(m^2 \cdot \mathrm{K})$

Symbol	Thermophysical Properties	Value
ϕ_f	volume fraction	0.69
ρ_f	density (fiber)	$1790\ kg/m^3$
cp_f	specific heat (fiber)	$710\ J/(kg.\mathrm{K})$
k_f	thermal conductivity (fiber)	$50\ W/(m.\mathrm{K})$
ρ_m	density (matrix)	$1265\ kg/m^3$
cp_m	specific heat (matrix)	1716
k_m	thermal conductivity (matrix)	$0.232\ kg/m^3$
ρ_t	density (Teflon)	$2200\ kg/m^3$
cp_t	specific heat (Teflon)	$1050\ J/(kg.\mathrm{K})$
k_t	thermal conductivity (Teflon)	$0.25\ kg/m^3$
ε	emissivity	0.97
ρ	reflectivity	0.02

In Equations (3.25), T_d and T_{sa} correspond to the temperature signals of the defective and non-defective regions. T_d is computed as the mean value over the entire defective region. Similarly, T_{sa} is computed as the mean value within the surroundings of the defective area. The area over which T_{sa} is calculated is twice the lateral size of the defective region. Further discussions and analysis are based upon Equations (3.25). Figure 3.10 shows a comparison between the theoretical and experimental decay curves (which refer to the cooling process resulting from the applied thermal stimulation) for defects with different aspect ratios, D/z.

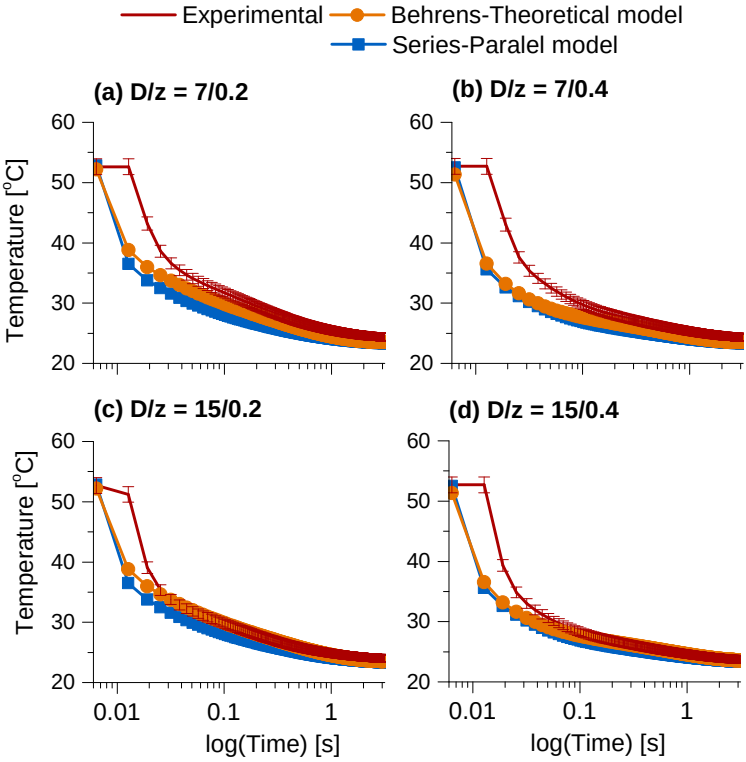

Figure 3.10: Comparison between experimental and simulated thermal decays of defective areas were obtained using the Transversal and Behrens-Theoretical models for thermal conductivity. Results correspond to defects with aspect ratio $D/z = 7/0.2$, $7/0.4$, $15/0.2$ and $15/0.4$.

Theoretical curves were obtained using the models for transversal thermal conductivities described in Section 3.2.1: the series-parallel and the Behrens-theoretical models. Sub-plots in logarithm scale have been include in order to observe the beginning of the cooling process in greater detail.

As depicted in Figure 3.10, both numerical solutions − obtained using the series−parallel and the Behrens−theoretical models for transversal thermal conductivity − show a slight difference in relation to the experimental decay curves, especially at the beginning of the cooling process. This difference between numerical and experimental results is, in most cases, attributable to the fact that the initial thermograms are often contaminated by saturation, i.e., the reading is outside the calibration scale and no accurate measurement can be computed. Although the difference between the numerical and experimental curves begins to decrease from the second thermogram, for defects with aspect ratios D/z of $7/2$ and $7/4$ this difference is greater (see Figure 3.10 on top). This difference in behavior is due to the fact that the real distribution of energy deviates slightly from that considered in the model (Gaussian distribution function), causing divergence especially in the case of the defects located at the center of the specimen.

The quantitative verification of the numerical model is based on the correlation coefficient between the experimental and simulated temperature decay curves. The correlation is a measure of the relationship (or linear dependence) between two difference variables. Thus, a correlation coefficient of 1 denotes a total positive correlation between the two variables, whilst a correlation of 0 means no correlation (Montgomery and Runger, 2003). The correlation coefficient is calculated using the following expression:

$$C_{X_1X_2} = \frac{\sigma_{X_1X_2}}{\sigma_{X_1}\sigma_{X_1}} \tag{3.26}$$

In Eq. (3.26), $C_{X_1X_2}$ is the correlation coefficient between variables X_1 and X_2; $\sigma_{X_1X_2}$ is the covariance and σ_{X_1} and σ_{X_2} are the variances of X_1 and X_2, respectively.

The correlation coefficients were calculated for the temperature decays of all 25 defects, considering both models for thermal conductivity: series-parallel and Behrens-theoretical models. Results are depicted in Figure 3.11. It can noted that the temperature curves obtained with the Behrens-theoretical model showed better correlation coefficients than when using the series-parallel model. The averages of the correlation coefficients obtained from the Behrens-theoretical and series-parallel models are respectively, 0.966 and 0.957.

According to the results obtained from the qualitative and quantitative validation, the decay curves using the Behrens-theoretical model show better agreement with the experimental curves than the obtained with the series-parallel model. This is because the Behrens-theoretical model considers more structural characteristics of the fibers (shape, distribution and sizes) than the series-parallel model. For this reason, all of the results shown in the subsequent sections are based on the numerical-solution using the Behrens-theoretical model.

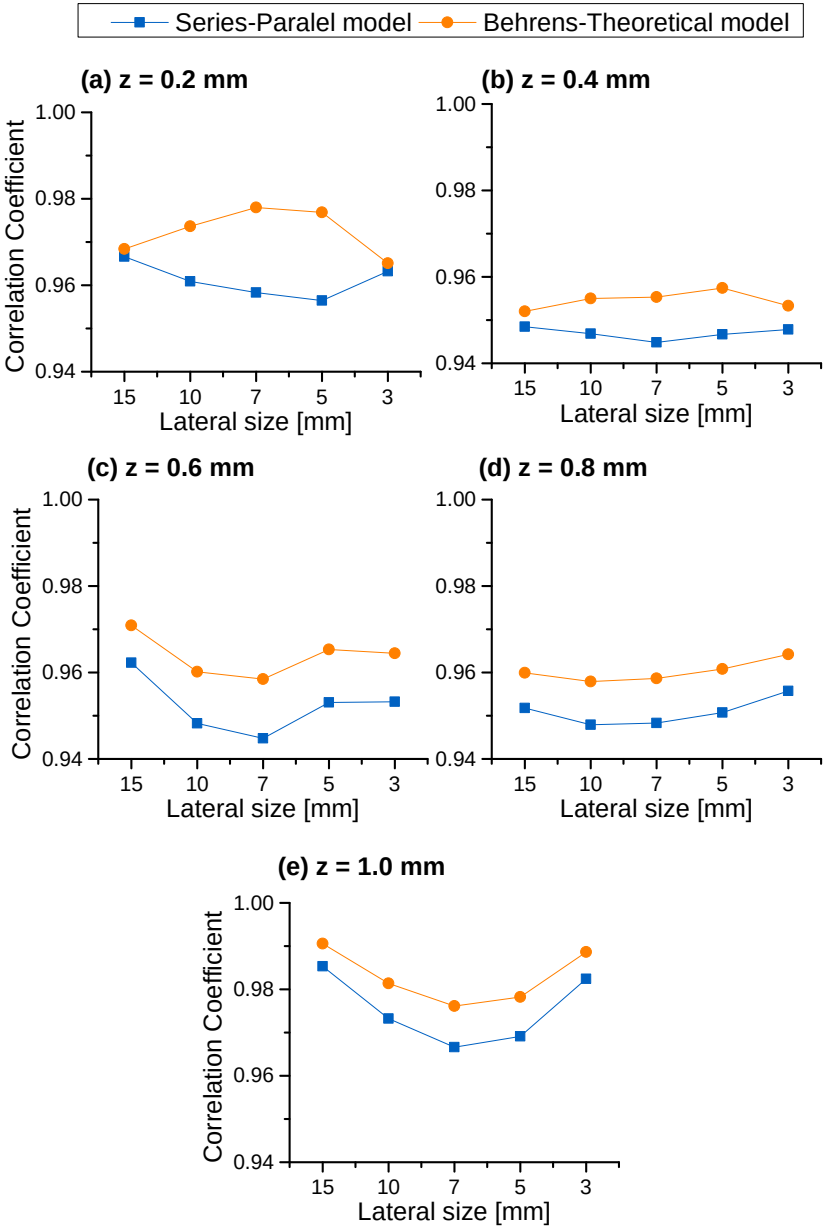

Figure 3.11: Correlation coefficients between experimental and numerical decay curves as a function of depth and lateral size of the defects.

3.5 Numerical Results

3.5.1 Thermal analysis of subsurface defects

The results and analysis presented in this section are based on the thermal behaviour during the cooling regime process of defective and non-defective zones, resulting from the thermal excitation of the specimen under study. Figure 3.12 (top) shows the thermal evolution curves for defects with $D/z = 7/0.4$ and $7/0.6$. Similarly, the evolution curve of a reference sound area has been included. These results were obtained through numerical simulation considering a uniform distribution of irradiation.

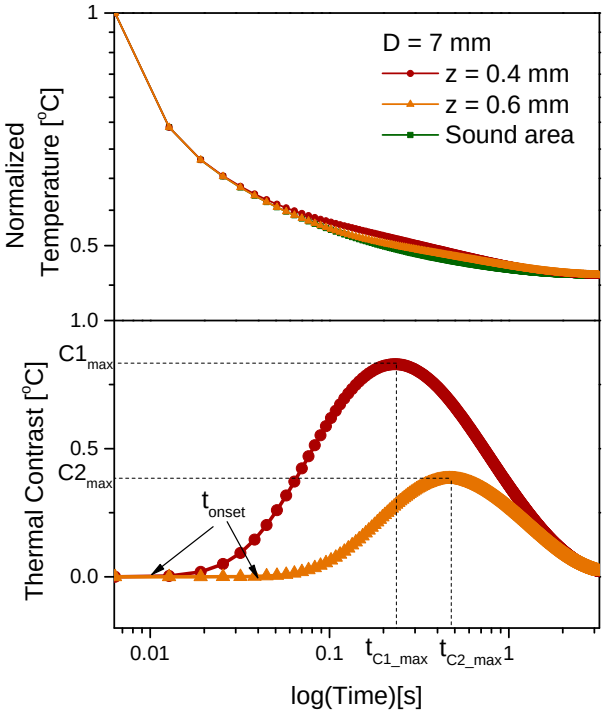

Figure 3.12: Normalized temperature decay (on top) and thermal contrast curves (on the bottom) for defects with $D/z = 7/0.4$ and $7/0.6$. Both results obtained by numerical simulation and considering a uniform distribution of irradiation.

Once the high-power short pulse is delivered to the material surface, the temperature of the specimen increases rapidly until it reaches the maximum value T_{max}, from which the cooling process begins. As can be observed in Figure 3.12 (top), the defects are detected when dissimilar or abnormal behavior of the decay curves for defective zones appears during the cooling process. The time at which the thermal decay of a defective region begins to present a dissimilar behavior compared to a reference zone is referred to as t_{onset} (onset time). This determines the moment at which the defect can be first detected in the thermogram sequence and, as will be further discussed, it is exclusively dependent on the depth of the defects.

Figure 3.12 (bottom) shows the evolution of the thermal contrast, which is defined as the temperature difference between defective and non-defective (sound) regions. It can be observe from the thermal contrast plots the two breaking points that characterized the thermal regime of the defects: the onset time t_{onset} and time of occurrence of the maximum level of thermal contrast (t_{max}). The thermal contrast defects with depths $z = 0.4$, 0.6, 0.8 and 1.0 *mm*, are plotted in Figures 3.13, 3.14, 3.15 and 3.16, respectively. It can be noted that deeper defects take longer to be detected (later onset time) independently of their lateral size. These results are in agreement to the following order of magnitude,

$$t \sim \frac{z^2}{\alpha} \tag{3.27}$$

which states that the observation time is directly proportional to the square of the depth and inversely proportional to the thermal diffusivity of the material. It can also be observed that for defects with the same lateral size, the deeper the defect the lower the maximum level of thermal contrast (C_{max}) and the longer its time of occurrence (t_{max}) will be. Maximum values for C_{max} were obtained for defects located at a depth of 0.4 *mm*, followed by a depth of 0.6 *mm*. The intensity of the thermal contrast for defects located at depths of 0.8 and 1.0 *mm* is very low and these defects are unlikely to be detected clearly without the use of data processing techniques or IR devices of high performance.

From the thermal contrast plots shown in Figures 3.13 to 3.16, the C_{max} and t_{max} values of each curve were computed and plotted as a function of depth. This analysis allows more detailed information to be obtained concerning the relationship between the maximum thermal contrast, its

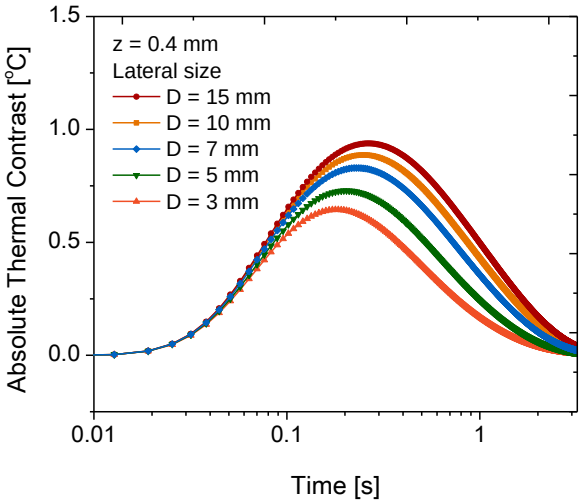

Figure 3.13: Thermal contrast evolution curves for defects depth $z = 0.4$ *mm*.

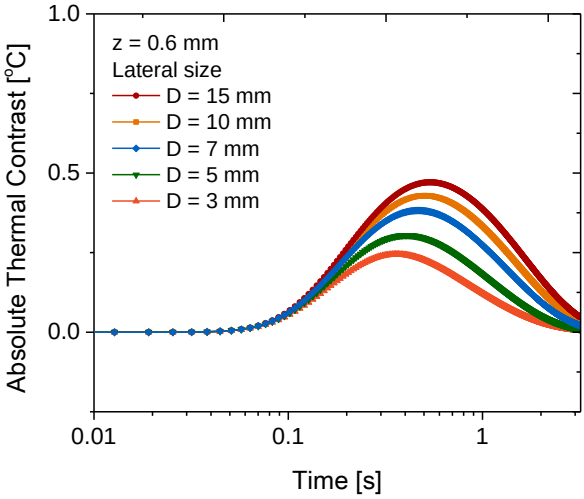

Figure 3.14: Thermal contrast evolution curves for defects depth $z = 0.6$ *mm*.

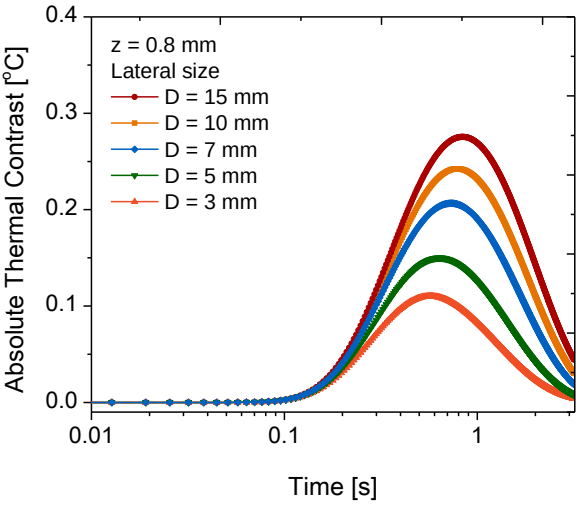

Figure 3.15: Thermal contrast evolution curves for defects depth $z = 0.8$ *mm*.

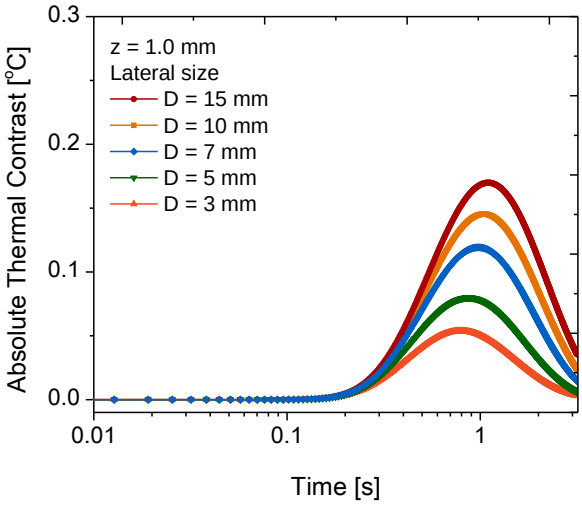

Figure 3.16: Thermal contrast evolution curves for defects depth $z = 1.0$ *mm*.

associated time of occurrence and the depth and lateral size of the defects. The results are shown in Figure 3.17.

Figure 3.17 (top) shows the maximum thermal contrast as a function of depth, considering defects with lateral sizes of 15, 10, 7, 5 and 3 *mm*. It is important to note that for defects with 0.2 *mm* of depth, the influence of the lateral size can be neglected and the relationship given by Eq. (3.27) is still valid. As the lateral size of the defect increases, the presence of lateral heat diffusion becomes more important in the thermal process and a 3D problem takes place.

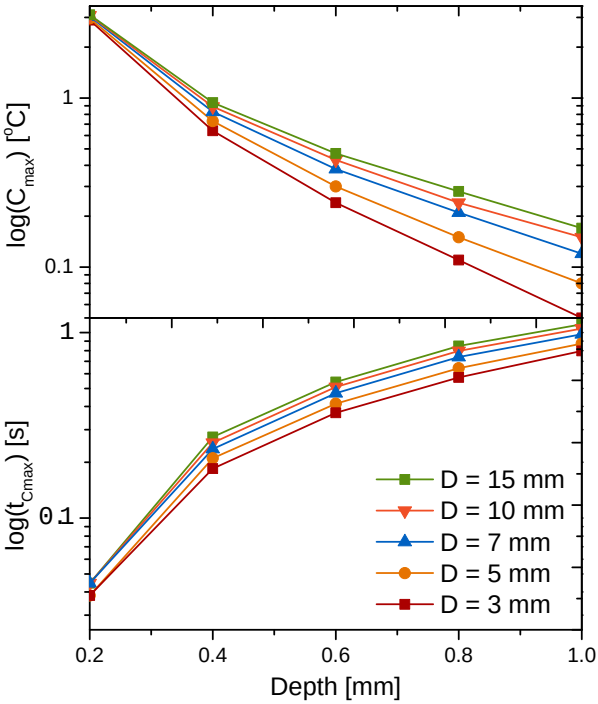

Figure 3.17: Maximum thermal contrast C_{max} and time of its occurrence as function of defect depth.

With regard to the time of occurrence of the maximum thermal contrast, Figure 3.17 (bottom) shows a similar pattern for defects located at 0.2 *mm*. Although the effect of the lateral size on t_{max} is weaker than in the case of thermal contrast, there is a relationship between the time of occurrence of the maximum thermal contrast and the lateral size and depth of the defects.

The relationship between defect depth and onset time is evident, as can be seen in Figure 3.18. The curve shows a strong correlation between the two variables and thus the influence of the lateral size of the defects on t_{onset} can be neglected. It is important to mention that the relation observed only applied to depths of 0.2 to 1.0 *mm*. Greater depths, or different thermal properties of the material, can lead to a different behavior.

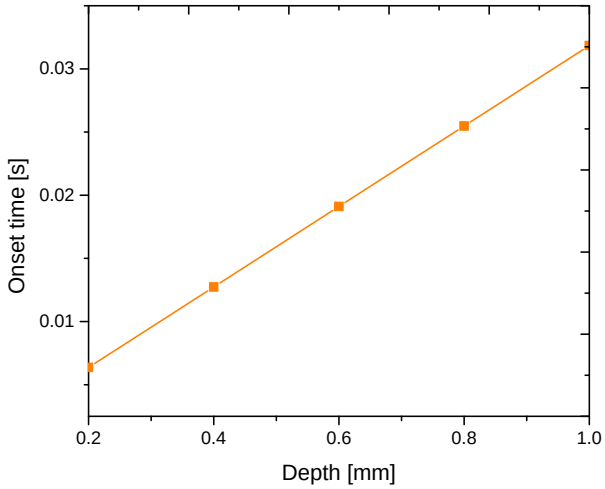

Figure 3.18: Onset time t_{onset} as function of defect depth.

3.5.2 Impact of non-uniform heating

Non-uniform heating is probably the most undesirable condition and it is an unavoidable problem in the configuration of the irradiation sources. Other factors that contribute to the non-uniformity are natural convection (especially over longer periods) and the optical properties of the surface.

In order to investigate the influence of non-uniform heating on the detection of defects and on the parameters previously discussed, a numerical simulation using a Gaussian distribution function was carried out and the results compared with those obtained when an ideal uniform distribution is applied to the surface. Figure 3.19 shows a comparison between two sets of thermograms obtained at different times and considering uniform and non-uniform irradiation distributions.

It is evident that the visibility of defects is greater when an ideal heat distribution is applied compared with non-uniform heating of the surface of the material. At 0.0064 s after the beginning of the cooling process (see Figure 3.19a) the temperature span of the thermogram using uniform heating is approximately 1 ^oC. On the other hand, when non-uniform heating is applied the span increases to approximately 1 ^oC. For longer periods, the temperature span with non-uniform heating continues to be greater than when an ideal heat distribution is applied, which affects the sensitivity of the PT technique in terms of the detection of deeper and smaller defects. For instance, it can be observed that all defects $-$ even those with the smallest aspect ratios $-$ are visible at 0.770 s when the heat is ideally distributed (see Figure 3.19c left column); however, when the heat is applied with a Gaussian distribution, the smaller and deeper defects ($D/z = 3/0.8$ and $3/1.0$) are almost undetectable.

The quantitative analysis of the defects is also strongly affected by non$-$uniform heating. Since most of the techniques used to quantify the depth and shape of defects are based on the computation of the thermal contrast (this topic will be further discussed in Chapter 6), a considerable contribution to the uncertainty in the quantification process is due to the non-uniform excitation. Figures 3.20 and 3.21 show respectively, a comparison between the C_{max} (maximum thermal contrast) and t_{max} (time of occurrence of the maximum thermal contrast) values computed from the thermal sequences obtained by numerical simulation, considering uniform and non-uniform heating.

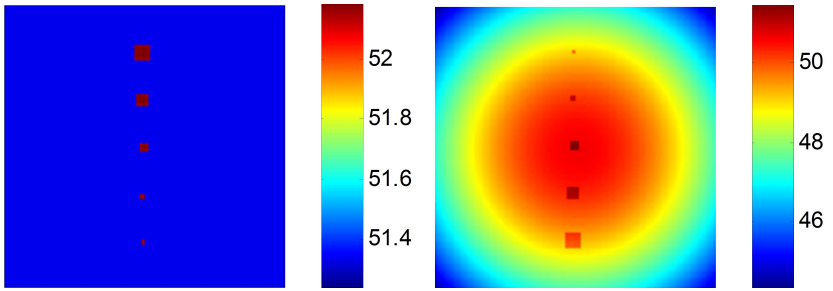

(a)

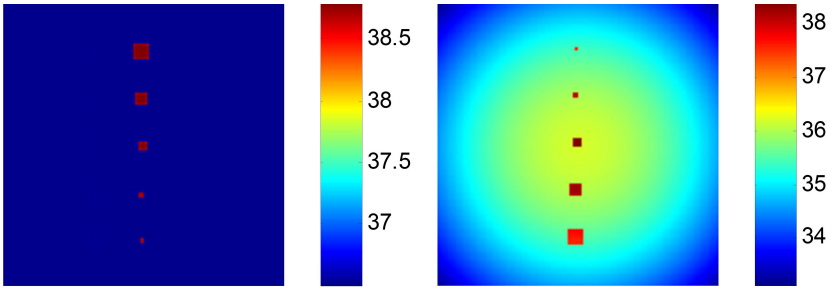

(b)

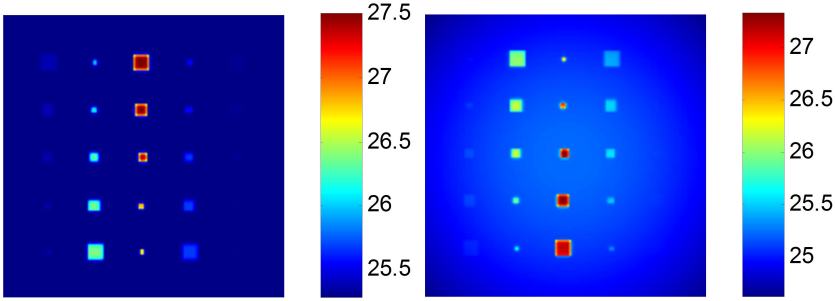

(c)

Figure 3.19: Comparison of simulated thermograms obtained considering uniform (left column) and Gaussian (right column) irradiation distribution functions. Thermal images correspond to (a) 0.00637, (b) 0.0127 and (c) 0.2547 s.

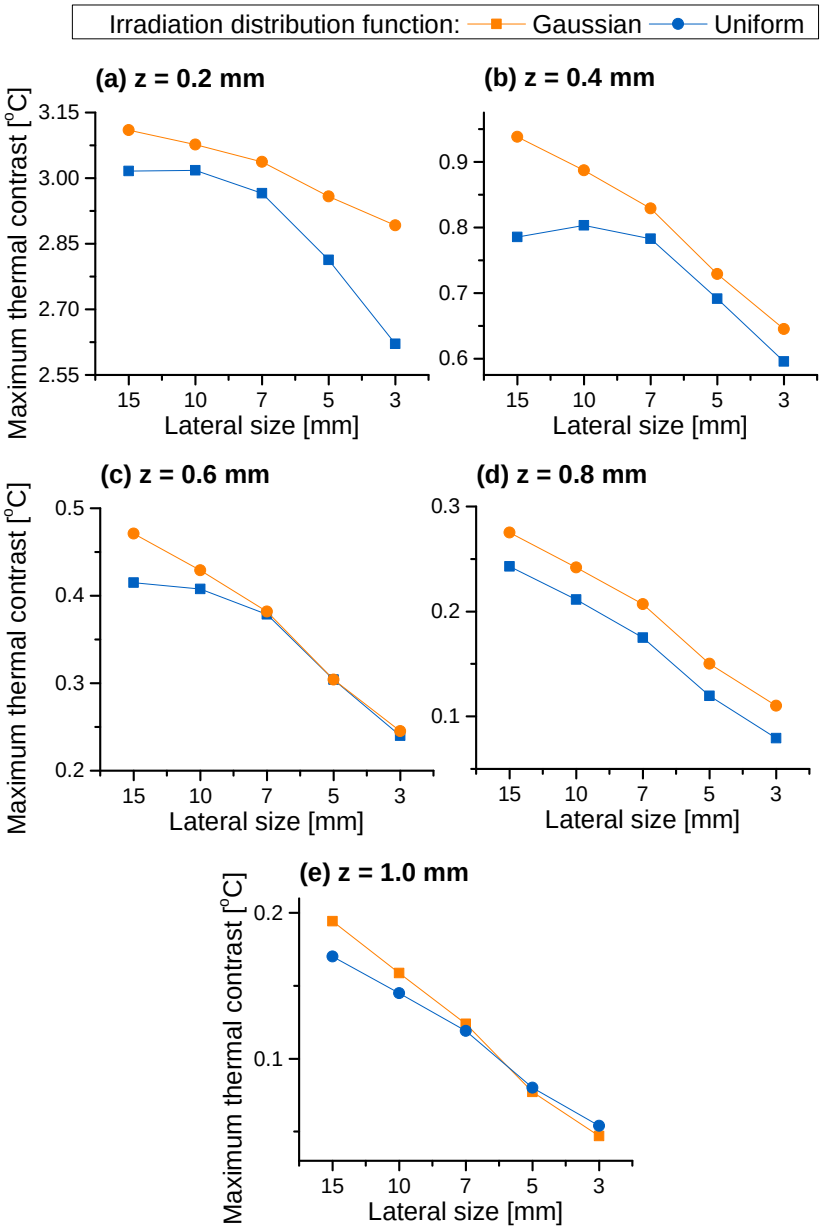

Figure 3.20: Maximum thermal contrast as function of depth, considering uniform and Gaussian distribution functions of irradiation.

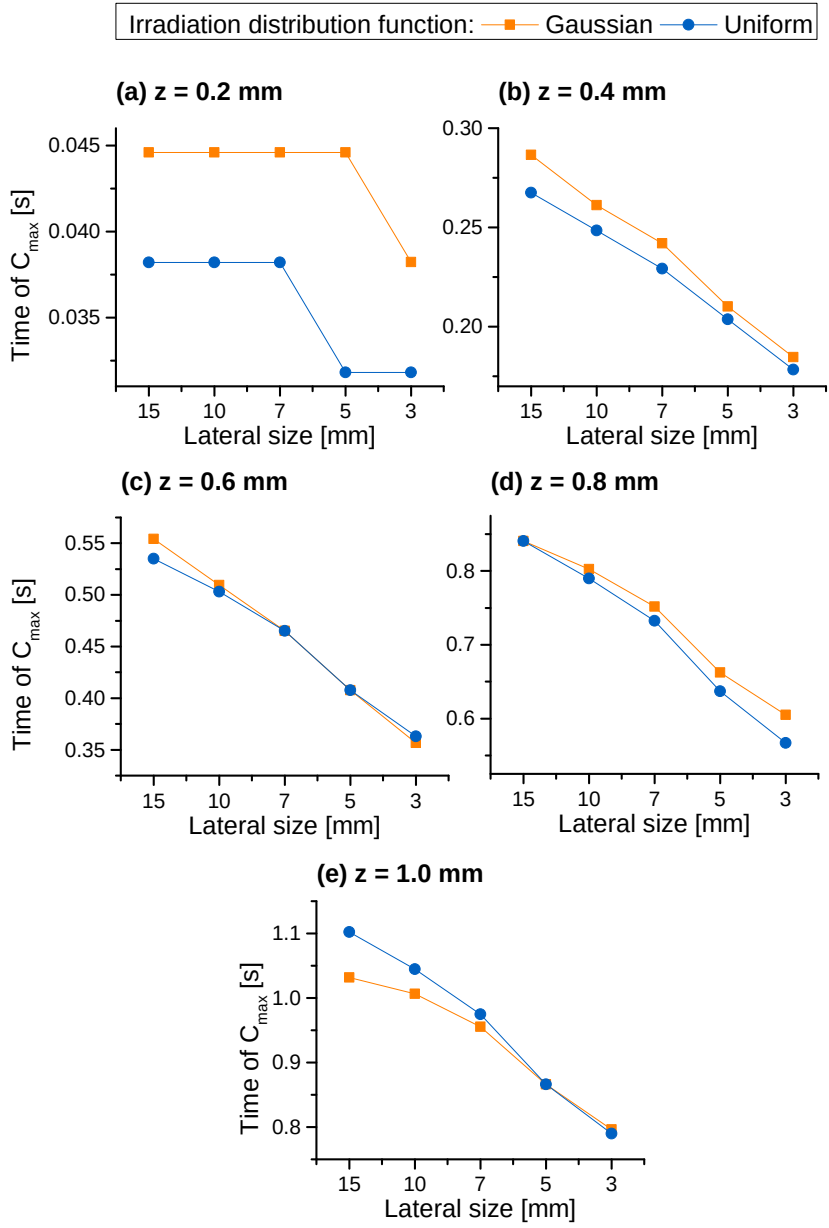

Figure 3.21: Time of occurrence of C_{max} as function of depth, considering uniform and Gaussian distribution functions of irradiation.

In general terms, it can be observed that as the depth increases, the difference between the values computed with uniform and non-uniform heating becomes greater. The maximum thermal contrast of defects with $z = 0.2\,mm$, are the most affected due to that they are located in the center of the specimen, where most of the energy is concentrated. Another important deviation between thermal contrast values obtained with Gaussian and uniform distribution can be seem in defects with $z = 0.4\,mm$ (see Figures 3.20 and 3.21). In this regard, defects with the largest lateral sizes ($D = 15$, 10 and 7 mm) are the most sensitive to non-uniform heating, which can lead to uncertainties when quantitative analysis is performed.

3.5.3 Impact of defect thickness

The results presented up to this point consider defects with a thickness δ value of 0.1 mm. In order to study the influence of this variable on the defect detectability level, a numerical simulation was conducted considering $\delta = 0.2\,mm$ and a non-uniform distribution of the irradiation. Figure 3.22 shows two simulated thermograms obtained at 0.0064 s (top) and 0.191 s (bottom) after the beginning of the cooling process. To the left of each thermogram there is a comparison of the temperature profiles along the dotted line, considering $\delta = 0.1\,mm$ and $\delta = 0.2\,mm$. It can be observed that the increase in the defect thickness produced an overall rise in the temperature field of the material surface. This behavior is interesting since the rise in temperature is not restricted to the defective regions. The influence of the defect thickness is more evident at later times.

It can also be observed in Figure 3.22b that the temperature profiles along the dotted line show that at 0.191 s the defects with a thickness of 0.2 mm provide greater thermal contrast than those with a thickness of 0.1 mm. The mentioned above can be seen in greater details in Figure 3.23, where is shown a comparison between the thermal contrast curves of defects with $\delta = 0.1\,mm$ and 0.2 mm, and considering aspect ratios of $5/0.1$ and $5/0.4$. As expected, higher thermal contrast values were obtained when the defect thickness was 0.2 mm. However, t_{max} and t_{onset} values remained constant when the defect thickness was increased, even though the value for the maximum thermal contrast showed a proportional increase. Figure 3.24 shows a comparison between the C_{max} values obtained in the two cases, showing that they are strongly correlated. In other words, C_{max} is proportional to defect thickness.

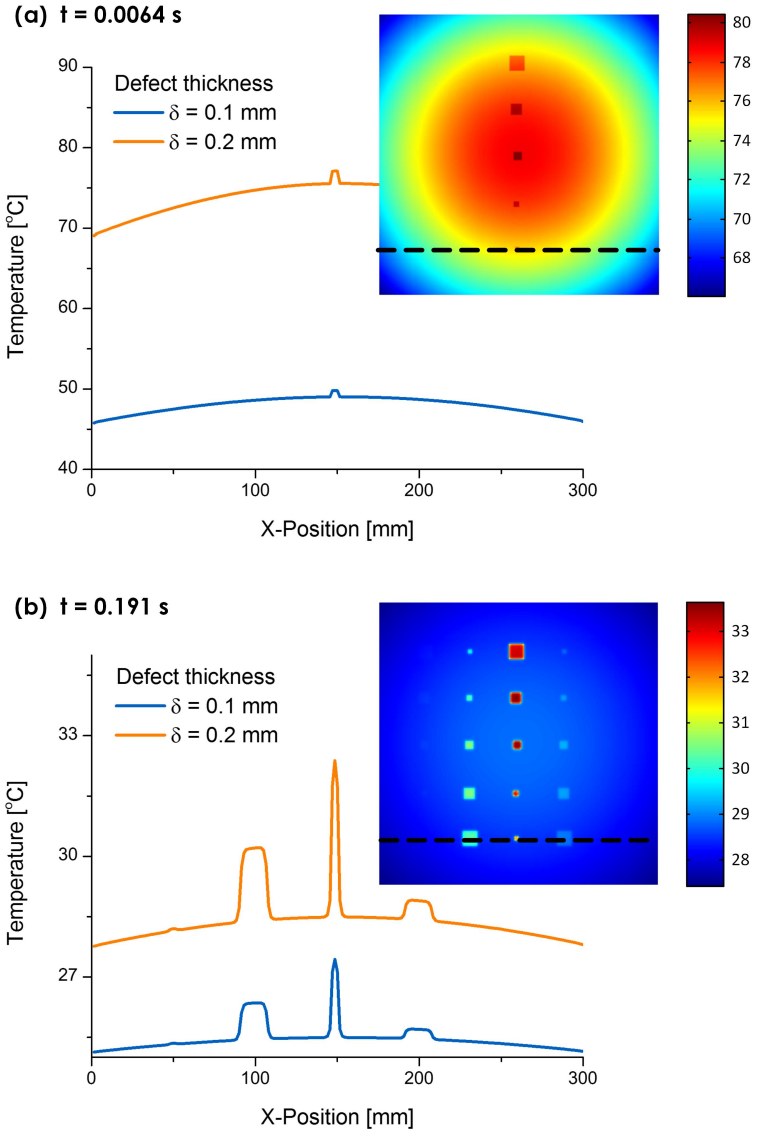

Figure 3.22: Simulated thermal profiles along $x-directions$ (considering defect thickness $\delta = 0.1$ and 0.2 mm and a non-uniform distribution of the irradiation) and thermograms obtained at (a) 0.0064 s and (b) 0.191 s..

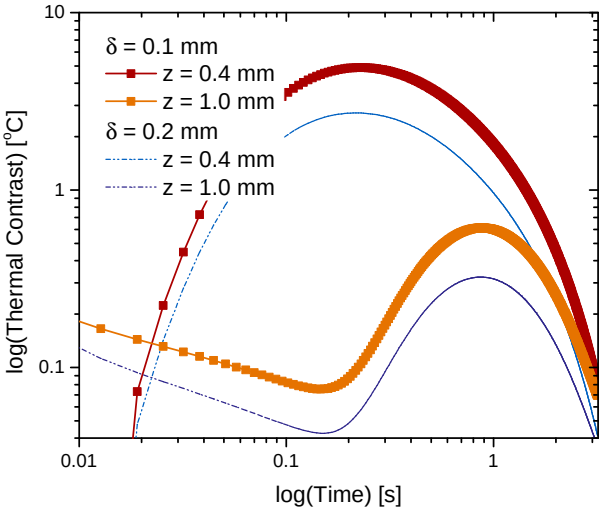

Figure 3.23: Thermal contrast for defects with lateral size $D = 5$ *mm* and depth $z = 0.4$ and 1.0 *mm*.

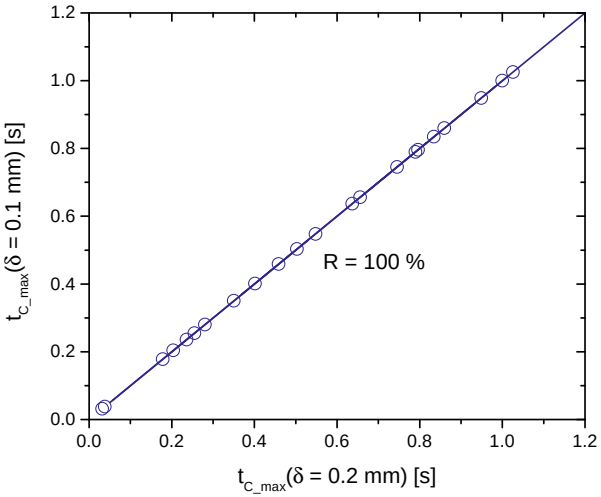

Figure 3.24: Correlation between computed values of time of occurrence of maximum thermal contrast for defect thickness $\delta = 0.1$ and 0.2 *mm*.

3.5.4 Impact of irradiation power density

The amount of energy delivered to the material surface during the application of the thermal excitation can lead to significant modifications in the detectability of defects. Figure 3.22 shows the influence of the irradiation power density on the thermal contrast which, as previously mentioned, is the variable used to estimate the detectability level of defects.

As shown in Figure 3.25, an increase in the radiant heat from 12.8 to 25.6 *kJ* produced an increase in the peak value for the thermal contrast C_{max} for all defects. The defects with depth $z = 0.2$ *mm* and 0.4 *mm* were the most sensitive to the increase of the radiant heat, with their C_{max} values increasing by approximately 100 %. As long as the depth of defects increases, the difference between C_{max} values obtained with different radiant energy becomes smaller. However, it is important to mention that a considerable increase of C_{max} is achieved in defects with depth $z = 0.2$ *mm* when the radiant energy was increased.

It is also worth mentioning that the time of occurrence of the maximum contrast of the defect, t_{max}, remained unaffected by the increase in the irradiation power. This is a very important factor since it means that the detection of the defects using the PT inspection technique can be enhanced without affecting the time at which the defects are more visible.

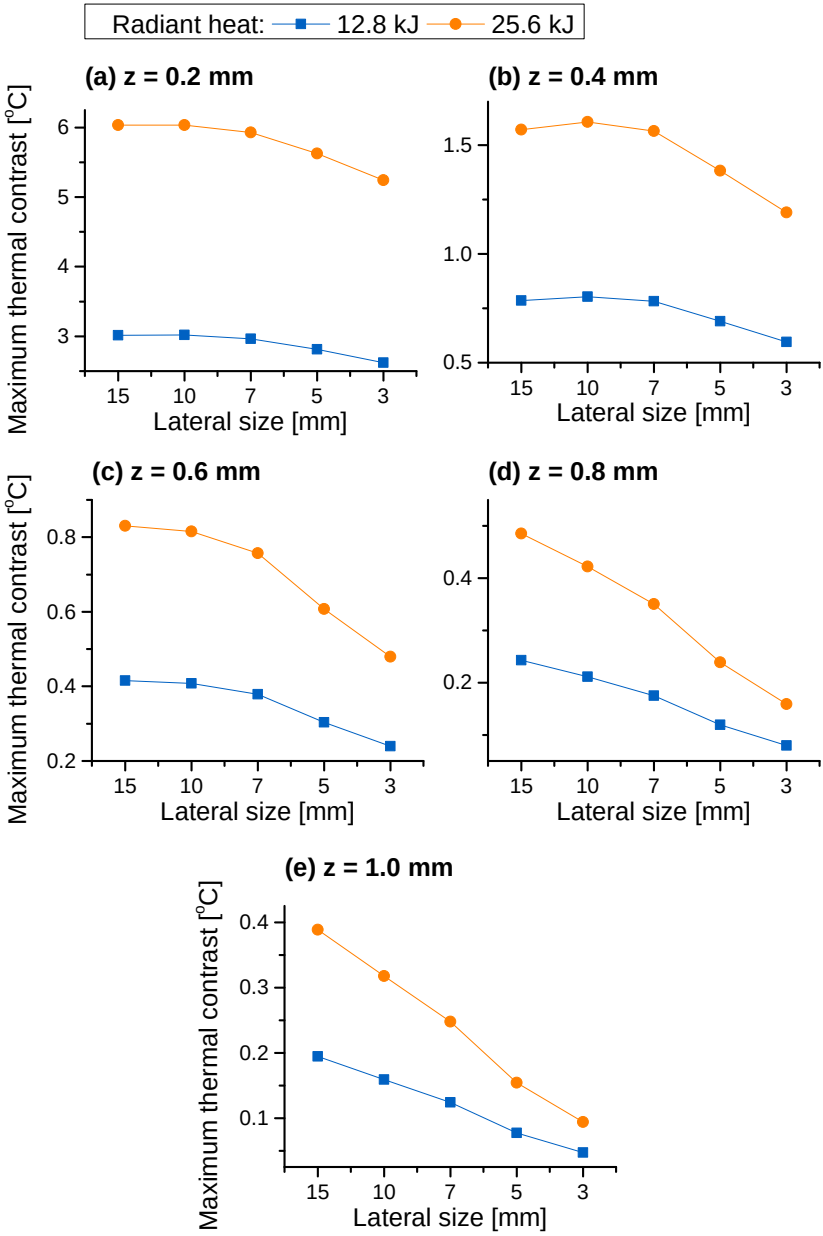

Figure 3.25: Comparison of C_{max} values considering radiant heat of I_{rad} = 12.8 kJ and 25.6 kJ. Values of C_{max} were obtained considering a Gaussian distribution function of irradiation.

Figure 3.26 shows the thermal contrast evolution curves for defects with aspect ratio $D/z = 10/0.2$, $10/0.4$, $10/0.6$, $10/0.8$ and $10/1.0$, considering a radiant heat of 25.6 kJ. Along with the thermal contrast plots are the moment at which the maximum thermal contrast takes place (marked with $\times$) when the radiant heat is 12.8 kJ. It can be seem that the time of occurrence of the maximum thermal contrast remains invariable when the amount of radiant heat is altered. Those results are only applicable when the distribution of surface irradiation remains the same.

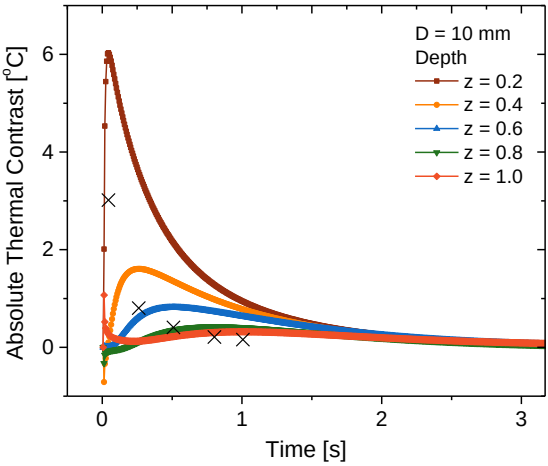

Figure 3.26: Thermal contrast curves for defects with lateral size $D = 10\,mm$, considering $I = 25.6\,kJ$. '$\times$' are the points of maximum thermal contrast for $I = 12.8\,kJ$.

3.6 Summary

Numerical simulation constitutes one of the main approach used to analyse the applicability of a given TNDT technique as well as to understand the involved phenomenology in cases where the experimental approach is almost impossible to perform. In regard to PT, most of the mathematical models used to explain the heat transfer that arises from the thermal excitation are based on simplified equations obtained from the solution of the 1D heat conduction equation, considering that the thermal pulse has the same temporal shape as the Dirac delta function. However, these simplified models only apply when the heat conduction regime is 1D, which in general terms is only valid for small temporal windows and shallower defects. For this reason, it has been developed in this survey a methodology to model and simulate the pulsed thermography inspection in anisotropic media.

The proposed model considers the heat conduction in 3D and transient regime. Furthermore, in the model are considered the thermal loses between the sample surface and the environment as well as the thermophysical properties of the laminated composite. In this sense, two different models have been tested: the Behrens-theoretical and the series-parallel model. The solution of the thermal model was carried out through the Finite Volume Method and the simulated results were validated with experimental data.

A parametric study was conducted and the analysis was based on the response of the informative parameters obtained during the cooling process regime: the onset time, maximum thermal contrast and its time of occurrence of all the 25 defects in the CFRP specimen. Several parameters were studied, such as the geometry of the defects and the the associated to the external thermal excitation.

Chapter 4

Thermographic Signal Processing

This Chapter provides an in-depth analysis and a critical review of three of the most used processing methods for pulsed thermography data: thermographic signal reconstruction (TSR), differential absolute contrast (DAC) and pulsed phase thermography (PPT). A methodology to study the performance of the the processing techniques is developed. The evaluation of the techniques is based on the signal-to-noise ratio at maximum signal contrast of thermographic signals of 25 *defects with different aspect ratios on two academic specimens made up of glass and carbon fibers. The discussion and analysis − which are presented in terms of the application, advantages and limitations of each technique − will provide the basis for the development of a more robust method of processing pulsed thermography data.*

4.1 Background

The inspection by pulsed thermography still presents great challenges, specially when inspecting highly-anisotropic materials such as the investigated in this Thesis. At larger times, blurring − the effects of lateral heat diffusion − becomes more predominant thus causing lost in defect visibility. Additionally, due to the nature of the measurement process, the signals acquired with the infrared camera are often contaminated with artifacts from external reflections, emissivity variations and also non-uniform heating caused during the application of the external excitation. This later is probably the most harmful and it is an unavoidable problem in the configuration of the heating sources, affecting in particular the detection of smaller and/or deeper defects (see for instance section 3.5.2). Due to these problems, PT, in its basic form, is generally limited to qualitative applications on large and near-surface defects.

Most of the problems that arise from blurring and non-uniform heating can be eliminated through the implementation of processing techniques to the temperature signatures obtained with the IR camera. In general terms, most of the techniques consist in a transformation of the temporal data to a different domain with the purpose of simplifying data analysis and obtain a new variable to deal with. This new variable may improve the defect detection, especially to those that are more sensitive to the effects of lateral heat diffusion and non-uniform heating.

Thermographic signal processing is a topic that has been subject of investigation by several researchers (Hidalgo-Gato et al., 2013; Ibarra-Castanedo et al., 2009). Currently exits a wide spectrum of algorithms for the processing of thermographic images, most of them being applied to pulsed thermography inspection. Figure 4.1 shows a compendium of the principal methods currently available, standing out two streams of algorithms: single image and image sequence techniques. Single image techniques aim to perform − at once − spatial processing of single thermograms collected during the acquisition. These methods are generally based on mathematical and statistical operations such as mean substraction, filtering, histograms and variance analysis. On the other hand, image sequence techniques are intended to processing the data on space and time and require complex computations of a sequence or stack of images that describes the temporal evolution of the thermal response. Although these methods are generally time-consuming and requires large computational resources, they can provide quantitative information of the subsurface discontinuities.

As depicted in Figure 4.1, there are four categories of processing methods within the group of images sequence techniques: thermal contrast, space transformation, heat conduction and statistical multivariate -based techniques. The simplest processing − and analysis − methods of PT data are the thermal contrast-based techniques, which rely on the comparison of a defective and non-defective region. There are available in the literature several formulations of thermal contrast, each one with particular definitions and applications (see section 2.2.4).

Space transformation-based techniques enable the representation of temporal signals into a combination of sinusoidal waves or wavelets. The Discrete Fourier Transform (DFT) constitutes the basis of pulsed phase thermography (PPT), enabling to go back and forth using the duality principle between the frequency and time domains. The idea behind the Fourier Transform is that it is possible to reconstruct any $1D$ function

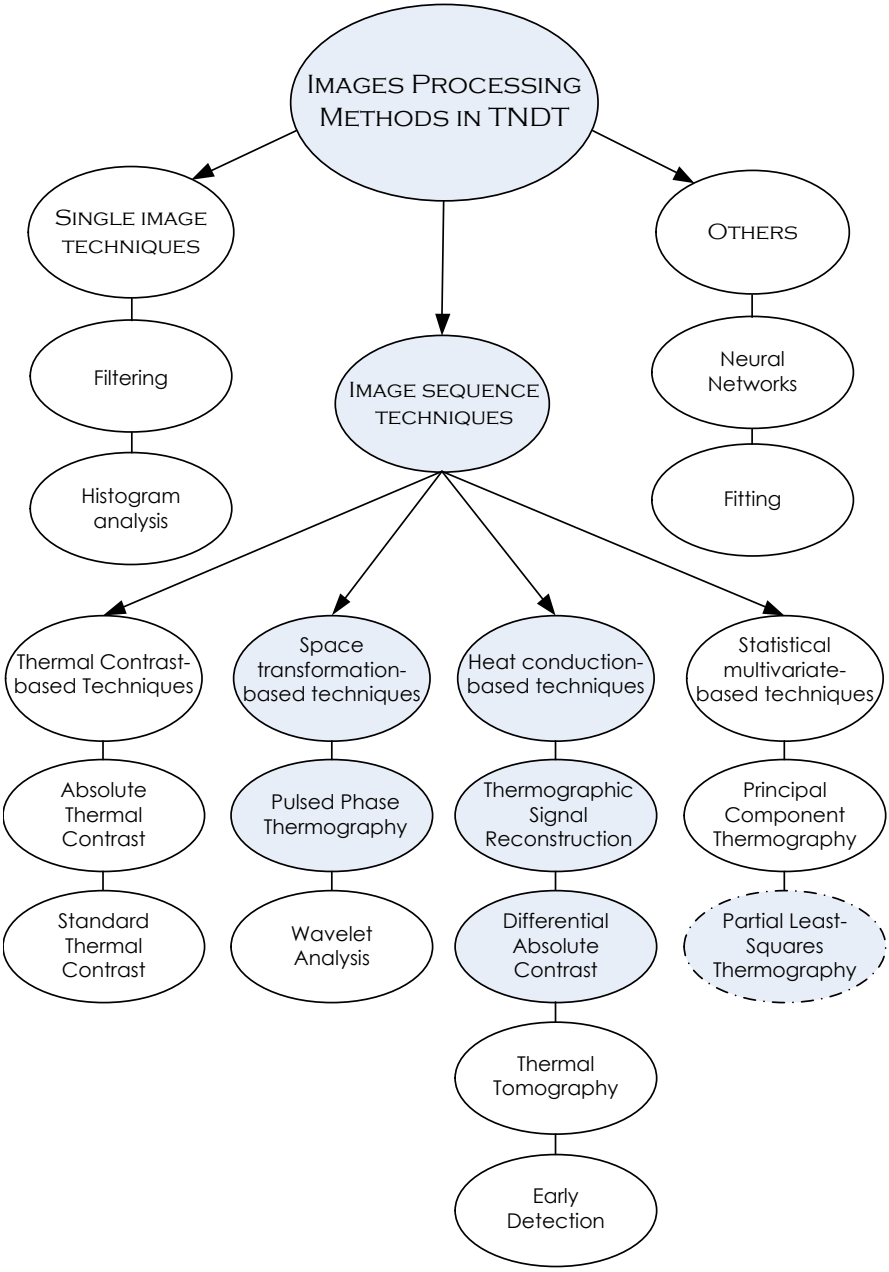

Figure 4.1: Current scenario of data processing methods in thermal nondestructive testing (TNDT).

at a particular space (e.g. temperature evolution in time) as a summation of sinusoidal terms of increasing frequency. In addition to the DFT, other transformations are possible such as the Discrete Wavelet Transform (DWT). The wavelet transform (WT) was intended as an alternative transformation algorithm to better represent transient functions. Instead of using waves (e.g. the sinusoids) as in the FT, the WT uses wavelets (i.e. waves of limited duration) as its basis functions. The use of wavelets allows processing the information at different scales (or resolutions) by decomposing the signal into stretched and scaled replicas of a base wavelet, which allows a better approximation of sharp functions (Ibarra-Castanedo et al., 2006).

Heat conduction-based techniques constitute the core of the processing methods applied to pulsed thermography data. As its name implies, these methods are based on the solution of the $1D$ heat conduction equation. In spite of being physically-base methods, they are restricted to situation in which the thermal regime of the heat conduction is $1D$. However, the improvement of defect visibility is considerable greater especially in defects with larger aspect ratio D/z. Finally, statistical multivariate-based techniques represent a new trend of processing and analysis of thermographic images. These techniques are based on statistical concepts to transform the PT data into a new subspace called of latent variables. Two techniques are based upon this concept: principal component thermography (PCT) and the new-introduced partial least squares thermography (PLST).

From the presented scenario of processing methods, this survey analyses the performance of three of the most attractive methods for PT data: differential absolute contrast (DAC), thermographic signal reconstruction (TSR) and pulsed phase thermography (PPT). These techniques has been widely reported as the most suitable processing methods for pulsed thermography data (Ibarra-Castanedo et al., 2009; Oswald-Tranta and Shepard, 2013). The mathematical concepts of the techniques are briefly revised, followed by the implementation on a set of thermographic images collected during a PT inspection on two laminated composites made up of glass and carbon fibers (specifications of plates CFRP006 and GFRP006 are in Appendix). The SNR at maximum signal contrast is the quantity adopted to evaluate the performance of each technique. The discussion begins with techniques whose analysis is performed in the time-domain: DAC and TSR.

4.2 Time-domain Processing Techniques

4.2.1 Differential absolute contrast, DAC

DAC (Pilla et al., 2002) is a classical processing technique whose main goal is to eliminate the downside of selecting a sound area when performing classical thermal contrast computations (see section 2.2.4). Based on the solution of the $1D$ heat diffusion equation, DAC estimates the temperature of a sound area (T_{sa}) at time t', which is computed locally assuming that on the first few images all points behave as a sound area. Thus, the thermographic data obtained from a PT experiment can be approximated to the $1D$ solution of heat equation through following expression (Pilla et al., 2002):

$$\Delta T_{DAC} = T_d(t) - \sqrt{\frac{t'}{t}} \cdot T(t') \tag{4.1}$$

The first step in the implementation of the DAC method is to define t' as a given time value between the instant when the thermal excitation is applied, and the precise moment when the first defective spot appears on the thermogram. Figure 4.2 shows the methodology implemented to find a proper t' through the use of IrView (Klein et al., 2008) − a graphical user interface developed to this aim − considering a defect with aspect ratio $D/z = 10/0.2$. Figure 4.2 also shows the estimated thermogram used as a reference. It can be observed from this thermogram that the frames following the flash excitation are often contaminated with saturation and effects associated to the non-uniform excitation. This last may affect the performance of DAC. Furthermore, it is important to emphasize that Eq. (4.1) is a good approximation at earlier times; as time elapses, Eq. (4.1) will diverge from the semi-infinite case. The last mentioned is exemplified in Figure 4.3, where are shown two thermograms obtained after being processed with DAC, at two different times.

It can be noted from Figure 4.3 that, as time elapses, the effectiveness of the technique is affected as a consequence of the divergence between actual measurement and the solution provided by Eq. (4.1). The divergence from the semi-infinite model affects primary deeper defects. Despite this, DAC provides an improvement on defect visibility and reduction of artifacts caused by non-uniform heating, specially at the beginning of the cooling process (see the temperature profiles along the dotted lines).

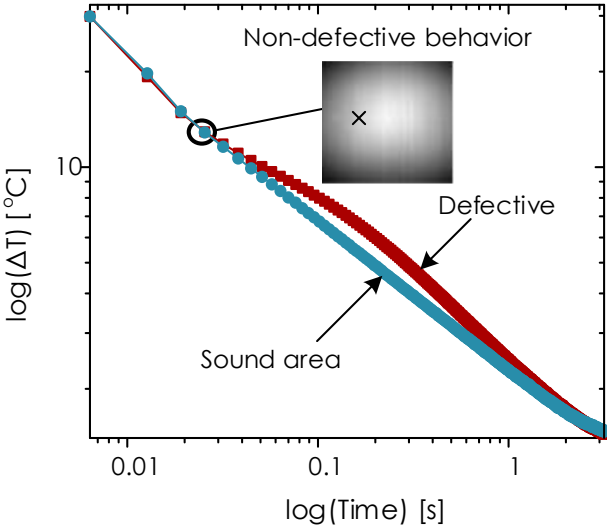

Figure 4.2: Implementation of DAC considering decay curves (defective and non-defective) of a defect with aspect ratio of $D/z = 10/0.2$ in the CFRP specimen. On the bottom are plotted the thermal profiles of both images along the dotted line.

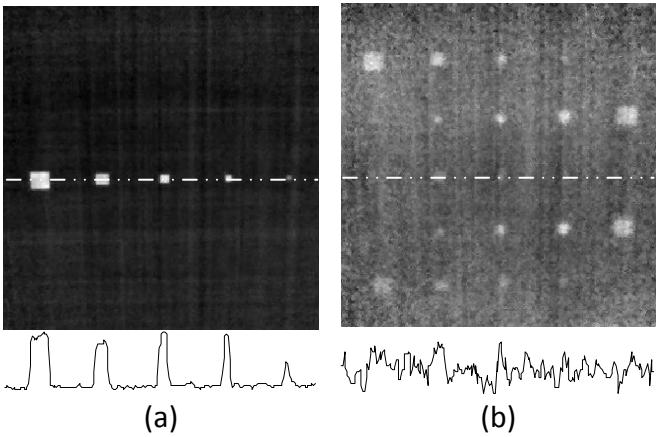

Figure 4.3: Processing results with DAC of the CFRP specimen inspected by pulsed thermography, at (a) $t = 0.0254\ s$ and (b) $t = 1.91\ s$.

4.2.2 Thermographic signal reconstruction, TSR

TSR (Shepard, 2001; Shepard et al., 2002) is an attractive processing method specially conceived to be used in PT data. This technique brings important improvements and advantages over PT raw data, the most significant being the simplicity and accuracy of quantitative measurement, increase of temporal and spatial resolution, reduction of high frequency noise and the ability to produce time derivative images. The basis of TSR is the use of a low order polynomial function to reconstruct − or to fit − the temperature evolution cooling profiles obtained from an inspection by PT. Assuming that the temperature decay of a defect-free region behave in a similar manner as the solution of the $1D$ heat diffusion equation, the temperature evolution of a non-defective area can be written in logarithmic form as:

$$\ln(T - T_o) = \ln(\frac{Q}{e}) - \frac{1}{2}\ln(\pi t) \tag{4.2}$$

In Eq. (4.2), T_0 is the initial temperature whereas T is the variable temperature; Q is the applied heat energy as external stimulation, e is the thermal effusivity of the material [defined as $e = (k\rho c_p)^{1/2}$] and t is the time. From Eq. (4.2) it is possible to model the temperature evolution of a free-defect region as a fixed and straight line with slope $= -0.5$. This linear and fixed-slope behavior is independent of the thermal properties and the applied heat flux [see second term of Eq. (4.2)]. Obviously, defective regions will diverge from linearity. The regression proposed by Shepard (2001) consisted on the use of an m-degree polynomial function to approximate the logarithmic time dependence of thermographic data. This polynomial function can be written as:

$$\ln(T - T_o) = a_o + a_1\ln(t) + a_2[\ln(t)]^2 + ... + a_m[\ln(t)]^m \tag{4.3}$$

As can be observed in Eq. (4.3), one of the main steps in the regression process in TSR is the selection of the appropriate number of coefficients m to fit the thermographic data. For isotropic materials, a good correspondence between acquired data and fitted values can be achieved setting m to 4 or 5. Nevertheless, when working with anisotropic materials such as those considered in this work (carbon fiber reinforced polymers) the number of coefficients should be carefully selected in order to avoid higher residuals between fitted and experimental data.

As already mentioned, one of the main contributions of TSR is the ability to produce time derivative-images without additional noise contribution. First and second time derivative-images are obtained using the following expressions:

$$\frac{d}{dt}\ln(\Delta T) = \sum_{n=1}^{N} n a_n \ln(t)^{n-1} \tag{4.4a}$$

$$\frac{d^2}{dt^2}\ln(\Delta T) = \sum_{n=2}^{N} (n-1) n a_n \ln(t)^{n-2} \tag{4.4b}$$

being $\Delta T = T - T_o$. The main achievement of the time derivative-images is the apparent reduction of blurring (lost of contrast due to lateral heat diffusion), which is a consequence of the fact that the derivative-images provide earlier indications of both, the onset time and time of occurrence of the maximum contrast, than normal contrast images of the same target (Shepard, 2007). As is shown in Figure 4.4, with synthetic temperature data the defect becomes visible approximately in the 5^{th} thermogram. However, using the first and second time derivative-images the onset of the defect is reduced to the 4^{th} and 3^{th} frames, respectively.

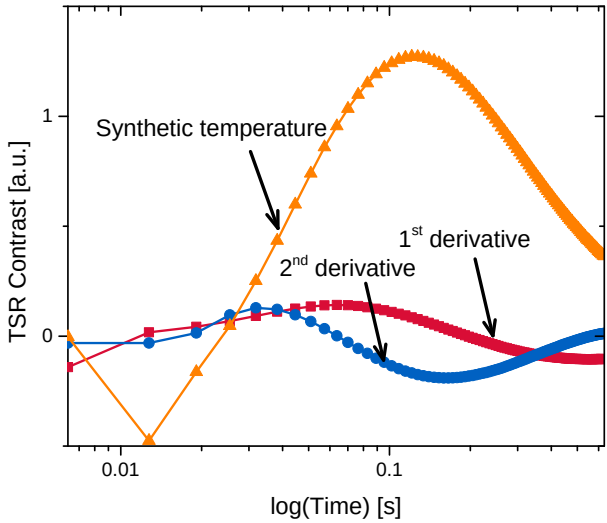

Figure 4.4: Contrast curves of synthetic thermal data, 1^{st} and 2^{nd} time derivative-images, for a defect with $D/z = 10/0.2$ in the CFRP specimen.

4.3 Processing and Analysis in the Frequency Domain

4.3.1 Pulsed phase thermography, PPT

PPT is a processing technique introduced by Maldague and Marinetti (2002). The basis of this technique is the superposition principle, which states that a time-domain response $T(t)$ can be decomposed into a frequency-domain response using Fourier expansion:

$$T(x,t) = \sum a(\omega_n) T(z,\omega_n,t) \tag{4.5}$$

In Eq. (4.5), $T(z,\omega_n,t)$ is a plane thermal wave of angular frequency ω_n propagating in the $z-direction$ and $a(\omega_n)$ is a measure of the strength of this component in the frequency concerned. Physically, the diffusion of heat from the surface into the material can be understood in terms of the propagation of these thermal waves into the solid away from the surface. The different frequency components will suffer different amounts of attenuation, increasing or decreasing the penetration of each of the thermal waves (Almond and Patel, 1996). It is because of this duality between the transient and harmonic problem that PPT is considered as the link between Pulsed and Lock-in Thermography (Ibarra-Castanedo et al., 2007b).

In PPT the data is transformed from the time domain to the frequency domain using the one-dimensional discrete Fourier transform (DDT):

$$F_n = \Delta t \sum_{k=0}^{N-1} (k\Delta t) \exp^{-\frac{j2\pi k}{N}} = Re_n + Im_n \tag{4.6}$$

where j is the imaginary number, n designates the frequency increment ($n = 0,1,...,N$), Δt is the sampling frequency interval, and Re and Im are the real and imaginary parts of the transform, respectively. Although from Eq. (4.6) is possible to obtain amplitude A and phase ϕ, fast Fourier transform algorithms are available in commercial in packages such as Matlab®.

PPT offers interesting features specially when working with phase data. The phase maps, or phasegrams, enable measuring the difference between the sinusoidal oscillations of two or more thermal waves. As explained by the harmonic heat transfer theory, the phase difference (or phase lag) can be associated to the location of internal barriers – or defectives zones at the interior of the material – that produces internal reflections of thermal waves between the interface of the defect and the

surface of the specimen. Thus, along with a considerable improvement in the reduction of environmental reflections, emissivity variations and non-uniform heating, phase data enables quantitative analysis of defects (Ibarra-Castanedo and Maldague, 2005; Maldague and Ibarra-Castanedo, 2004).

In spite of the advantages in terms of reduction of non-uniform artifacts and external reflections, PPT is affected by harmonic oscillations. Figure 4.5 shows the phase profiles for defective and sound areas and the corresponding phase contrast, considering a defect located at 2 *mm* depth in the carbon fiber reinforced polymer specimen. It can be noted at higher frequencies PPT is highly affected by higher-order oscillations. These side effects of PPT affect mostly shallower defects (associated to high frequencies) rather than deeper defects (related to low frequencies).

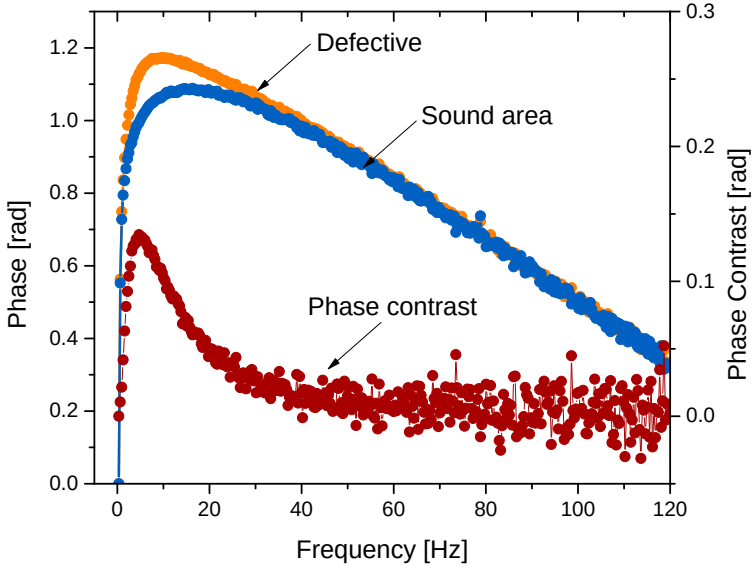

Figure 4.5: Phase profiles (for defective and sound area) and phase contrast of a defect with $D/z = 10/0.2$ in the CFRP specimen.

As already explained, all three techniques possess advantages and limitations which depend mainly on parameters related to the subsurface defects. Next section is dedicated to describe the methodology adopted to compute the signal-to-noise ratio.

4.4 Quantification of Signal-to-Noise Ratio at Maximum Signal Contrast

This section section discusses the characterization of the signal-to-noise ratio (SNR) at maximum signal contrast. A method of distinguishing discontinuities and sound areas is first presented, followed by the methodology implemented to analyze the performance of the signal processing techniques based on the SNR at maximum signal contrast.

4.4.1 Methodology of selection of defective and sound areas

The variable contrast has been established as a standard variable to determine how strong or how weak is the signal of a defect, or in other words, its visibility. The variable contrast is defined as:

$$C = \triangle S(t) = |S_d(t) - S_{sa}(t)| \tag{4.7}$$

where $S_d(t)$ and $S_{sa}(t)$ are respectively the temporal signals of defective and non-defective regions. These signals may be temperature, phase or intensity of 1^{st} and 2^{nd} derivative images at a particular frame. In similar manner as in section 3.4, signals from defective and sane regions are computed using the following expressions:

$$S_d(t) = \sum_{i=1}^{nx} \sum_{j=1}^{ny} \frac{S(i,j)_d}{nx \cdot ny} \tag{4.8a}$$

$$S_{sa}(t) = \sum_{i=1}^{nx} \sum_{j=1}^{ny} \frac{S(i,j)_{sa}}{nx \cdot ny} \tag{4.8b}$$

Figure 4.6 shows the defective and sane regions over which $S_d(t)$ and $S_{sa}(t)$ are computed. The area over which $S_{sa}(t)$ is calculated is twice the lateral size of the defective region. This methodology of selection of defective and sound areas was implemented in order to avoid the requirement to establish a reference region as a sound area, which in most cases the computation of $\triangle S(t)$ will differ as a function of the localization of the non-defective region, mainly because of the effects of non-uniform heating [see for instance Ibarra-Castanedo et al. (2007a)].

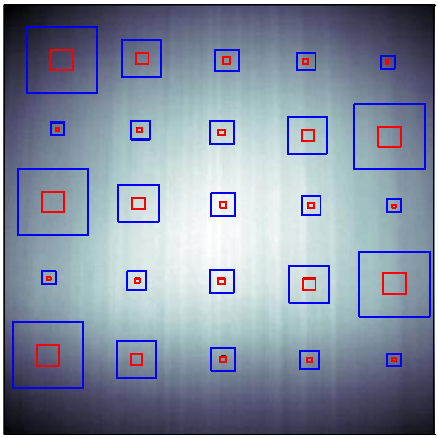

Figure 4.6: Selection of defective (red squares) and non-defective (blue squares) regions for different lateral sizes of defects.

4.4.2 Signal-to-noise ratio

The quantity adopted to characterize the performance of the signal processing techniques is the signal-to-noise ratio (SNR). The quantification of the SNR will allow to analyze the relationship between the desired signal strength and the level of background noise at the maximum signal contrast. From this quantification it is also possible to determine the advantages and limitations of each processing technique based on the inspection parameters, thermal properties of the material and aspect ratio of defects. SNR is calculated using the following expression (Grinzato et al., 1995; Ibarra-Castanedo et al., 2009):

$$SNR = \frac{C^2}{\sigma^2} \tag{4.9}$$

In Eq. (4.9), C^2 and σ^2 are respectively the amplitude of the signal and background noise. Signal amplitude is calculated using Equations (4.8), while the background noise is determined from the variance over the entire sound area. The variance is calculated using the following expression:

$$S_{sa}(t) = \frac{\sum_{i=1}^{n} (S_i - \bar{S})^2}{n-1} \tag{4.10}$$

In Eq. (4.10), $\bar{S}$ is the mean value of the signal and n is the total numbers of pixels that comprise the sound area. Eq. (4.9) can also be expressed in logarithmic decibels. In decibels, the SNR is defined as (Huynh-Thu and Ghanbari, 2008):

$$SNR = 10 \cdot \log_{10} \left(\frac{C}{\sigma} \right)^2 = 20 \cdot \log_{10} \left(\frac{C}{\sigma} \right) \tag{4.11}$$

It is important to note that each calculation using Equations (4.9) to (4.11) is performed on every frame. Since it is of interest to quantify the maximum SNR possible, both the amplitude of the signal and the background noise are calculated at the maximum value of the contrast. In terms of C_{max}, the equation to compute the SNR at maximum signal contrast and in decibels is expressed as:

$$SNR_{C_{max}} = 20 \cdot \log_{10} C_{max} - 20 \cdot \log_{10} \sigma_{C_{max}} \tag{4.12}$$

As already discussed in Chapter 3, the selection of C_{max} is inherent to a particular defect. Thermal properties of the specimen, as well as the aspect ratio of the defects and the method used as a processing technique will determine the time of occurrence of C_{max}.

In next section is described in details the methodology adopted to calculate the SNR.

4.4.3 Methodology

Figure 4.7 shows the methodology adopted in this work to analyze the performance of the signal processing techniques based on the SNR at maximum signal contrast. This methodology is conceived as a standard method to be use in all the three techniques subject to discussion in this thesis.

The experimental data consisted on a set of IR thermal images obtained through the inspection by PT of the carbon and glass fiber reinforced polymers (CFRP006 and GFRP006 specimens) using the system

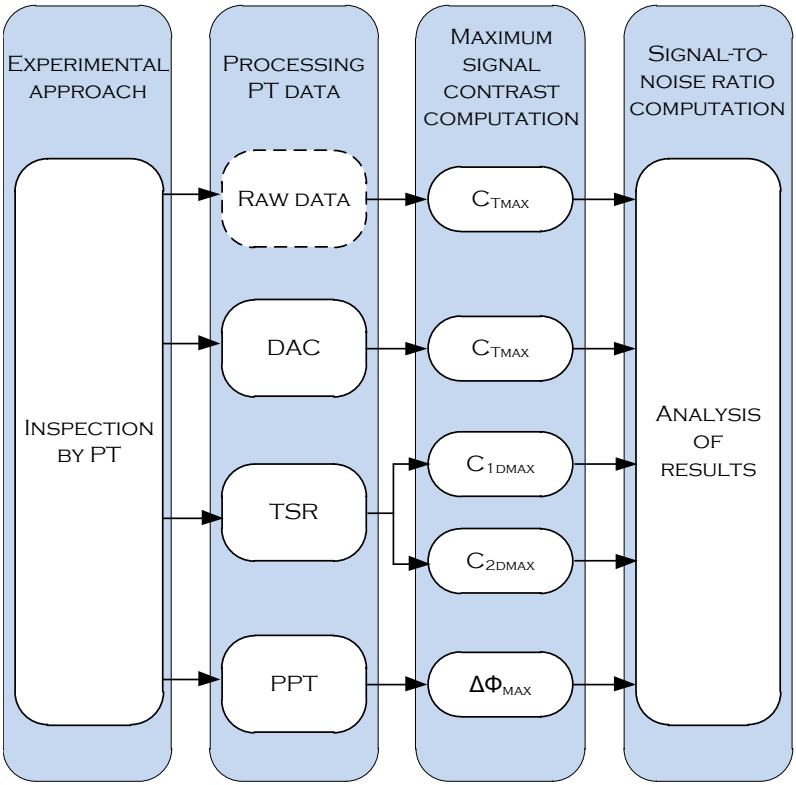

Figure 4.7: Methodology adopted to calculate the SNR at maximum signal contrast.

introduced in Chapter 2. Both specimens were inspected using a fixed acquisition frequency (f_s) of 157 Hz, which is the maximum full-frame rate achieved (320x256 pixel array). Furthermore, a total of $N = 1000$ frames − maximum storage capacity of the IR camera − were collected in each inspection. Once the inspection is carried out, the complete thermal sequences of both experiments were processed using TSR, PPT and DAC. It is important to point out that no signal treatment was applied (reduction of truncation window, increase or reduction of sampling parameters) to the raw data in any of the techniques. However, since the only basis used to select the acquisition parameters was the use of the maximum frequency allowed by the IR camera, SNR results may vary using other acquisition parameters.

The next step after the application of the processing techniques is the computation of the maximum signal contrast. This is a crucial step and is accomplished using Equations (4.7) to (4.8). Along with C_{max}, t_{max} (time of occurrence of C_{max}) is computed as well, which is necessary also to calculate the noise over the sound area. As already mentioned, C_{max} and t_{max} are inherent to some characteristics associated with the defects (depth and lateral size), thermal properties of the specimens and also the processing technique. Finally, the last stage of the methodology is the analysis of the performance of the signal processing techniques based on the computation of the SNR [Eq. (4.12)].

In the next section are presented the results and analysis of the computed values of SNR at maximum signal contrast.

4.5 Comparative Results and Analysis

The results to be presented herein are divided in two sections, each corresponding to the analysis of the data processing techniques in the specimens CFRP006 and GFRP006. The discussion begins with results obtained in the carbon fiber reinforced polymer composite.

4.5.1 Carbon fiber reinforces polymer composite

Figure 4.8 shows a comparison of processed images at different times and frequencies obtained after the implementation of DAC, 1^{st} and 2^{nd} TSR derivatives, and PPT, to the PT thermal sequence. The first, second and third row of the Figure 4.8 correspond to the first, fifth and fiftieth frame of the new processed sequences.

It can be observed that the first frames of the new processed sequences show no information about the localization of the defects, except for PPT [column (d)]. Since the strongest detection mechanism in the frequency domain is at lower frequency components, PPT enables to detects the deeper defects in the first frame of the sequence (which correspond to the lowest frequency $f = 0.156\ Hz$), whilst the shallowest defects (located at $z = 0.2\ mm$) are visible from the 5^{th} frame of the PPT-phase sequence ($f = 0.785\ Hz$).

It is also important to note from the processed results showed in Figure 4.8 that DAC and TSR require more time to detect the defects − compared to PPT, which the detection occurs during the first frames of the processed sequence. This is obvious since both techniques are based on the heat conduction equation [see for instance Eq. (3.27)].

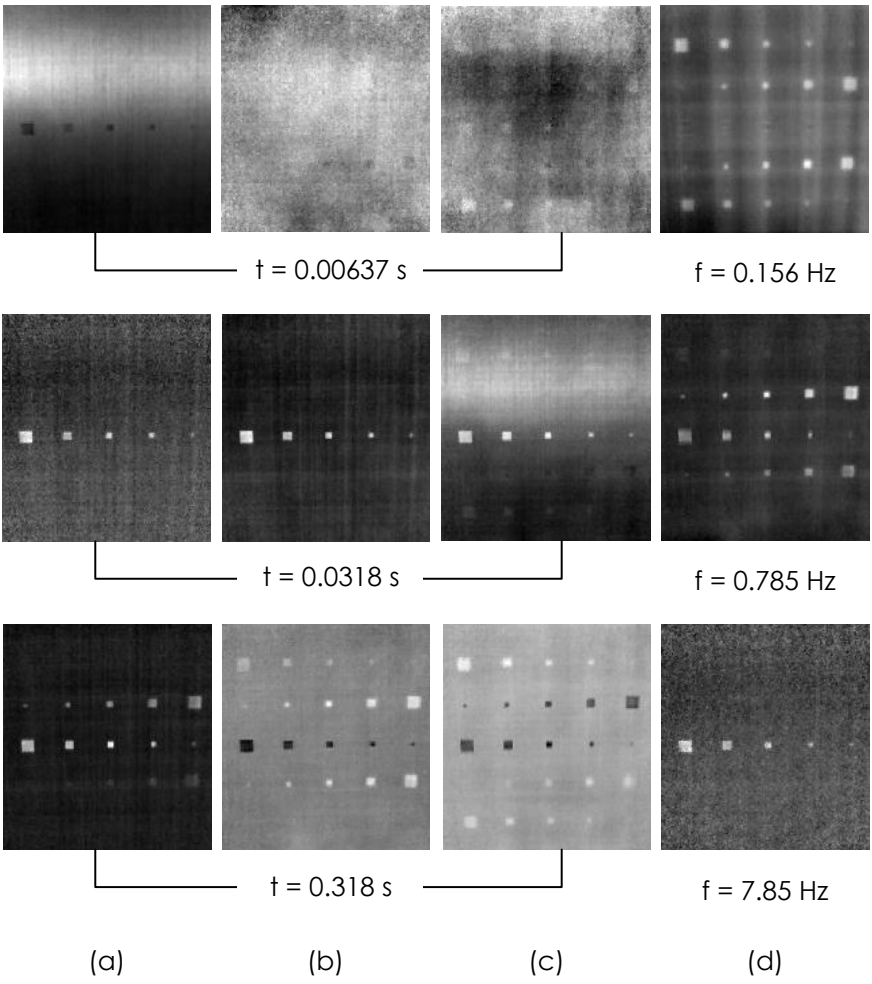

Figure 4.8: Comparison of processing results in the CFRP006 specimen: (a) DAC, (b) TSR, 1^{st} derivative, (c) TSR, 2^{nd} derivative, and (d) PPT, phase. Processing results correspond to the 1^{st}, 5^{th} and 50^{th} frame of the PT thermal sequence.

In spite of the above mentioned, DAC and TSR (1^{st} and 2^{nd} derivative images) shorten the onset time of the defects compared to raw data, allowing thus a considerable reduction of noise due to lateral heat diffusion [see Figures 4.8a, b and c].

In Figure 4.9 are showed the results of SNR_{Cmax} for raw data and after applying the signal processing techniques on the thermographic sequence obtained in the PT inspection. Furthermore, the average of the SNR at maximum signal contrast of each technique are plotted (in dashed line) in order to estimate an overall performance. This value however should be examined with caution, since it reflects the techniques performance under the experiment conditions and not a global assessment of the goodness of the techniques.

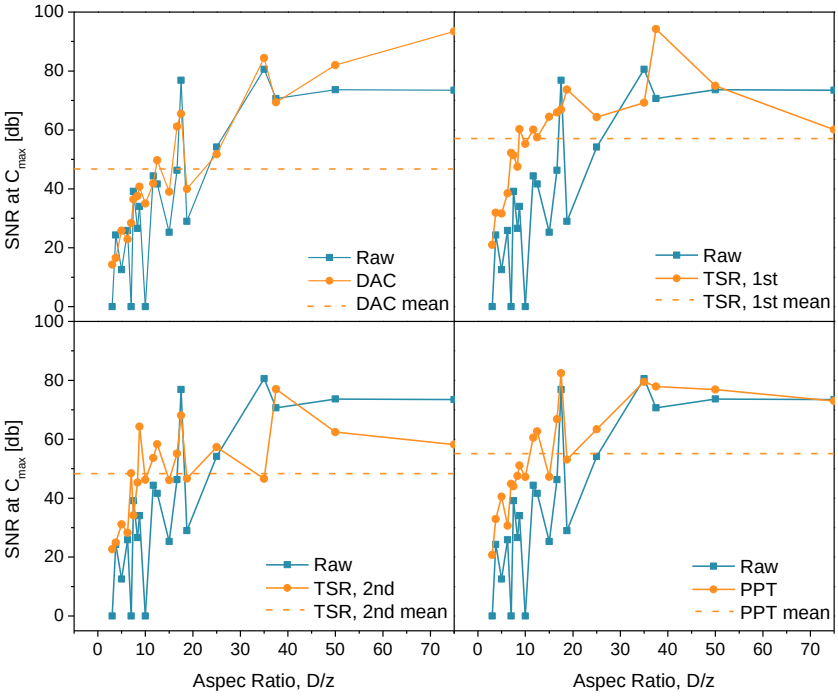

Figure 4.9: Comparison of SNR at C_{max} results for raw data and after processing the thermogram sequence obtained in the CFRP006 PT inspection.

As a first observation from these graphs, it can be concluded that no signal processing would be required for defects having an aspect ratio above 25, since the SNR obtained from raw thermograms is comparable (and sometimes higher) than the processed results. The real usefulness of processing data becomes more evident for defects having the smallest aspects ratios.

In spite that most of the defects have SNRs greater than 20 decibels (considered to be the detection threshold), an appreciable enhancement of the SNRs at maximum signal contrast were achieved with the treatment of the thermal images using each of the techniques, especially for those defects with aspect ratio below 10 (more challenging defects to be detected). For defects with aspect ratio below 25, 1^{st} and 2^{nd} derivative (TSR) and phase images (PPT) provide important improvements on the signal-to-noise ratio. DAC can provide improvement when the aspect ratio is greater than 37. As long as the aspect ratio becomes lower than 37, the performance of DAC is seriously affected. It can be also observed in the plots showed in Figure 4.9 that the SNR of defects with aspect ratio of 3, 7 and 10 in raw data is zero. This is due to the fact that, in the case of defects with $D/z = 3$ and 7, there was not enough contrast to detect them, and, in the case of the defect with $D/z = 10$, the noise level was higher than the signal amplitude.

Figure 4.10 shows the images obtained at C_{max} as function of depth and thermographic signal processing technique, considering only defects with 5 *mm* of lateral size. The main objective of these images is to validate the methodology adopted to evaluate the performance of the processing techniques. The image sequence presented in Figure 4.10 agrees with the SNR results, which determine that for the CFRP006 specimen, the best results are achieved with TSR 1^{st} derivative and PPT phase-images. Moreover, the rectangular shape of the defects is still preserved for the defects located at 0.2, 0.4 and 1.0 *mm* depth.

Conversely to TSR 1^{st} derivative and PPT, the signal strength of DAC and TSR 2^{nd} derivative is highly affected as the depth increases. Even considering the great SNRs obtained with DAC in defects with higher aspect ratios (shallower defects), results show a drastically decrease of SNRs as the values of D/z become lower. As discussed earlier, DAC is a suitable method only for shallower defects, which according to the 1D heat conduction equation is equivalent to shorter observation times.

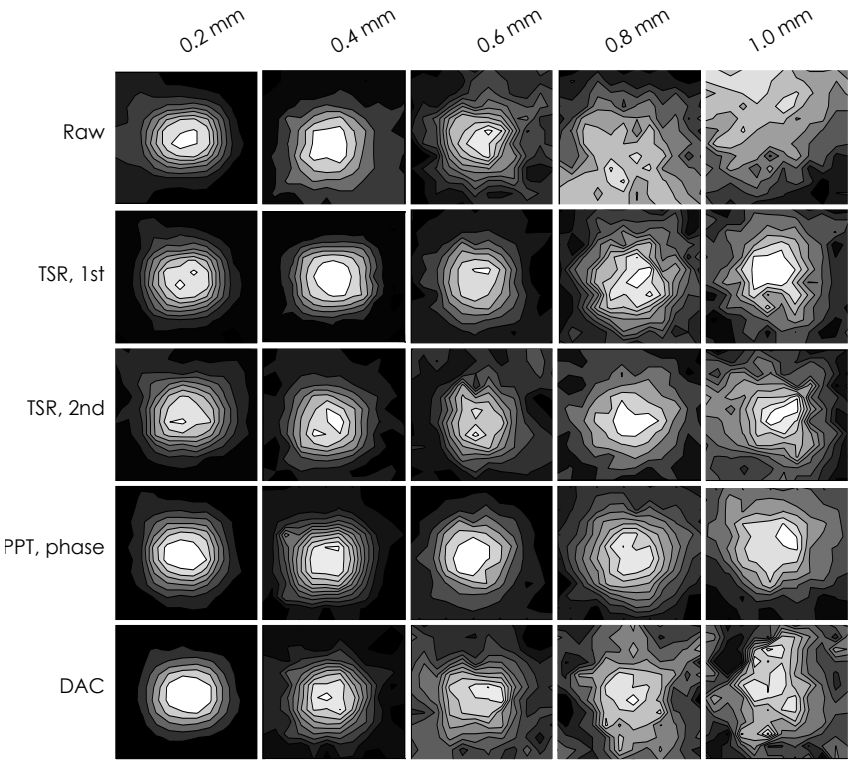

Figure 4.10: Images obtained at C_{max} as function of depths and thermographic signal processing techniques. All images correspond to the defects with 5 *mm* of lateral size of the CFRP006 specimen.

4.5.2 Glass fiber reinforces polymer composite

In Figure 4.11 is showed a set of processed images with DAC, 1^{st} and 2^{nd} TSR derivative and PPT, considering the same times and frequencies as in the CFRP006 specimen. It can be observed that in general terms the inspection of the GFRP006 presents more challenges than in the case of the carbon fiber reinforced polymer composite. The defects require more time to be detected and their signal strength (or contrast) is weak. The effects of lateral heat diffusion are stronger and the convection heat transfer plays an important role in signal degradation. As expected, the first frames of the processed sequences (first row of Figure 4.11) do not reveal the presence of the subsurface defects, except for PPT.

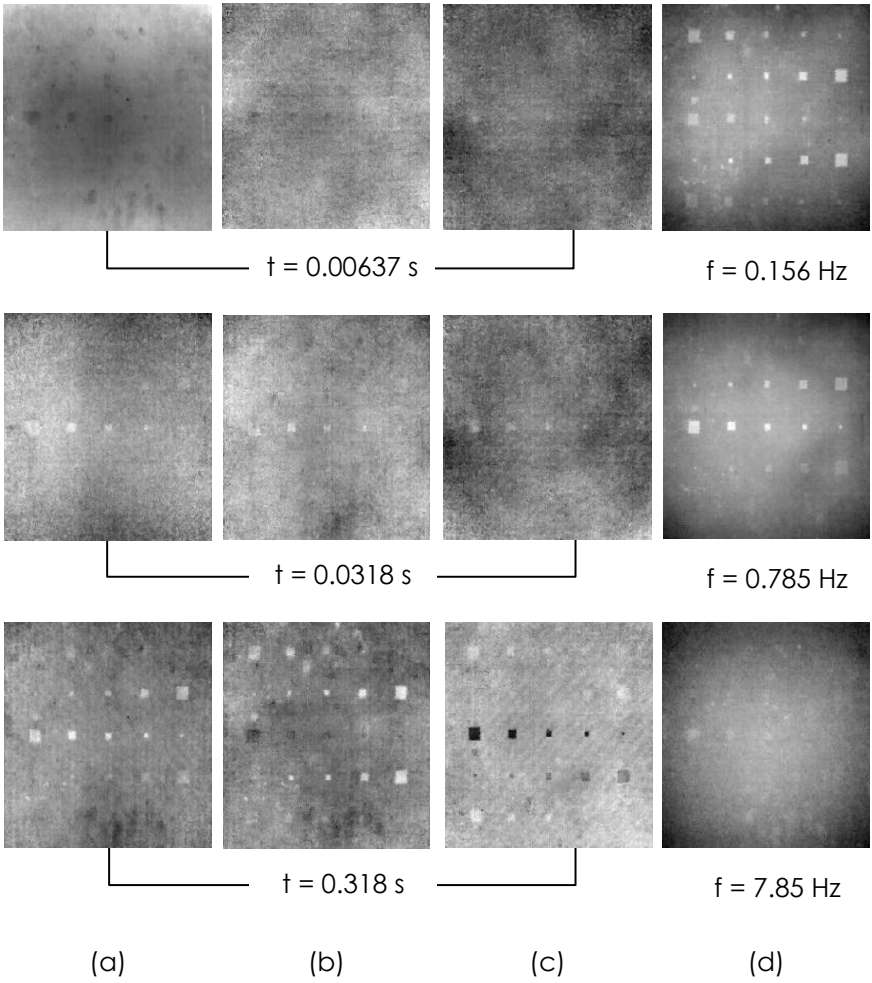

Figure 4.11: Comparison of processing results in the GFRP006 specimen: (a) DAC, (b) TSR, 1^{st} derivative, (c) TSR, 2^{nd} derivative, and (d) PPT, phase. Processing results correspond to the 1^{st}, 5^{th} and 50^{th} frame of the PT thermal sequence.

The defects located at 0.8 and 1.0 *mm* are barely detected at $t = 0.318\ s$ with TSR 1^{st} and 2^{nd} derivative images (see Figures 4.11a, b and c). Once again, DAC provides good results only in shallower defects (or larger values of D/z). It can be observed in Figure 4.11a that the defects located at $z = 0.8$ and 1.0 *mm* are not detected after the implementation of DAC.

Results of signal-to-noise ratio at maximum signal contrast are depicted in Figure 4.12. SNRs of raw data are also plotted, along with the average of the SNR results of each technique (dashed line) in order to estimate an overall performance. As in the case of the fiber carbon specimen, defects with SNR below 20 decibels are undetectable. In the other hand, defects with SNR beyond the detection threshold are considered detectable. Interestingly, seven (7) defects are below the detection threshold without processing data (in the case of the carbon fiber specimen, only four defects were below 20 decibels); this represents the great challenge in inspecting materials made up of glass fiber reinforced polymers.

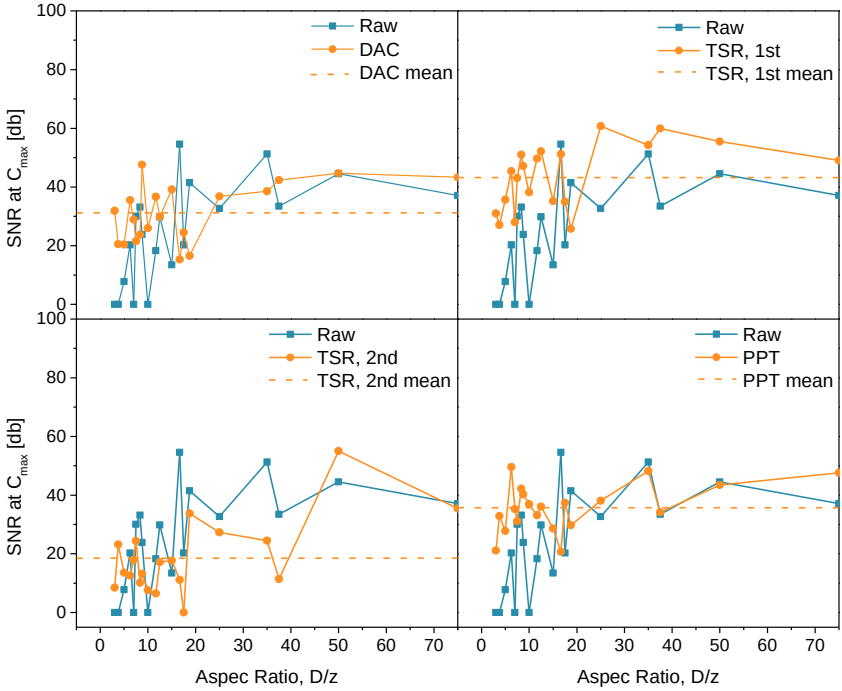

Figure 4.12: Comparison of SNR at C_{max} results for raw data and after processing the thermogram sequence obtained in the GFRP006 PT inspection.

It can also be observed from the plots showed in Figure 4.12 an appreciable improvement in the SNRs (compared to raw data) after processing the thermal sequence, even in defects with aspect ratio of 3 (more challenging defects). Those results showed that PPT phase images and TSR

1^{st} derivative images presented globally the highest values, followed by DAC. TSR 2^{nd} images showed little effectiveness in improving the quality of the signals. It should be mentioned that the acquisition parameters of the PT inspection play an important role on the effectiveness of the processing technique, and in this particular case, these were not the most appropriate parameters (more specifically, the sampling frequency) to properly implement the TSR 2^{nd}. Similar to the raw data of the CFRP006 inspection, the SNR of several defects ($D/z = 3$, 3.75, 7 and 10) is zero. A poor signal or thermal contrast associated to a high noise contamination over the sound area contributed to this behavior.

The validation of the methodology applied to study the performance of the processing techniques is showed in Figure 4.13, where a set of images at C_{max} are shown as a function of depth and processing technique, considering defects having 5 *mm* of lateral size. Figure 4.13 confirms that PPT phase and TSR 1^{st} derivative images are shown to provide the best results in terms of noise reduction (and consequently, visibility) followed by DAC.

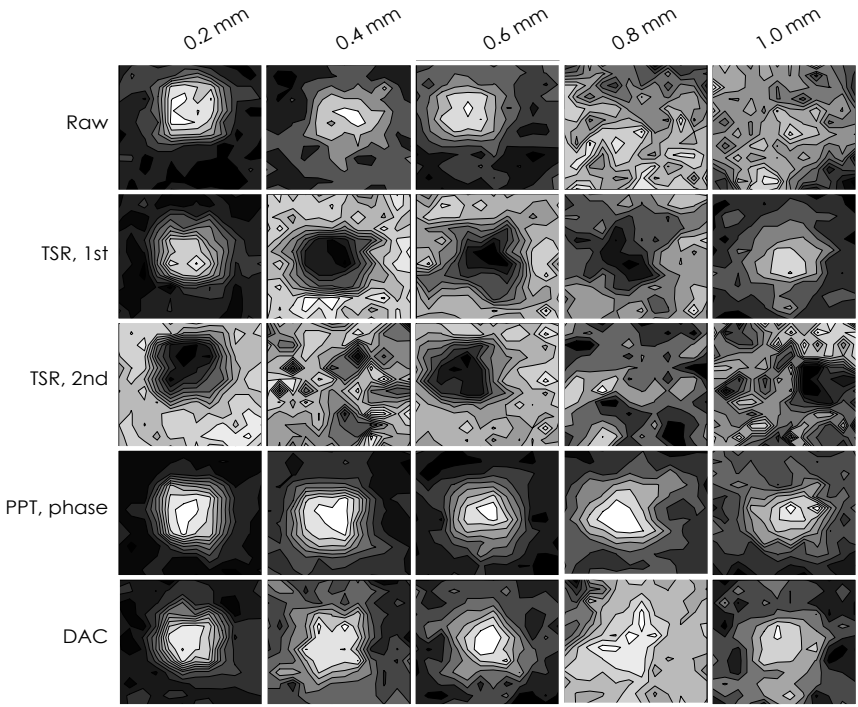

Figure 4.13: Images obtained at C_{max} as function of depths and thermographic signal processing techniques. All images correspond to the defects with 5 mm of lateral size of the GFRP006 specimen.

4.6 Summary

Thermographic signal processing is one of the major concerns in pulsed thermography. It has been widely studied that most of the difficulties that arises from the application of the thermal excitation as well as the noise caused by blurring can be solved with the application of processing algorithms to the thermographic data obtained in the PT inspection.

In this thesis are analyzed the performance of three of the most attractive methods for PT data: differential absolute contrast (DAC), thermographic signal reconstruction (TSR) and pulsed phase thermography (PPT). DAC and TSR are both derived from the solution of the 1D equation of heat conduction while PPT is based on the Discrete Fourier Transformation to translate analysis of the data from the time domain to the frequency domain.

A methodology to study the performance of the three techniques has been developed. This methodology is based on the signal-to-noise ratio (SNR) at the maximum signal contrast of each defect. To this aim, thermal data obtained from the PT inspection on two laminated composites (carbon and glass fiber reinforced composites) are processed with the techniques under discussion and the SNR of all the 25 defects are computed. The results showed that DAC is suitble only for shallower defects (and small observation times) while TSR 1^{st} derivative and PPT-phase images provide better SNR values for deeper defects. It was also shown that while TSR and DAC suffer the potential consequences of undersampling, PPT does not (since its more valuable information is at lower frequencies).

Chapter 5

Multivariate Imaging by Partial Least Squares Regression

This Chapter introduces and tests a statistical correlation method for the optimization of the pulsed thermography inspection. The method is based on partial least squares regression (PLSR), which decomposes the thermographic PT data sequence obtained during the cooling regime into a set of latent variables. Each latent variable are orthogonal to each other and are characterized by its variance; through a carefully analysis it is possible to associate them to different phenomena that take places during the cooling regime of the PT inspection. The regression method is applied on experimental PT data from carbon and glass fiber reinforced polymer specimens. The performance of the regression technique is evaluated in terms of signal-to-noise ratio at maximum signal contrasts. A comparison with the techniques previously discussed is performed in order to analyse the advantages and limitations of the new processing method of PT data.

5.1 Overview of Partial Least-Squares Regression

As already discussed, thermographic signal processing represents the front-line to overcome most of the constraints produced by non-uniform heating. Despite the great improvement in the quality of the images obtained with Fourier law-based signal processing techniques (for instance, DAC, TSR and PPT), their applications are subjected to certain criteria, which include: defect depth, thermophysical properties of the material and duration of the transient regime. These concerns motivated the review of an alternative method that could allow the reconstruction of the thermographic signatures while maintaining physical consistency. The new method proposed in this Thesis is discussed next.

5.1.1 PLS background

Partial Least Squares is a method for constructing predictive models which was developed in the 1960's by Herman Wold as an econometric technique. In spite that some of the most avid proponents of PLS are chemical engineers (including Wold's son Svante), this technique have been accepted and successfully applied to controlling industrial process (Mujica et al., 2008) - where a large process can easily have hundreds of controllable variables and dozens of outputs - analysis of hyperspectral images, magnetic resonance imaging (MRI) (Grahn et al., 1989) and most recently, neuroimaging (Krishnan et al., 2011). The author recommend references Martens (2001) and Wold (2001) where is presented a chronological overview of the evolution of PLS since its emerging from Herman Wold's work.

The basic concept of PLS and its difference with classical linear regression methods is depicted in Figure 5.1. While most regression methods rely on the use of all x-values independently of its content in order to form a new linear combination of variables, PLS finds a few linear combinations (components or factors) of the original x-values and uses only these linear combination in the regression equation (Naes et al., 1996; Wold et al., 1984). In this way, irrelevant and unstable information is discarded and only the most relevant part of the x-variation is used for regression. The collinearity problem is solved and more stable regression equations are obtained. Furthermore, since all variables all projected down to only a few linear combinations, simple plotting techniques can be used for analysis.

As a regression method, PLSR seeks to model a dependent variable Y (predicted) in terms of an independent variable X (predictor). To this aim, PLS combines interesting features of two techniques: principal component regression (PCR) and multivariate linear regression (MLR). While in PCR factors that capture the greatest amount of variance in the predictor (X) variables are found, in MLR the aim is to find a single factor that best correlates predictor (X) with predicted (Y) variables. In PLS, the factors, or new variables, are chosen to simultaneously satisfy three conditions: i) that they are highly correlated with the dependent (or Y) variables, as in MLR; ii) that they model as much of the variance among the independent (or X) variables as possible, as in PCR; and iii) that they are uncorrelated with each other. The first condition is clearly necessary in order for a good regression to be obtained. It is this first condition that distinguishes PLS from PCR. The second condition is based on the premise that the

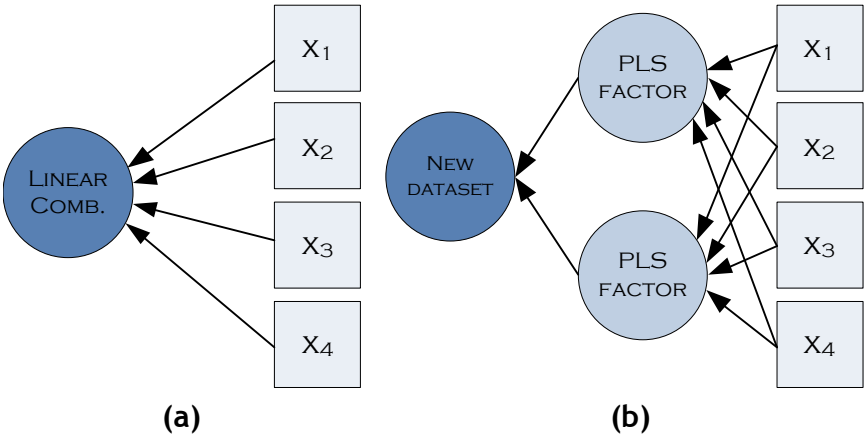

Figure 5.1: Conceptual illustration of PLS and its comparison with classical linear regression methods. In classical linear regression all variables are selected to form a linear combination as in (a), while in PLS all x-variables are transformed into linear combinations of PLS factors in order to form a new dataset as in (b).

signal-to-noise ratio is highest for the components with the greatest variance. The third condition minimizes the redundancy of information and hence minimizes the number of variables needed (Glen et al., 1989). In the next section the mathematical formulation upon which PLSR is based is described.

5.1.2 Mathematical formulation of PLSR

PLS regression is based on the basic latent component decomposition of the predictor $X(n\ x\ N)$ and predicted $Y(n\ x\ M)$ matrices into a combination of loadings, scores and residuals. Mathematically, the PLS model is expressed as:

$$X = TP^T + E \tag{5.1a}$$

$$Y = UQ^T + F \tag{5.1b}$$

In Equations (5.1), $T(n\ x\ a)$ is known as the scores matrix and its elements are denoted by t_a ($a = 1,2,...,A$). The scores can be considered as a small set of underlying or latent variables responsible for the systematic variations in X. The matrices $P(N\ x\ a)$ and $Q(M\ x\ a)$ are called loadings

(or coefficients) matrices and they describe how the variables in T relate to the original data matrices X and Y (Naes et al., 1996). Finally, the matrices $E(n\ x\ N)$ and $F(n\ x\ M)$ are called residuals matrices and they represent the noise or irrelevant variability in X and Y, respectively.

As it will be further discussed, the X-scores (T) are predictors of Y and also model X, i.e., both Y and X are assumed to be, at least partly, modeled by the same latent variables. The scores are orthogonal and are estimated as linear combinations of the original variables x_k with the coefficients, called weights, w_{ka} ($a = 1,2,...,A$). Thus, the scores matrix T is expressed by:

$$T = XW \tag{5.2}$$

Once the scores matrix T is obtained, the loadings matrices P and Q are estimated through the regression of X and Y onto T. Next, the residual matrices are found by subtracting the estimated versions of TP^T and UQ^T from X and Y, respectively. Finally, the regression coefficients for the model are obtained.

It is important to note that in PLS the weight column vectors are orthogonal to each other, while the loadings vectors (**P** and **Q**) and Y-scores are not. The columns of the PLS scores matrix T are also orthogonal to each other (Sjostrom and Eriksson, 2001). This PLS method in its classical form is based on the nonlinear iterative partial least squares (NIPALS) algorithm. However, there are alternative methods of obtaining the parameters of Equations (5.1) by using other forms of PLS (see Rosipal and Kramer, 2005).

Next, the NIPALS algorithm is discussed.

5.1.3 The NIPALS algorithm

NIPALS algorithm carries out the decomposition of both, X and Y, through the computation of scores, weights, loadings and inner-coefficients sequentially. For univariate Y ($Y = y$), the bilinear decomposition is given by:

$$X = t_1 p_1' + t_2 p_2' + ... + t_k p_k' + F \tag{5.3a}$$
$$y = u_1 q_1' + u_2 q_2' + ... + u_k q_k' + E \tag{5.3b}$$

The algorithm calculates each of the variables as follows (Eigenvector, 2006):

- Imput: $(X_o \longleftarrow X; Y_o \longleftarrow Y)$
- Step 1. $u_1 = y$
- Step 2. $w_1 = \dfrac{X^T u_1}{\| X^T u_1 \|}$
- Step 3. $t_1 = X w_1$
- Step 4. $q_1 = \dfrac{Y^T t_1}{\| Y^T t_1 \|}$
- Step 5. $u_1 = Y q_1$
- Convergence is then checked by comparing t_1 in (3) with the value from the previous iteration.
- Step 6. $p_1 = \dfrac{X^T t_1}{\| t_1^T t_1 \|}$
- Step 7. $p_{1new} = \dfrac{X^T t_1}{\| t^T t_1 \|}$
- Step 8. $t_{1new} = t_{1old} \| p_{1old} \|$
- Step 9. $w_{1new} = w_{1old} \| p_{1old} \|$
- Find the regression coefficient for the inner relation.
- Step 10. $b_1 = \frac{u_1^T}{\|t_1^T t_1\|}$
- After calculating the scores and loadings of the first latent variable, X and y-blocks residuals are calculated.
- Step 11. $E_1 = X - t_1 p_1^T$
- Step 12. $F_1 = y - b_1 t_1 q_1^T$
- Step 13. Repeat the entire procedure replacing X and y with their residuals.

The application of the PLSR as a reconstruction method of PT data is discussed next.

5.2 Application of PLSR to PT Inspection

The application of partial least squares regression to the pulsed thermography data arises from the necessity of 'reconstruct' the thermal data obtained during the inspection into a new sequence of images less contaminated by noise while maintaining physical coherency. With PLSR it is possible to link time and temperature data, in a similar manner as TSR (or the linking of frequency and phase-lag in PPT), allowing the extraction of the most important variations while discarding the unnecessary information present in the original thermal sequence. This application is achieved by decomposing the raw thermal data into multiple PLS components (or latent variables), each component being orthogonal to each other. Since each of the PLS components is characterized by its variance, it is possible to identify through a carefully analysis of the LVs different phenomena affecting the overall thermal regime. In the next sections, the methodology applied in this work to reconstruct a new thermal sequence using PLSR is discussed in detail.

5.2.1 Data structure and modeling

The thermal images obtained during the PT inspection are typically arranged in a 3D matrix, whose $x-$ and $y-$axis are represented, respectively, by i and j pixels, while the $z-$axis corresponds to the k frame number. N_x and N_y correspond to the total numbers of pixels in the $x-$ and $y-$ directions while N_T is the total number of frames (see Figure 5.2 on the left).

In order to perform the decomposition of the thermal data sequence into PLS components, it is firstly necessary to transform the 3D thermal data into a 2D raster-like matrix, as shown in Figure 5.2. This process is known as unfolding. The unfolded X matrix (corresponding to the thermal sequence) has dimensions $N_T \; x \; N_x \cdot N_y$ and physically represents N_T observations (or samples) of $N_x \cdot N_y$ variables (or measurements). On the other hand, the dimension of the predicted matrix Y (defined by the observation time during which the thermal images were captured) is $N_T \; x \; 1$.

Prior to the PLS decomposition, in order to allow an easy interpretation and numerical stability, it is recommended that the values for each variable are in the mean-centered form. Centering is performed to make the data compatible with the structural model. The temperature average for each row (or frame) is calculated and then subtracted from each corresponding variable.

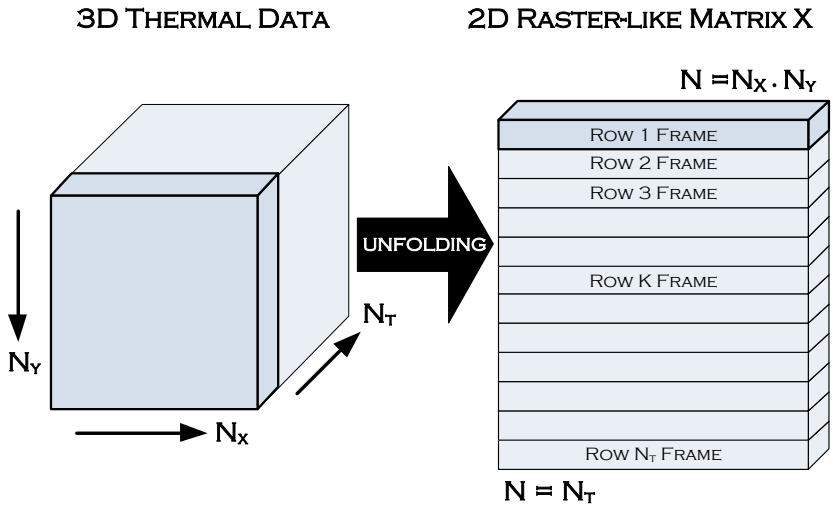

Figure 5.2: Schematic representation of the transformation of the 3D thermal data into a 2D raster-like matrix.

The experimental PT data used as X and Y inputs in the PLS model, consists of two sets of thermal images obtained from the PT inspection of specimens CFRP006 and GFRP006. The 3D sequence (269 x 252 x 500) is mean-centered and converted into a 2D raster-like matrix X (both with dimension 500 x 67788). The predicted Y matrix is a column-vector (500 x 1) composed of a time series. The application of PLSR, using Equations (5.1), to each of the pulsed thermography sequences is represented graphically in Figure 5.3.

Matrix X and the column-vector Y are decomposed into a set of scores, loadings and errors matrices. The X and Y scores matrices both have dimensions N_T x a, being a the number of PLS components of the regression model; similarly, the dimensions of the X and Y loadings matrices are also dependent on the number of PLS components. The residuals matrices E and F represent the error between the original data X and Y, and the fitted data obtained through the multiplication of the scores and loadings matrices.

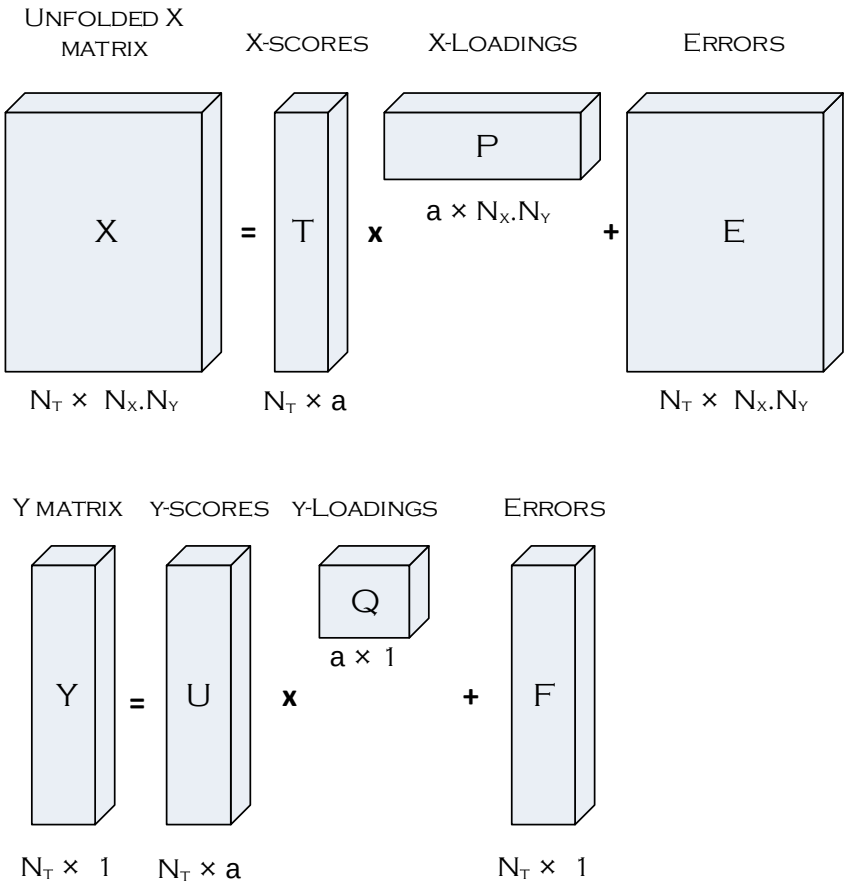

Figure 5.3: Graphical representation of the application of Equations (5.1) to the pulsed thermography thermal sequence.

5.2.2 Model dimensionality

The model dimensionality refers to the number of PLS components used to construct the new empirical model. Although it is possible to calculate as many PLS components as the rank of the X block matrix, in general, not all of them are used. The main reason for this is that the measured data is never noise-free and some of the smaller components only describe noise. For this reason it is necessary to select the number of PLS components based on an appropriate criteria in order to avoid over-fitting

and also leave out small components that carry problems of collinearity.

One of the quantitative variables most commonly used to select the numbers of components is the RMSE (root mean square error), which is expressed by:

$$RMSE = \sqrt{\frac{\sum_{i=1}^{n} (x_i - x_{i,ref})^2}{n}} \tag{5.4}$$

where n is the number of samples, $x_{i,ref}$ is the reference value and x_i is the predicted value. From Eq. (5.4) it is possible to estimate the number of components that best fits the X data. Lower RMSE values do not necessarily mean that the selected number of components was the most appropriate for the regression model. In some cases, the RMSE tends to decrease as the number of components is increased. However, as mentioned earlier, increasing smaller components will introduce noise oscillations into the regressed data. The use of Eq. (5.4) to predict the number of latent variables should be carried out in conjunction with the analysis of the percentage of variance explained by each component.

Figure 5.4 shows the estimated RMSE and the percentage variance explained in X of the thermal PT data obtained from the inspection on the CFRP006 and GFRP006 specimens (Figures 5.4a and b respectively). Although the minimum RMSE in both cases is reached with 10 components, only 6 components are sufficient to describe all of the variance in the predictor matrix X. Increasing to more than 6 PLS components will introduce higher-order oscillations into the new data sequence. Further analysis and discussions are based on PLS models using 6 components.

5.2.3 Descriptive analysis of PLS latent variables

Previous studies [see for instance Rajic (2002) and Marinetti et al. (2004)] on the application of multivariate statistical regression to IR thermal sequences have shown that through an analysis of the factors of the multivariate model it is possible to extract useful information that can be used for the optimization of the PT inspection. Thus, the predictor loading matrix P (see Figure 5.3) was converted into a 3D matrix, composed of N_x x N_y x N_{comp} elements (N_x and N_y are the total numbers of pixels in the $x-$ and $y-$directions, respectively, whereas N_{comp} is the number of components of the PLS regression model). The six predictor loadings of the PT data in the CFRP006 specimen are shown in Figure 5.5.

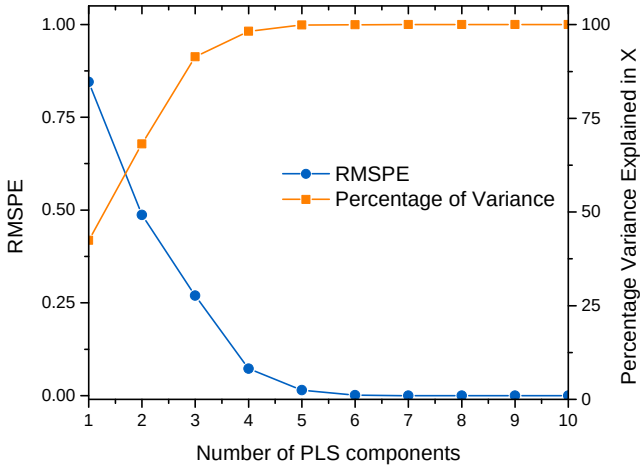

(a)

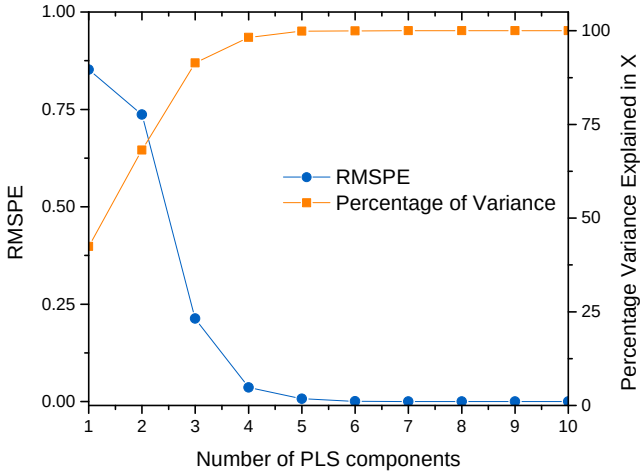

(b)

Figure 5.4: Estimated MSPE and percent variance explained in X for thermal PT data obtained in: (a) CFRP006 and (b) GFRP006 specimens.

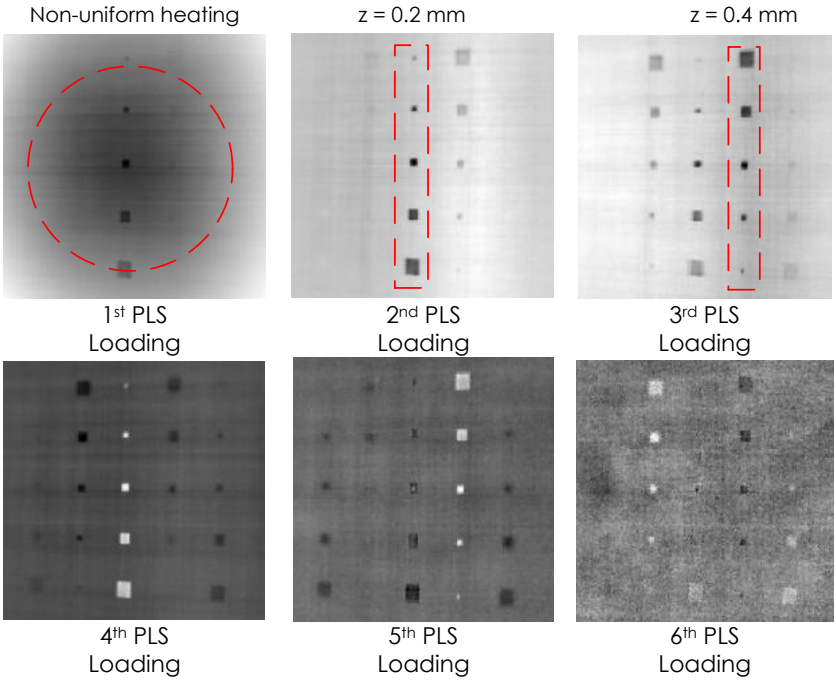

Figure 5.5: PLS loadings obtained after the implementation of PLSR to the experimental pulsed thermography data on the CFRP006 specimen.

It can be noted from Figure 5.5 that the 1^{st} PLS loading conserves a Gaussian-shape distribution, with higher values for the coefficients at the center of the images. This behavior indicates that the effect of non-uniform heating is retained in the 1^{st} PLS component. The 2^{nd} PLS loading shows that defects located at 0.2 *mm* can be clearly detected; similarly, most of the defects with $z = 0.4$ *mm* can be detected in the same loading but with less contrast. Deeper defects can be observed in the 3^{rd}, 4^{th} and 5^{th} PLS loadings, which is due to the fact that the variation in the temperature during the cooling process becomes lower as the depth increases (in agreement with heat conduction theory). As depicted in Figure 5.6, each PLS component is characterized by its variance. Thus, the 1^{st} PLS component retains the highest variations, followed by the 2^{nd} component and so on. Along with the histograms of each loadings, the standard deviation of a fitted Gaussian distribution function has been included.

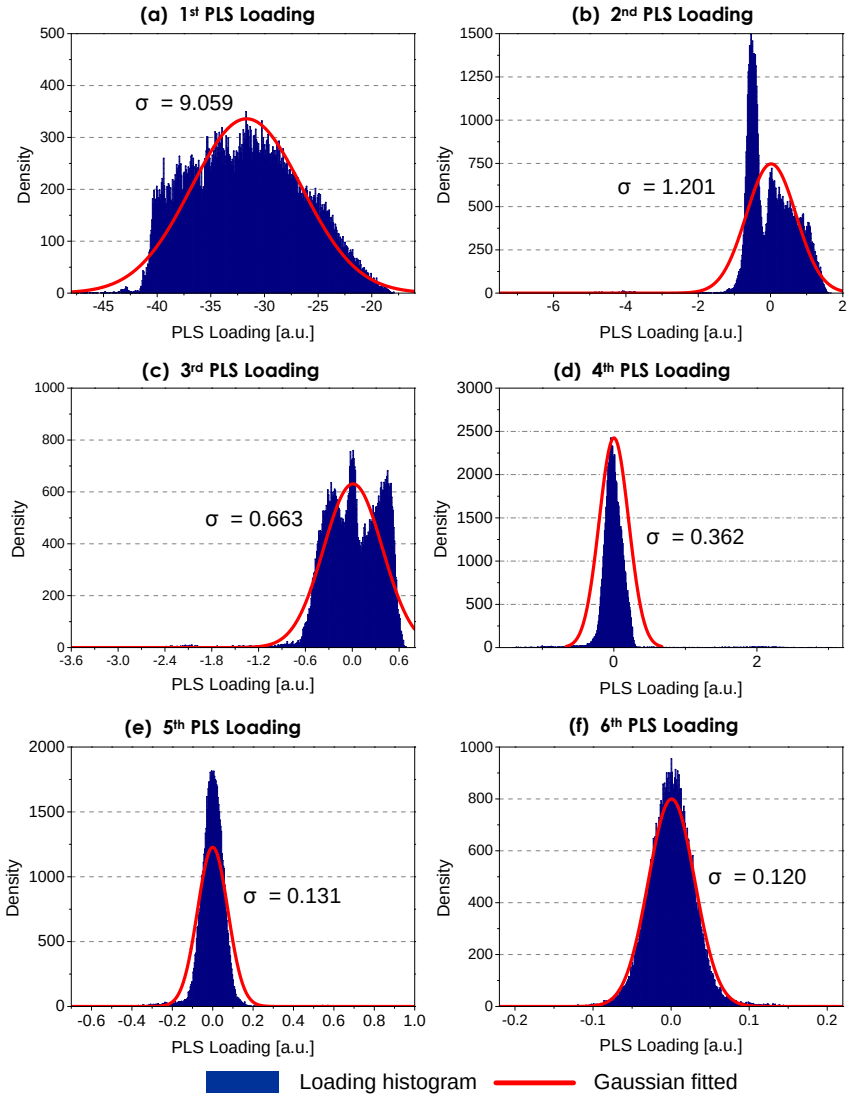

Figure 5.6: Histograms and fitted Gaussian distribution function to the PLS loadings obtained after application of PLSR to the PT data of the CFRP006 specimen.

As expected, the highest standard deviation corresponds to the 1^{st} PLS loading (see Figure 5.6a), which confirms that most of the variation is due to the non-uniform heating applied during the thermal excitation. The standard deviation drops dramatically from the 1^{st} to the 2^{nd} PLS loading (from 9.059 to 1.201). Furthermore, it is important to note that deeper defects are related to loadings with lower standard variation (3^{rd}, 4^{th} and 6^{th}), which is a consequence of the thermal phenomena that take place during the cooling process: as the defect depth increases the variation in the temperature compared to a reference sound area becomes lower. Consequently, the lowest variations in the temperature are retained in the last PLS components, as shown in Figures 5.5 and 5.6. Finally, it can also be observed in these figures that the 6^{th} PLS loading is highly contaminated by noise, characterized by a low variance (see for instance Figure 5.6d).

A more detailed analysis of the PLS latent variables can be carried out when looking at each score T and its corresponding loading, P, of the predictor matrix X. The outer product of the score and the corresponding loading vectors allow to analyze the variation of each latent variable over time. Graphically, this operation is illustrated in Figure 5.7. The result is given by a set of the N_{comp} matrix, which after unfolding has dimensions $N_x \; x \; N_y \; x \; N_T$.

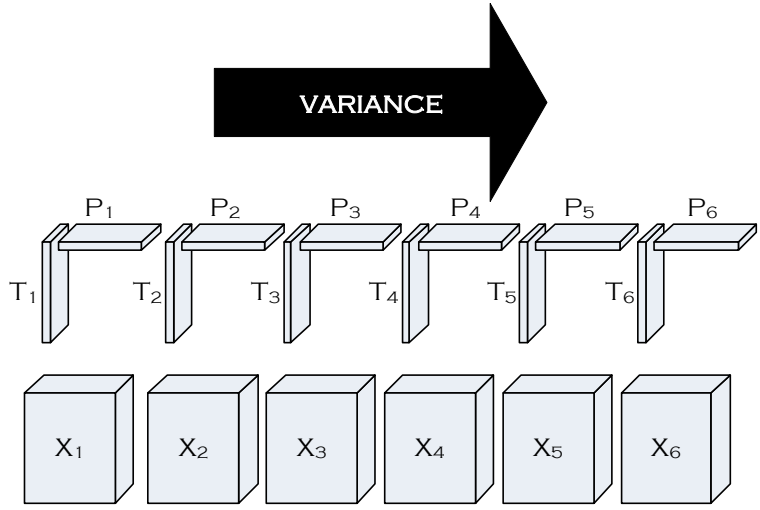

Figure 5.7: Outer product of scores T and the corresponding loadings vector P of the predictor matrix X.

Physically, each matrix describes the systematic variation of each latent variable over time. Thus, it is possible to determine the moment at which each physical effect - described by its variance - is more predominant during the cooling process of the pulsed thermography inspection. Figure 5.8 shows the evolution of the 1^{st}, 2^{nd}, 3^{rd} and 6^{th} PLS latent variables over time, considering defects with aspect ratios $D/z = 10/0.2$, 10/0.4 and 10/0.6. The evolution of a reference sound area has been included in order to compare its behaviour with defective areas.

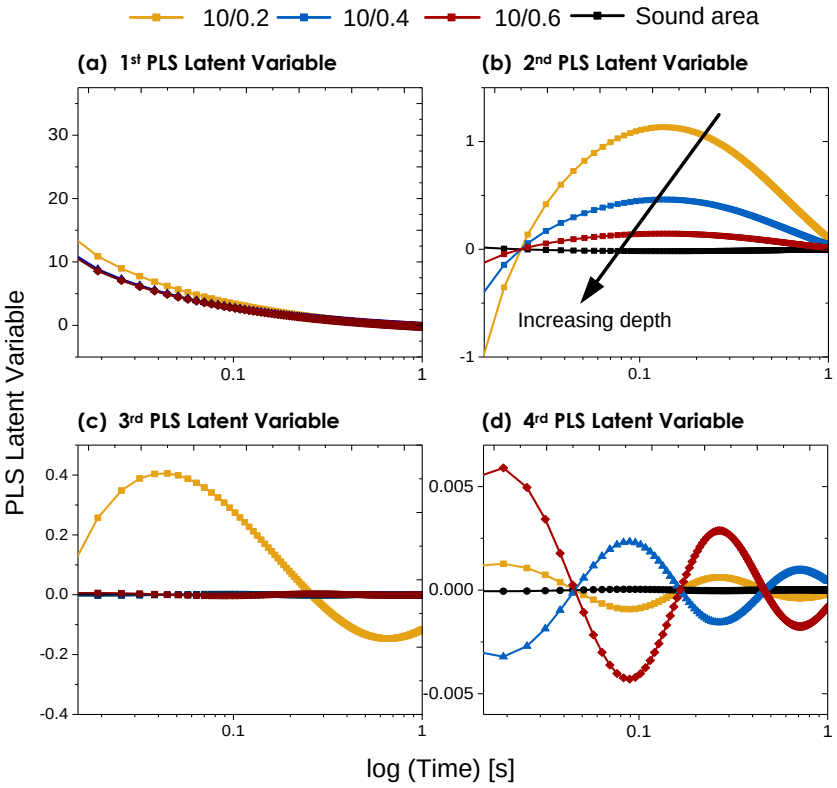

Figure 5.8: Evolution of (a) 1^{st}, (b) 2^{nd}, (c) 3^{rd} and (d) 6^{th} PLS latent variables over time.

It can be observed from Figure 5.8a that all three defects present the same behavior in the 1^{st} PLS latent variable. In other words, the variability of the temperature of the defects is almost the same. Furthermore, the

strongest variation occurs at the beginning of the cooling process, when the effects of the non-uniform heating are more predominant. However, there is no evidence that the 1^{st} PLS component retains information concerning to the thermal diffusion process or the location of the defects.

In contrast to the 1^{st} component, where all three defects present the same behavior, the 2^{nd} PLS latent variable shows a strong correlation between the variability of temperature (maximum value for the latent variable) and defect depth (see Figure 5.8b). The deeper the defects the lower the maximum value of the PLS latent variable will be. This behavior is in agreement with the results reported by Rajic (2002) using principal component thermography, in the sense that the 2^{nd} component (or factor in PCT) is associated with the thermal diffusion that arises from the application of the pulsed thermal excitation. Moreover, it can be noted in Figure 5.8c that an oscillatory behaviour begins to rise in the 3^{rd} component (along with the 4^{th} and 5^{th}) dominated by non-linearities, whereas the 6^{th} (Figure 5.8d) is related to higher-order oscillations or random noise.

5.2.4 Loadings and scores plots

Loadings and scores plots can provide valuable information concerning to the experiment and the behaviour of the different phenomena affecting the inspection process. For this reason, this section extents the analysis of the PLSR to the loadings and scores plots in order to obtain insight of the relationship between samples, variables and PLS components.

Figure 5.9 shows the loadings (a) and scores (b) plots of the CFRP006 thermal data regressed with PLSR. The relationship between variables (or temperature measurements) is described in the loadings plot. Variables that are close together are said to be correlated. As is shown in Figure 5.9a, most of the variables are correlated to each other. However, there are some data points which are uncorrelated (those far away from the main group); they may form small groups called clusters. Two cluster (in color ellipses) has been identified in the thermal image and interestingly, they correspond to defective areas with $z = 0.2$ *mm* and where the irradiation intensity was highest.

The relation between samples (sample refers to each time at which the IR camera made the acquisition) can be examined in the scores plot showed in Figure 5.9b. The first sample loads most in both - the first and second PLS component - followed by the second sample (or frame). Since both samples are far away from the rest, they are said to be uncorrelated.

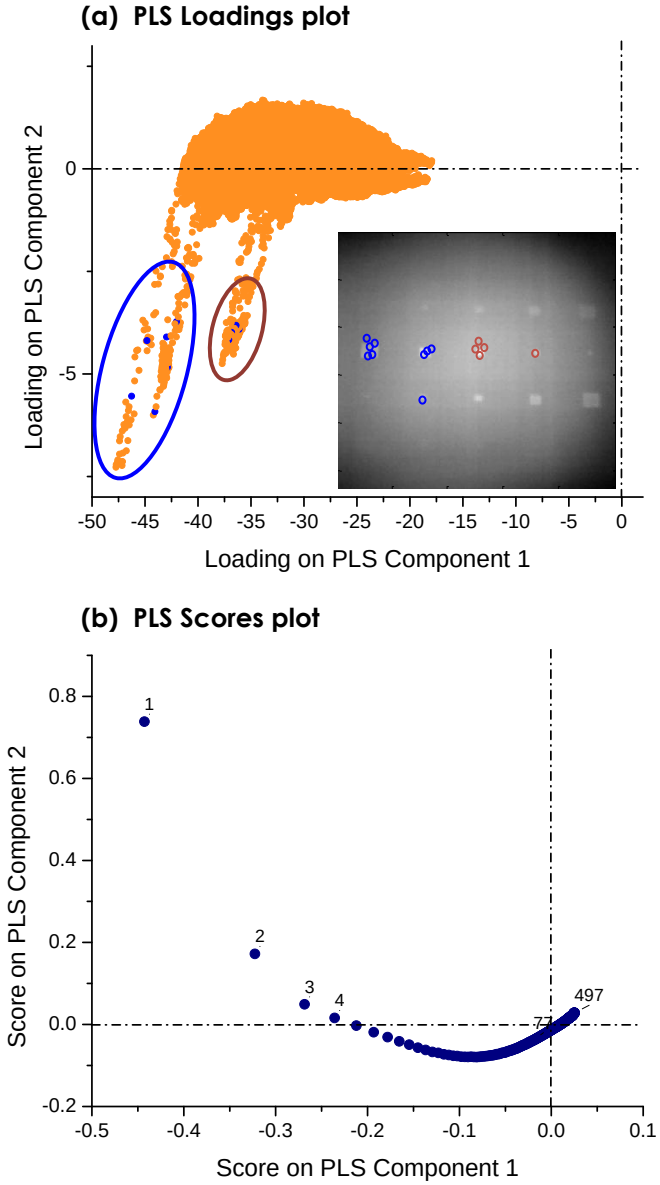

Figure 5.9: Loadings (a) and scores (b) plots in the CFRO006 thermal data.

The analysis of the loadings and scores plots suggest that there are some variables (temperature measurements) and samples (frames) that should be left out from the empirical model. Since those outliers are not correlated to the rest of the data, quantitative analysis may be affected by the use of them. Furthermore, the scores plot suggests that the moments at which the thermal effects are stronger (2^{dn} PLS component) correspond from 0.0254 to 0.490 *s* (see Figure 5.9b). Samples further to 0.490 *s* (or frame 77) are not important to the model under study.

Based on the analysis presented herein, the next section is dedicated to the optimization of the pulsed thermography inspection using partial least squares regression as a signal processing method.

5.3 Experimental Optimization of PT Inspection

5.3.1 Enhanced Detection by PLSR

Once the thermal sequence has been decomposed into a set of latent variables, each one characterized by its variability, it is possible to create a new set of thermal images which are less contaminated by noise and with less redundant signals. Figure 5.10 shows a set of six images corresponding to different times after the application of PLSR to the PT thermal sequence of the CFRP006 specimen. It can be shown that almost 92 % of the defects can be detected with the new synthetic sequence. Although at longer times (i.e., at 1.16 and 1.75 *s*) the background noise is reduced; non-uniform heating is still present at the beginning of the IR sequence. The most important finding is that the new sequence preserves the physical coherency of the heat transfer process: shallower defects can be observed at the beginning of the cooling process while deeper defects require a longer observation time to be detected and show less thermal contrast. This latter factor is extremely important and useful for the quantitative analysis of defects.

Based on the analysis of the PLS latent variables (see section 5.2.3), the 1^{st} PLS component, which retains the highest variance produced by non-uniform heating, is suppressed from the synthetic data. In other words, non-uniform heating effects are discarded from the original thermal data. The results of this operation are shown in Figure 5.11. In order to compare and analyze the effects of this operation, the same times as those reported in Figure 5.10 are considered.

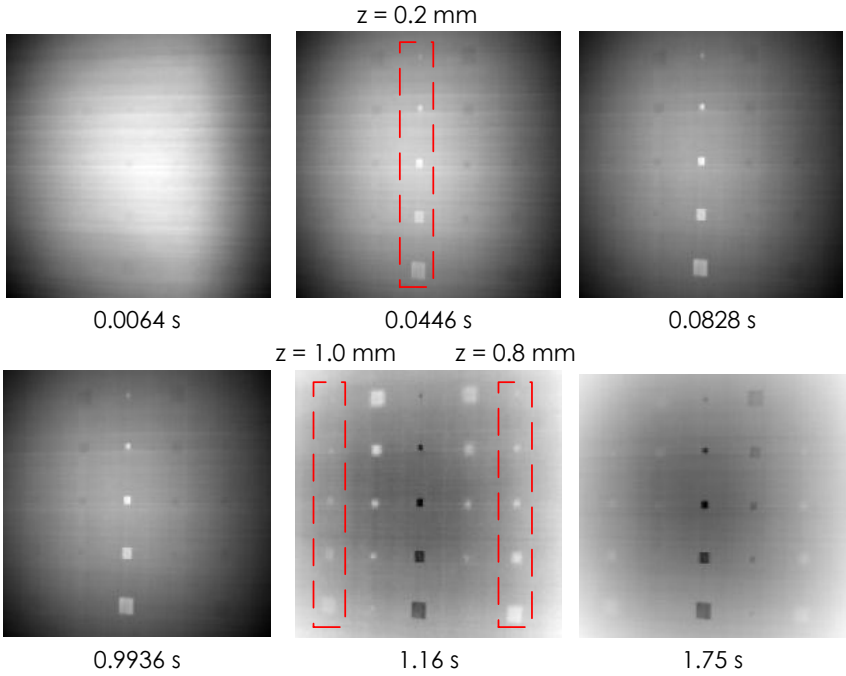

Figure 5.10: Synthetic thermal sequence obtained after the application of the PLS model to raw temperature images of the CFRP006 specimen.

It can be noted from Figure 5.11 that after the suppression of the 1^{st} PLS component for the synthetic data, a considerable enhancement in the visibility of the defects is achieved. From the first frame of the thermal sequence (at 0.0064s) the defects located at 0.2 *mm* are already visible in the enhanced thermal sequence. At 0.0446 seconds (second frame), defects located at 0.4 and 0.6 *mm* depth are visible, even those with the smallest lateral size ($D = 3mm$). Moreover, it is important to note that the Gaussian distribution of temperature produced by the non-uniform excitation was eliminated from the new sequence, allowing defects located close to the edges of the specimen to be easily detected. At 0.9936 *s* almost 96 % of the defects are clearly visible, which represents a significant improvement in the ability of PLSR to detect defects at earlier times when compared with 32 % of detection when the non-uniform effect is present in the data sequence.

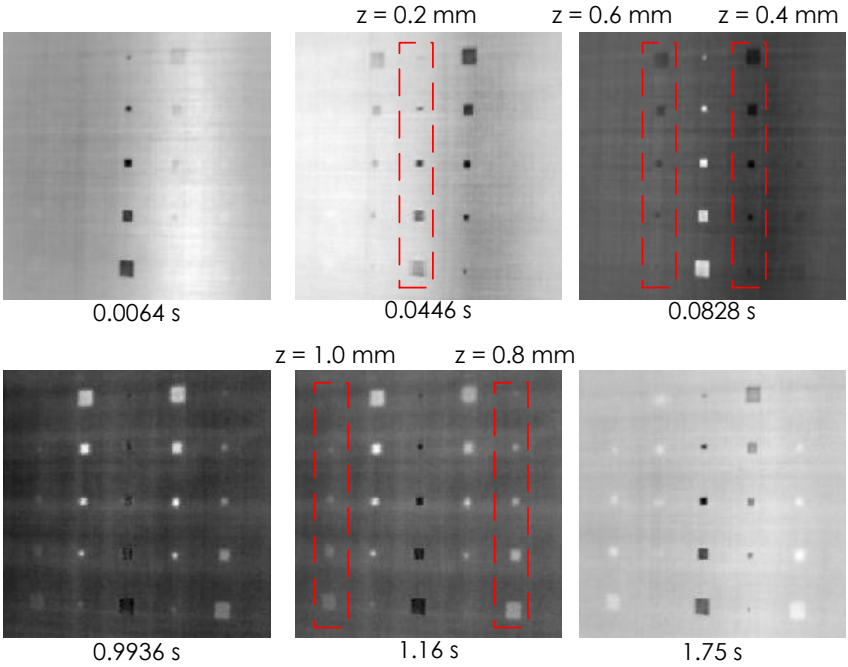

Figure 5.11: Enhanced thermal sequence after suppression of the non-uniform heating effects in the PT data of the CFRP006 specimen.

The same operation performed in the CFRP006 thermal data has been carried out to the obtained in the PT inspection of the GFRP006 specimen. A PLS model with 6 components was built and the 1^{st} PLS component was suppressed from the synthetic data. The result of this operation is depicted Figure 5.12. With the enhanced thermal sequence is possible to detect up to 56 % of the defects (an increase of 8 % compared to raw data). Defects located at $z = 0.2$, 0.4 and 0.6 *mm* are clearly visible 0.9936 *s* and at 1.75 *s* most of the defects located at $z = 0.8$ *mm* can be detected.

The suppression of non-uniform heating provided a considerable reduction of background noise specially in the CFRP006 thermal data. However, even with the reduction of spatial noise obtained in the enhanced sequence of the GFRP006 specimen, the signal strength (or contrast) of the defects is still affected by the lateral heat diffusion, this as product of the longer times of observation.

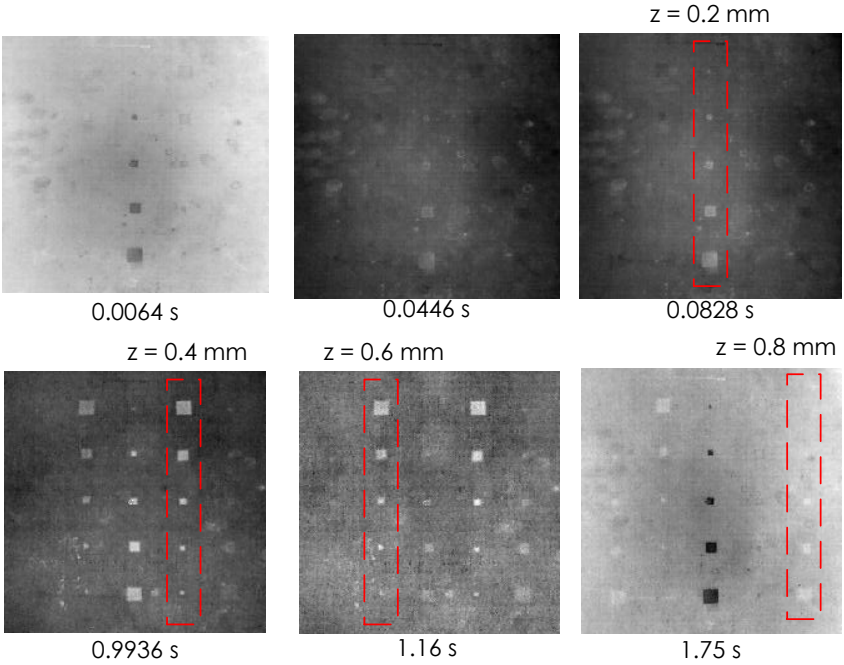

Figure 5.12: Enhanced thermal sequence after suppression of the non-uniform heating effects in the PT data of the GFRP006 specimen.

A more detailed analysis of the signal-to-noise ratio is discussed next.

5.3.2 Signal-to-noise ratio analysis

The performance of the method proposed in this Chapter is evaluated in terms of the signal-to-noise ratio (SNR) at maximum signal contrast. The same methodology discussed in Chapter 4 is used in this section. Three different sequences are analyzed on both specimens (CFRP006 and GFRP006): the raw thermal sequences obtained during the PT inspections; the synthetic data sequences processed with PLSR; and a data sequence processed with the 1^{st} PLS component suppressed.

Figure 5.13 shows the results for the SNR at maximum signal contrast of the carbon (a) and glass (b) fibers specimens, both computed for unprocessed PT thermal data (raw), the thermal sequence processed using PLSR with 6 components (PLS, 6 components) and the processed

enhanced sequence obtained after the suppression of the 1^{st} PLS component (PLS, non-uniform heating suppressed). As in previous analysis, the SNR results are based on the aspect ratio, D/z, of the defects. For the CFRP006 specimen (Figure 5.13a), it can be noted that a considerable improvement in the SNR values is obtained after processing the PT raw data with partial least squares regression. With the PLSR an increase in the SNR was obtained for 88 % (22/25) of the defects. Only defects with $D/z = 15/0.2$, $7/0.2$ and $3/0.8$ exhibit SNR values below that obtained with the raw data. Since the defects with 0.2 *mm* depth are located in the middle of the specimen (where more thermal energy is concentrated during the thermal excitation), a decrease in their SNR values was expected due to a reduction in the signal strength. However, their values continue to be above the detection threshold, considered to be of 20 *db*.

The performance of the SNR results improves even more when the suppression of the 1^{st} PLS component is applied; an increase in the SNR values for 96 % of the defects is achieved when non-uniform heating is removed from the synthetic PT sequence. Even the defects with the lowest aspect ratio (for instance $D/z = 3/1$ and 3/5) exhibit an increase in their SNR values. The increase in the SNR values when the suppression of the 1^{st} PLS component is performed (where the effects of non-uniform heating are retained) is associated with a reduction in the background noise in the new thermal sequence. Moreover, the shortening of the onset time (time at which the defects are first detectable in the thermal sequence) plays an important role in the increase in the signal strength; as already discussed, the effects of lateral heat diffusion (a phenomenon known as blurring) are more predominant at later times.

Concerning to the GFRP006 specimen, results showed that after processing the PT raw data with PLSR an increase in the SNR for 56 % (14/25) of the defects was achieved. Moreover, when the 1^{st} PLS component is suppressed from the synthetic PT sequence, an increase in the SNR was obtained for 64 % (16/25) of the defects. In spite of the SNR improvement exhibited in 64 % (16/25) of the defects, the most challenging defects ($D/z = 3/1$, $5/1$ and $7/1$) continue to be undetectable. As discussed in section 5.3.1, the themophysical properties of the glass fiber played a key role in the thermal process of the PT inspection, increasing the effects of signal degradation due to blurring.

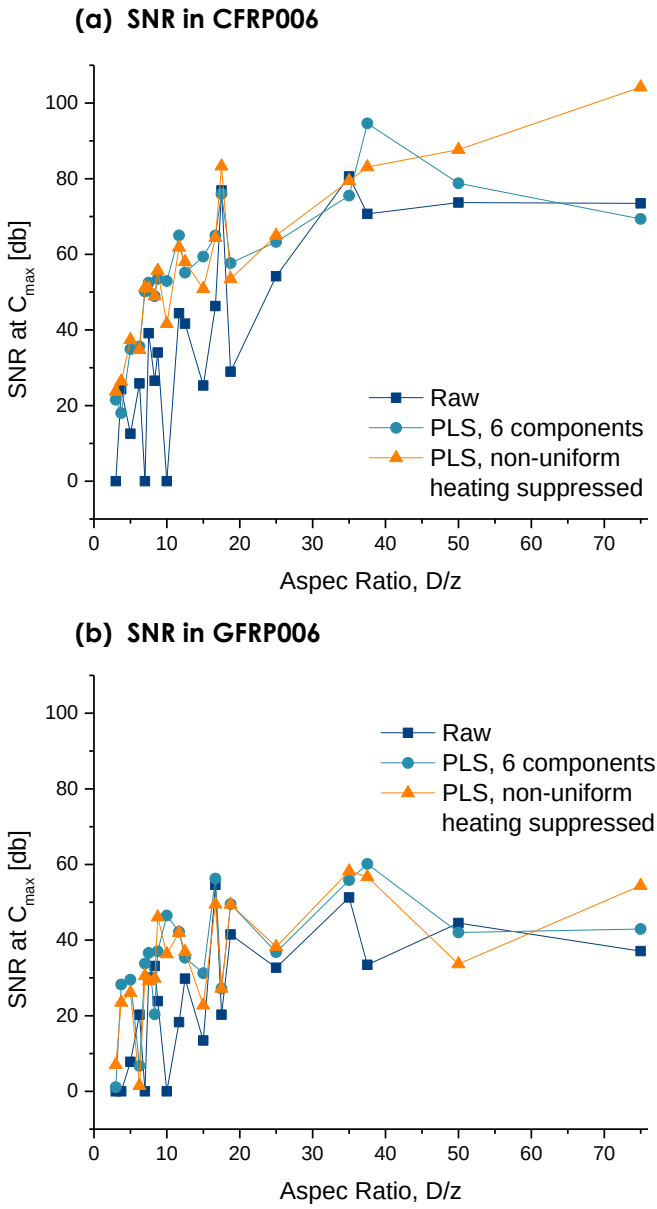

Figure 5.13: Signal-to-noise ratio results in the CFRO006 (a) and CFRO006 (b) after implementation of PLSR.

5.4 Summary

It was shown in previous chapters the necessity of thermographic signal processing in order to overcome most of the constraints produced by non-uniform heating. Despite the great improvement in the quality of the images obtained with Fourier law-based signal processing techniques, their applications are subjected to certain criteria, which include: defect depth, thermophysical properties of the material and duration of the transient regime. For this reason it was prompted the revision of an alternative method that could allow the processing of thermographic data even in cases in which the thermal behaviour of defective areas were not 1D.

The proposed method to 'reconstruct' the thermal data obtained during the inspection is based on partial least squares regression (PLSR), which decomposes the thermographic PT data sequence into a set of latent variables or components. Each latent variable are orthogonal to each other and are characterized by its variance. Thus, it is possible to identify the different phenomena and sources of noise that affect the cooling regime of the PT inspection.

The regression method was tested on experimental PT data from carbon and glass fiber reinforced polymer specimens and its performance was evaluated in terms of signal-to-noise ratio at maximum signal contrasts, using the methodology developed in the last chapter. Through the implementation of the new technique, were achieved an important improvement of the SNR values. In the case of the CFRP006 PT data, a gain the SNR values was obtained in 96 % of the defects. As for the GFRP006 data, it was achieved an increment of the SNR in 64 % of the defects when non-uniform heating was suppressed from the synthetic sequence.

Chapter 6

Quantitative Analysis

The main objective of this Chapter is to develop and test a new method for the inversion of depth and lateral size of defects. The proposed method is based on the statistical correlation between the lateral size and depth with informative parameters obtained during the cooling process (maximum thermal contrast, time of occurrence of the maximum thermal contrast and onset time) followed the pulsed thermal excitation. The correlation between the two block of data (dependent variables and predictors) is carried out using partial least squares regression. A calibration model - or learning phase - is built using results obtained through numerical simulation. The prediction of the dependent block (consisting of the depth and lateral size of 25 defects) is performed using experimental PT data obtained during the inspection of the CFRP006 specimen. The precision of the results are assessed and the capabilities and limitations of the new inversion approach over traditional methods are also analyzed.

6.1 Review of Quantitative Pulsed Thermography

Quantitative analysis represents the final step of the nondestructive testing and evaluation chain. Once the defects has been identified, it is of interest to characterize them quantitatively in order to judge their severity. Defect depth and lateral size are the most commonly parameters studied; however, other parameters such as the thermal properties of the defects are often assessed.

In general terms, the characterization of the defects is performed from the measured temporal and spatial thermal response obtained during the inspection by PT. Several studies have proposed interesting inversion procedures [i.e., statistical method (Vallerand and Maldague, 2000), neural

networks (Maldague and Couturier, 1997) or wavelet transform (Galmiche and Maldague, 2000)]. However, none of these approaches were able to provide a practical quantitative approach mainly due to the complex calibration steps and lengthy computations (Castanedo, 2005). The most suitable quantitative methods – in terms of applicability and easiness – are derived from the thermal contrast (time based IR data) and phase data.

The inversion of defect depth using thermal contrast is based on the fact that the most important information concerning to the presence and characteristics of the subsurface defects is contained in the cooling process following the pulsed thermal excitation of the material. This issue was studied and analysed in Chapters 3 and 4, where it was showed through numerical and experimental results the relationship between the thermal contrast, its time of occurrence and the onset time with the depth of defects. In Figure 6.1 (top) is shown a representation of the temperature and thermal contrast profile curves for defective and non-defective regions and the informative parameters used in the quantification of depth using IR temporal data. The inversion process relies on the computation of C_{max} and t_{max} obtained from the thermal contrast curve. The following expression to retrieve defect depth was proposed by Balageas et al. (1987):

$$z = A\sqrt{t_{max}}(C_{max})^n \tag{6.1}$$

with parameters A and n obtained from the calibration process. It is important to mention that the calibration process should consider only defects having the same lateral size. This is because the maximum thermal contrast and its time of occurrence are function of both, the depth and lateral size of the defects (see Figure 3.17 in section 3.5.1). This last mentioned constitutes a constraint in the practical applicability of Eq. (6.1) to determine the defect depth, since it is necessary to know or at least has an estimation of the lateral size before performing the regression of A and n onto Eq. (6.1).

As already mentioned, phase data also provides valuable means for retrieving defect depth. Ibarra-Castanedo and Maldague (2004) proposed an inversion technique based on the correlation of depth with its corresponding blind frequency, f_{blind}, i.e. the frequency at which the phase contrast reaches to zero ($\Delta\phi = \phi_d - \phi_{sa} = 0$). Figure 6.1 (bottom) shows a representation of the phase delay and phase contrast profiles obtained after the implementation of PPT [see Eq. (4.6)] to the IR thermal sequence. De-

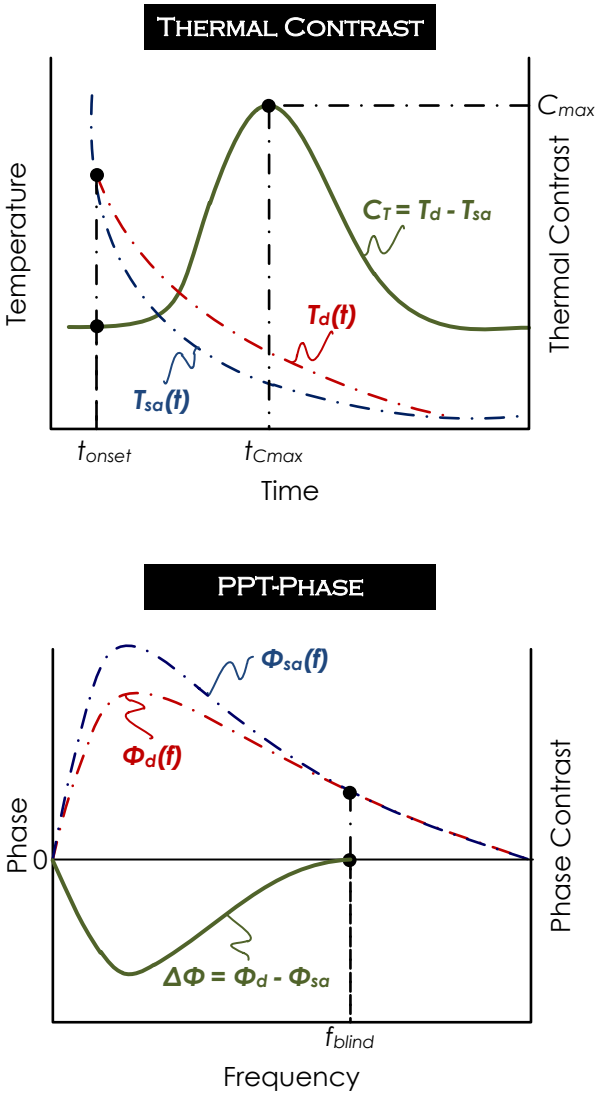

Figure 6.1: Representation of temperature (top) and phase-delay (bottom) profiles for defective and non-defective regions, along with their corresponding thermal and phase contrast curves.

fects are visible from zero to a given frequency, i.e. the blind frequency. In similar manner as in Lock-in Thermography, the defect depth and its blind frequency are correlated to each other through the thermal diffusion wave equation:

$$z = C_1 \cdot \mu = C_1 \sqrt{\frac{\alpha}{\pi \cdot f_{blind}}} \tag{6.2}$$

where C_1 is an empirical correlation constant, f_{blind} is the blind frequency (already introduced) and μ is the thermal wave diffusion equation. As in the thermal contrast method, the correlation constant is obtained from a calibration process and depends among other factors, on the thermophysical properties of the material.

It is well known that the use of phase data to retrieve defect has deeper probing capabilities than IR thermal data (Maldague, 2001). Furthermore, since phasegrams are less sensitive to reflections from the environment and non-uniform heating, the inversion using the blind frequency concept often provides better accuracy than when using Eq. (6.1). Nevertheless, previous results showed that phase data is highly affected with higher-order oscillations (see for instance Figure 4.5) affecting thus the calculation of f_{blind}. For this reason, the correct application of Eq. (6.2) – and consequently the accuracy of the inversion results – requires an additional step to adequately establish the temporal parameters (i.e. truncation window and sampling frequency) that will produce the appropriate frequency response. A carefully study of the acquisition of each temporal signals should be performed and re-adjusted individually, so the best frequency profiles are obtained (Castanedo, 2005).

As already discussed in this section, establishing a correlation between informative parameters (for instance, thermal contrast and blind frequency) and characteristics associated to the subsurface defects is a challenging task. Depth inversion techniques based on physical models are often restricted to particular situations and require additional calibration steps, arising difficulties when the implementation of these techniques is carried out in uncontrolled environments (outside the laboratory). All these concerns prompted to review of an alternative inversion method that could allow to statistically correlate the most representative parameters obtained during the cooling process regime with characteristics associated to the subsurface defects, such as depth and lateral size. This new method is discussed next.

6.2 Multivariate-based Method for Inversion of Defect Depth and Lateral Size

Before introducing the concepts of the proposed inversion method, it is important to recall some results obtained in Chapter 3. When considering uniform distribution of irradiation, simulation results showed that the values of the maximum thermal contrast (C_{max}) and its time of occurrence (t_{max}) are influenced by the depth and lateral size of the defects (see Figure 3.17). The influence is more evident as the value of the defect depth increases. Furthermore, it was also shown that the onset time (t_{onset}) depends solely on the defect depth (see Figure 3.18); both variables (z and t_{onset}) are highly correlated.

From the above results it is evident that the difficulties in establishing a relationship between the informative parameters (or variables) obtained during the cooling process (t_{max}, C_{max} and t_{onset}) with the depth and lateral size of the defects resulting from the nonlinearities present in the heat diffusion problem. In addition to this, multicollinearity between the variables represent a constraint when typical regression techniques are implemented (such as multiple linear regression - MLR). Interestingly, partial least squares regression represents an alternative and a valuable tool to analyze noisy and strongly correlated data (unlike MLR) and also simultaneously model several response variables, such as the considered in this Thesis.

In Chapter 5 the application of partial least squares regression was introduced and tested as a signal processing technique of thermographic data obtained during the PT inspection. This section extend the application of this regression technique in the quantitative analysis of subsurface defects, through the statistical correlation between the variables C_{max}, t_{max} and t_{onset} with defect depth and lateral size. To this aim, a training set consisting of simulated data is used first. In this way only the most representative information is used to build the model and also it will allow to study the noise effects on the performance of the regression technique. Then, the prediction of the dependent variables (z and D) is carried out using experimental data obtained during the PT inspection of the CFRP006.

Next section explains the formulation and data structure of the training data used in the calibration model.

6.2.1 Data structure and methodology

The goal of PLS regression is to predict **Y** (response or dependent variables) from **X** (predictors or independent variables) and to describe their common structure. Both matrices have the following structure:

$$Y_{(25\times 2)} = \begin{pmatrix} z_{1,1} & D_{1,2} \\ z_{2,1} & D_{2,2} \\ \vdots & \vdots \\ \vdots & \vdots \\ z_{25,1} & D_{25,2} \end{pmatrix}$$

$$X_{(25\times 3)} = \begin{pmatrix} t_{max\ 1,1} & C_{max\ 1,2} & t_{onset\ 1,3} \\ t_{max\ 2,1} & C_{max\ 2,2} & t_{onset\ 2,3} \\ \vdots & \vdots & \vdots \\ \vdots & \vdots & \vdots \\ t_{max\ 25,1} & C_{max\ 25,2} & t_{onset\ 25,3} \end{pmatrix} \tag{6.3}$$

The response matrix **Y** has dimensions 25×2, each column representing the depth and lateral size of 25 defects. In the other hand, the predictor matrix **X** has dimension 25×3 and each column corresponds to the computed values of thermal contrast, time of occurrence of C_{max} and the onset time of the 25 defects in the CFRP006 specimen. The values of z, D, C_{max}, t_{max} and t_{onset} used in the calibration model are reported in Table 6.2.1.

The prediction of matrix **Y** by the independent block **X** is carried out by first decomposing **X** into latent variables (or PLS components). This process was already discussed in Chapter 5 (see section 5.1 for details concerning to the mathematical formulation and the iterative procedure of PLS). From the decomposition of the independent block, a set of loadings **p**, scores **t**, weights **w** and coefficients **b** are obtained and used to build up the fitted response $\hat{\mathbf{Y}}$. This stage is known as the calibration or training process. The fitted response is given by :

$$\hat{Y} = XB = TT^T Q = TQ^T \tag{6.4}$$

Table 6.1: Depth and lateral sizes of the defects and computed values of maximum thermal contrast, its time of occurrence and onset time obtained from numerical simulation results.

Index	**z [mm]**	**D [mm]**	t_{max} **[s]**	$C_{max}[^{\circ}\mathrm{C}]$	t_{onset} **[s]**
1	0.2	15	0.0446	3.0164	0.0064
2	0.2	10	0.0446	3.0174	0.0064
3	0.2	7	0.0446	2.9649	0.0064
4	0.2	5	0.0446	2.8131	0.0064
5	0.2	3	0.0382	2.6213	0.0064
6	0.4	15	0.2866	0.7853	0.0382
7	0.4	10	0.2611	0.8030	0.0382
8	0.4	7	0.2420	0.7824	0.0382
9	0.4	5	0.2102	0.6910	0.0382
10	0.4	3	0.1847	0.5953	0.0382
11	0.4	15	0.5541	0.4150	0.1083
12	0.6	10	0.5096	0.4075	0.1083
13	0.6	7	0.4650	0.3788	0.1083
14	0.6	5	0.4076	0.3039	0.1083
15	0.6	3	0.3567	0.2398	0.1083
16	0.8	15	0.8408	0.2429	0.2930
17	0.8	10	0.8025	0.2113	0.2930
18	0.8	7	0.7516	0.1751	0.2930
19	0.8	5	0.6624	0.1195	0.2930
20	0.8	3	0.6051	0.0794	0.2930
21	1.0	15	1.0318	0.1943	0.4713
22	1.0	10	1.0064	0.1588	0.4713
23	1.0	7	0.9554	0.1238	0.4713
24	1.0	5	0.8662	0.0771	0.4713
25	1.0	3	0.7962	0.0468	0.4713

In the other hand, the prediction of the matrix ($\hat{\mathbf{Y}}_\mathbf{p}$) from a new observation set of predictors ($\hat{\mathbf{X}}$) is obtained via the formula:

$$\hat{Y}_p = \hat{X}B \tag{6.5}$$

The new observation set of predictors ($\hat{\mathbf{X}}$) corresponds to the values of maximum thermal contrast, time of occurrence of C_{max} and onset time obtained from the experimental PT inspection. It is important to point out that the regression coefficients matrix **B** is computed from the scores obtained in the calibration process, using the original **X** matrix (see the NIPALS algorithm discussed in section 5.1.3).

The methodology developed for the implementation of PLSR as a inversion method is depicted Figure 6.2. As already mentioned, the calibration model is built up using the results obtained through the numerical simulation of the PT inspection on the CRP006 specimen. From the cooling process, the informative parameters are computed and then matrix **X** and **Y** are built and arranged in the same form as shown in Eq. (6.3).

The next step is the decomposition of **X** into latent variables (which are also relevant for **Y**) through the application of the PLSR. As mentioned in Chapter 5, the PLS regression searches for a set of components that performs a simultaneous decomposition of **X** and **Y** with the constraint that these components explain as much as possible of the covariance between **X** and **Y**. This condition is precisely the main advantages of PLSR over other regression methods, such as MLR and PCR (Abdi, 2003). Before performing the bilinear decomposition it is important to select the number of PLS components needed to obtain the best generalization for the prediction of the new observation. This is the model dimensionality and as in Chapter 5, the variable adopted to test the quality of the model is the root mean square error [Eq. (5.4)], which is a measure of the difference between the original **X** and the new matrix obtained after the deflation of **X** into latent variables. Figures 6.3 shows the estimated RMSE along with cumulative variance explained in X, both as a function of the number of PLS components. It is important to note that in spite approximately 94 % of the variance is captured in the 1^{st} PLS component, the RMSE still remains high. From this results, the optimum number of PLS components using to build the model was set to 3.

The result of the bilinear decomposition of **X** and **Y** is a set of loadings, scores, weights and coefficients. The coefficients matrix **B** is then used to obtain the fitted response [Eq. (6.4)] and also to predict $\hat{\mathbf{Y}}$ [Eq. (6.5)]

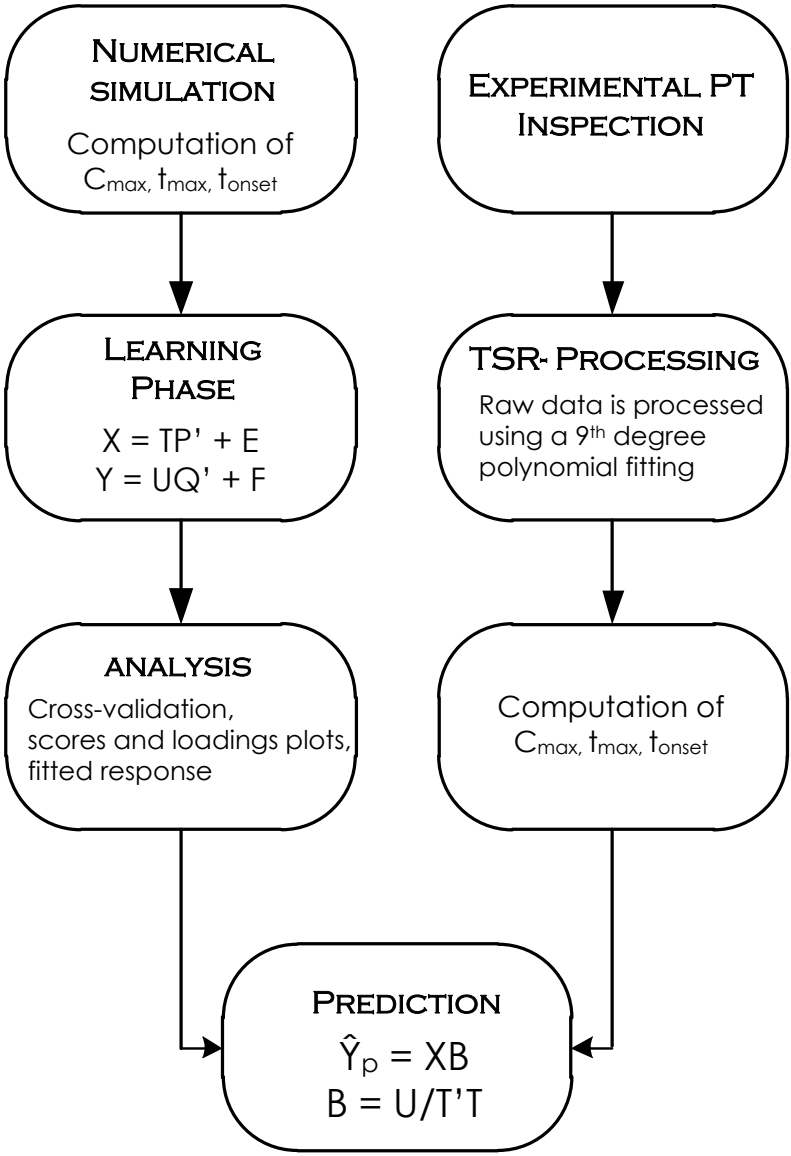

Figure 6.2: Methodology implemented for the prediction of defect depth and lateral size using partial least squares regression.

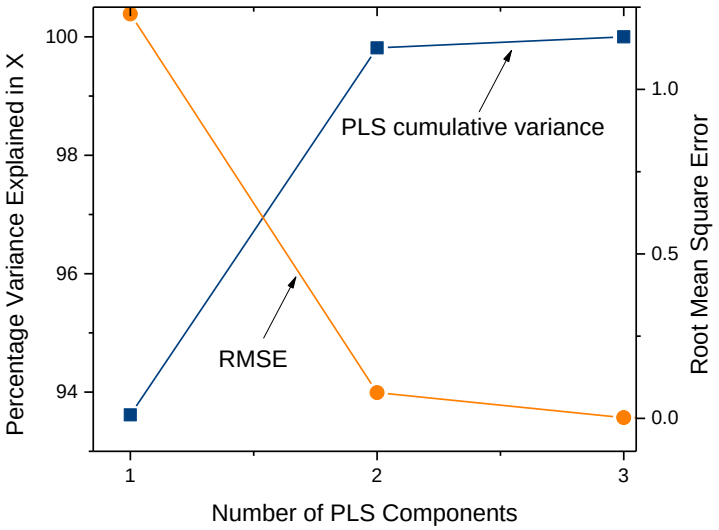

Figure 6.3: Root mean square predicted error and cumulative variance in X as function of the number of PLS components.

from a new observation matrix $\hat{\mathbf{X}}$. However, as is shown in Figure 6.2, an extra stage of processing the PT data has been included before performing the regression of $\hat{\mathbf{Y}}_\mathbf{p}$ from the experimental data $\hat{\mathbf{X}}$. The processing of the raw data was necessary due to the noise affecting the IR signals especially in deeper defects. Without performing this processing stage, the accuracy of the computation of the informative parameters would be seriously affected. Thermographic Signal Reconstruction [as proposed by Shepard et al. (2002) and Ibarra-Castanedo et al. (2009)] was applied to the raw thermal data using a 9^{th} degree polynomial fitting. Such high degree polynomial proves effective for signal de-noising with reduced 'ringing' effects (López et al., 2014).

Once the experimental PT data has been processed, C_{max}, t_{max} and t_{onset} can be computed more accurately and the matrix $\hat{\mathbf{X}}$ is assembled. The final step is the prediction of $\hat{\mathbf{Y}}_\mathbf{p}$ (consisting of the 25 values of depth and lateral size of the defects present in the CFRP006 specimen) using the regression coefficients obtained in the learning phase.

Next section is dedicated to discuss the calibration results as well as the exploratory analysis of the PLS latent variables.

6.2.2 Exploratory analysis and fitted response

In previous sections was shown that through the analysis of the scores and loadings important insights concerning to the relationship between samples, variables and PLS components can be retrieved [see for instance section 5.2.3]. Figure 6.4 shows the loadings (a) and scores plots (b) of the PLS model. As discussed earlier, the relationship between variables can be analysed from the loadings plot, whilst the relationship between samples can be obtained from the scores plot. As depicted in Figure 6.4a, t_{onset} is the most unique variable in this data set. The distance between t_{onset} and its nearest neighbor is further than that t_{onset} and any other variable in the plot. Moreover, it is important to note that C_{max} and t_{max} are close to each other, which is an indication that both variables are somehow correlated. Those variables load most significantly into the first PLS component (are furthest from zero in the left-right direction on the plot) and also they load with opposite sign, which indicate that they are anti-correlated (it makes sense since deeper defects require more time to be detected with a reduced thermal contrast).

Concerning to the scores plots, it can be observed from Figure 6.4b that some samples form small groups called clusters, which are similar to each other. Defects located at 0.2 *mm* are the most unique samples and they load the most to the 2^{nd} PLS component. These results confirm previous analysis (see Figure 5.9) in the sense that the defects located at 0.2 *mm* are not correlated to the rest of the data. It can be also observed from Figure 6.4b that as long as the depth increases, the correlation between samples having the same depth becomes lower. This can be explained as a consequence of the lateral heat diffusion, which becomes more predominant as the depth increases.

Figures 6.5 and 6.6 show respectively the fitted response of depth and lateral size after performing the PLS regression. Both - the fitted depth and lateral size - are plotted against their actual values. The fitted response can be considered as the ability of the PLS latent variables to reconstruct the original dependent block. It is possible to observe from Figure 6.5 that in general terms, PLSR can precisely estimated the depth of all defects. However, the largest difference between actual and estimated values correspond to the defects located at 0.2 *mm*, which interestingly, correspond to the most unique samples (the most uncorrelated to the rest of the data).

(a) PLS Loadings plot

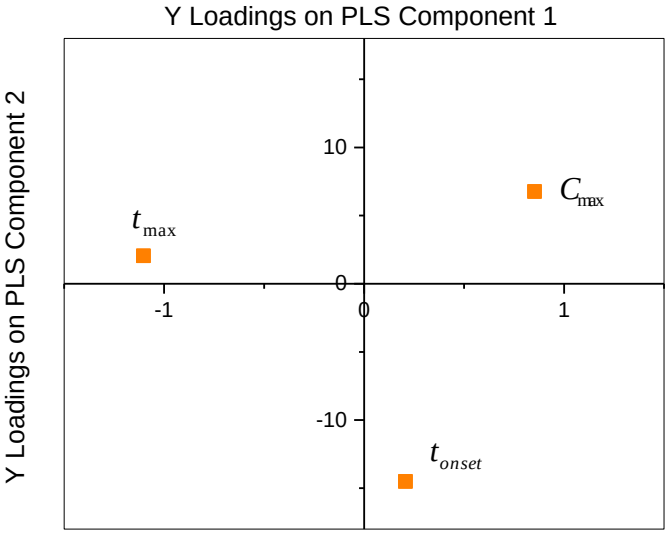

(b) PLS Scores plot

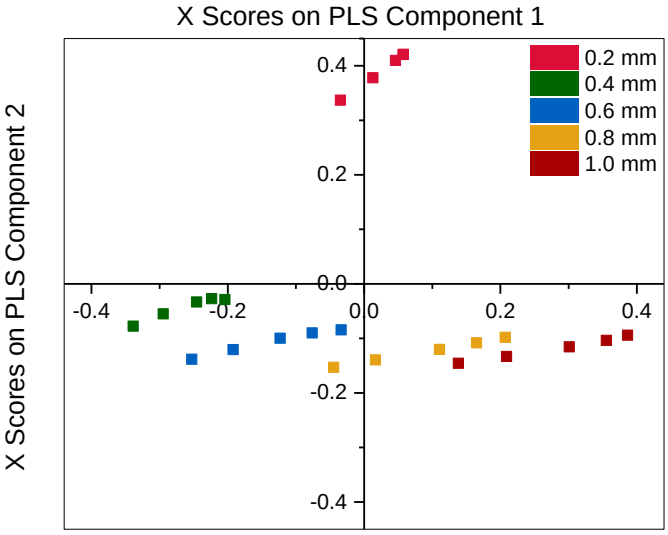

Figure 6.4: Loadings (a) and scores (b) plots of the PLS model.

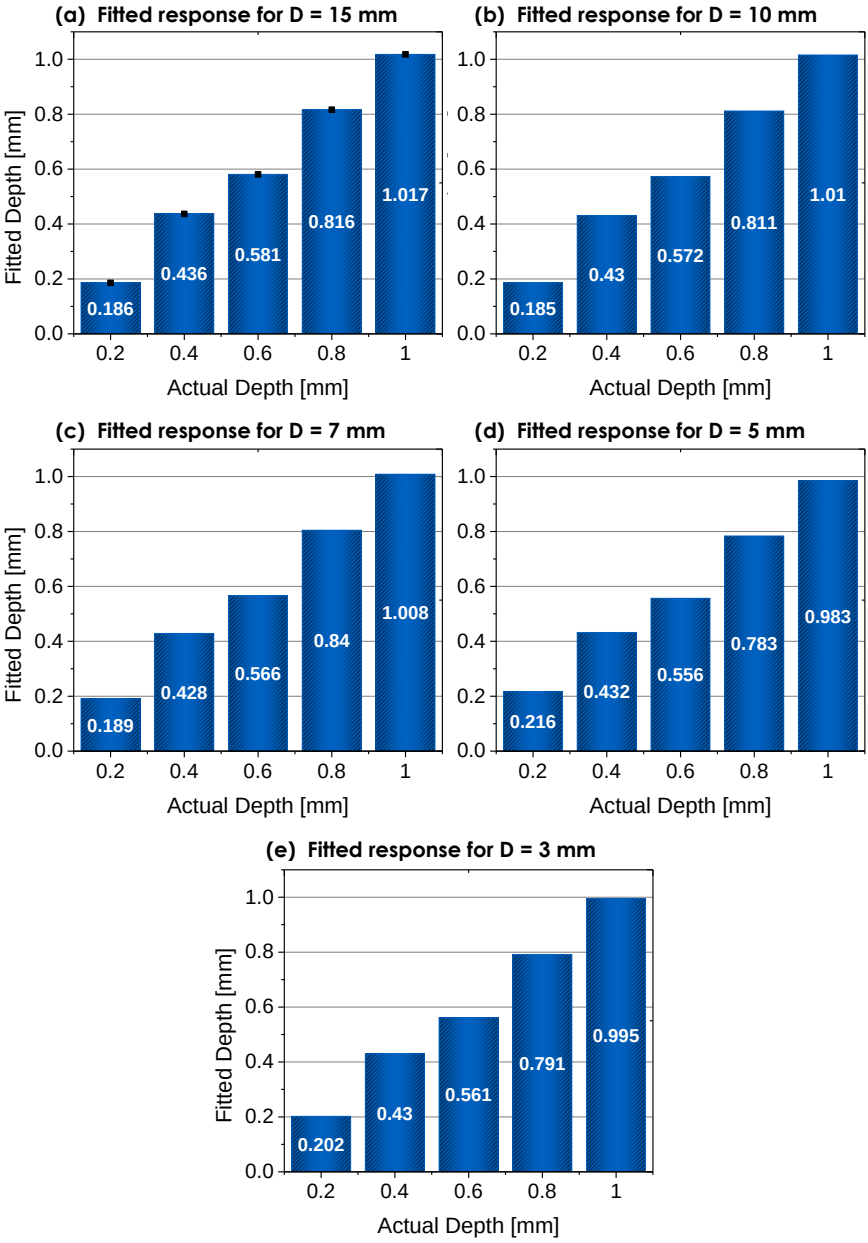

Figure 6.5: Fitted response of defect depths obtained after performing PLSR.

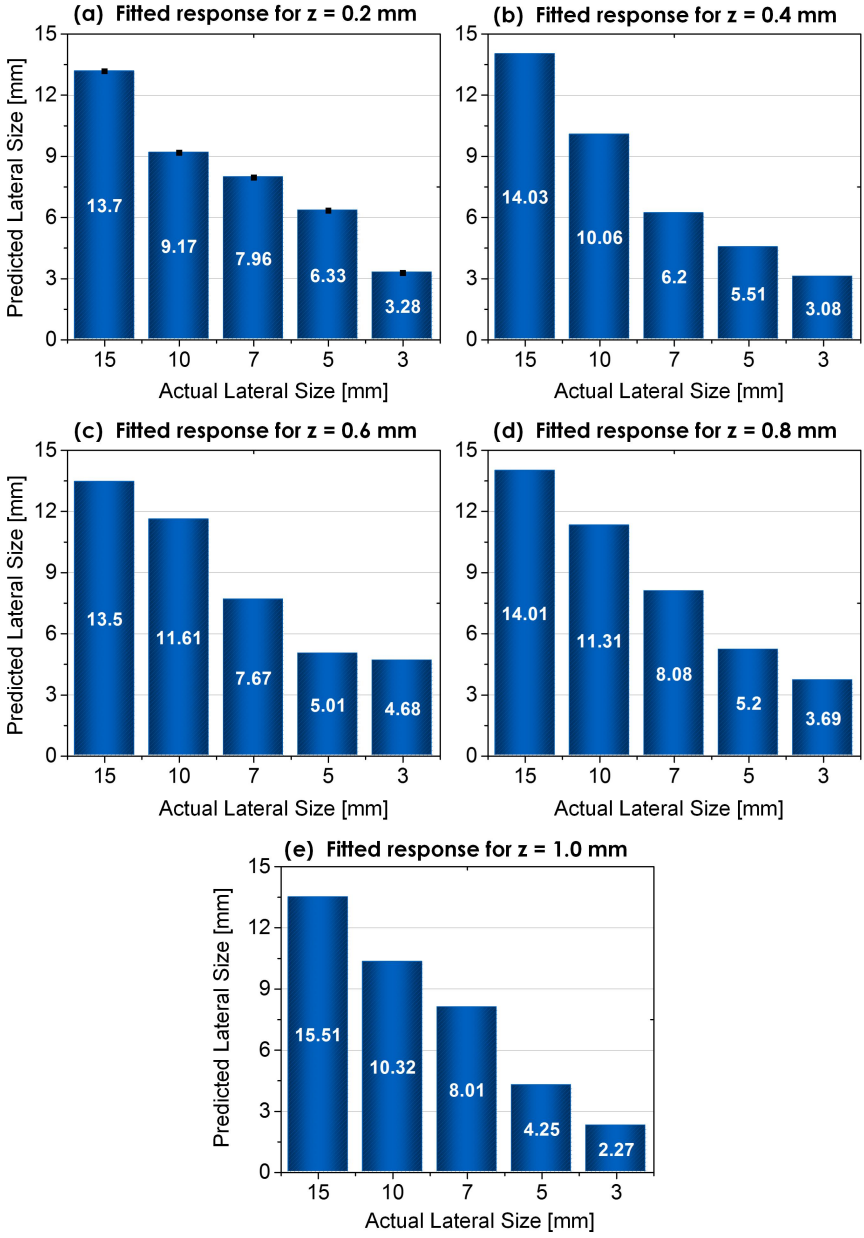

Figure 6.6: Fitted response of defect lateral sizes obtained after performing PLSR.

As per the lateral size, Figure 6.6 shows also a good agreement between actual and fitted values of D. Once again, the highest difference between actual and estimated values of lateral size correspond to the defects located at 0.2 *mm*.

The accuracy of the fitted response of both quantities - D and z - is evaluated in terms of the percentage error, calculated using the following expression:

$$PercentageError = \frac{V_{actual} - V_{fitted}}{V_{actual}} \tag{6.6}$$

The computed values of the percentage error for the depths and lateral sizes are depicted Figures 6.7 and 6.8, respectively. Concerning to the fitted depth, the maximum errors correspond to the defects located at 0.2 and 0.4 *mm*. As already explained, the fact that the defects with $z = 0.2$ *mm* are not similar to the rest, can lead to obtain coefficients that do not necessary better explain the systematic variation of these samples.

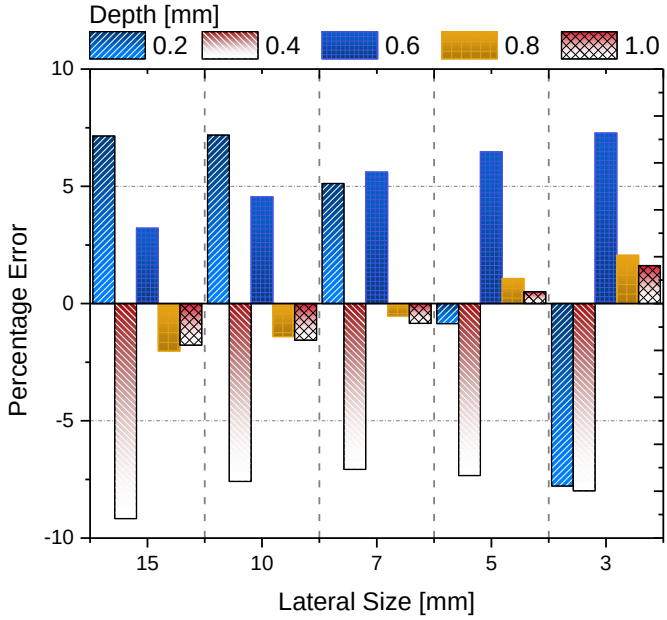

Figure 6.7: Percentage error of the fitted depth obtained with PLS regression.

It is also important to observe that the errors for defects with lateral size $D = 3\ mm$ are higher than the obtained with the other values of D. This can explained as a consequence of the size of the region (or number of pixels) that was selected as a sound area, which may not be the most representative sample. As is well known, an inadequate sample can produce higher values of standard deviation, affecting this way the computation of the temperature [see Equations (3.25)].

As is showed in Figure 6.8, despite that the percentage errors for the fitted lateral sizes are higher than the obtained with the depths, PLS regression can still estimate D precisely for almost all the defects. The highest errors correspond to the defects with $D = 3\ mm$, which as already explained, the size of the region of the sound area could not have been the most appropriate. The rest of the fitted values of lateral size has percentage errors below 15 %.

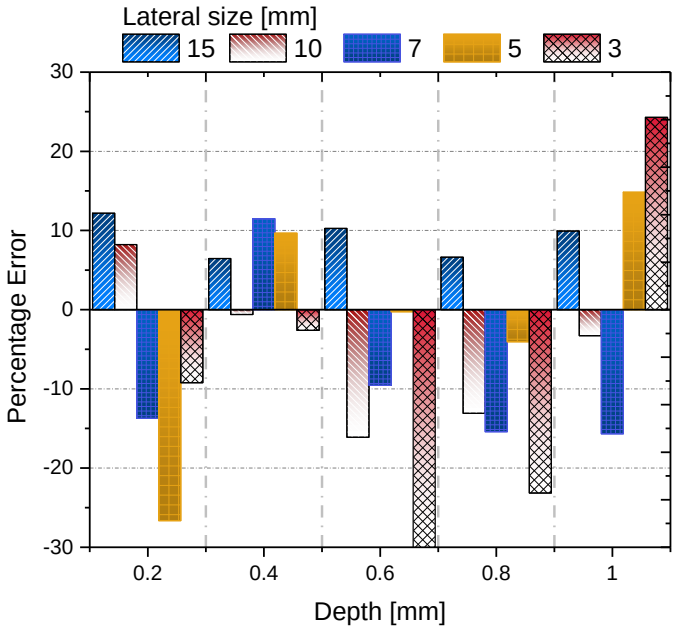

Figure 6.8: Percentage error of the fitted lateral size obtained with PLS regression.

6.3 Comparative Analysis

Looking back at the methodology shown in Figure 6.2, the next and final step is the prediction of the depth and lateral size of the defects from a new observation. As already explained, this new observation matrix $\hat{\mathbf{X}}$ consists of the computed values of C_{max}, t_{max} and t_{onset} obtained from the experimental PT inspection on the CFRP006 specimen. In this stage the calibration model is tested and evaluated using real data, which in spite of being processed with TSR, it is still contaminated with different sources of noise. The prediction results and the performance of PLSR as a inversion technique are evaluated using two different methods: through the comparison of the predicted depth using the method of maximum thermal contrast proposed by Balageas et al. (1987) (see section 6.1), and through the computation of the root mean squared error of prediction (RMSEP).

In order to produce a fair comparison, the computation of depth using Eq. (6.1) was performed using the same processed data used in PLSR. The maximum thermal contrast and its time of occurrence of all 25 defects were first computed and then, for each lateral size, it was plotted $log[z_d/(tmax)^{1/2}]$ as a function of $log[C_{max}]$. The two coefficients of Eq. (6.1) (n and A) were determined through a linear regression.

Table 6.2 shows the regression coefficients obtained during the learning phase of PLSR. Matrix $\mathbf{B}$ has dimension 3×2, each row representing the regression coefficient of the original predictor. Important insights can be obtained from Table 6.2: the onset time is the most representative variable for describing the defect depth (which is in agreement to previous results), whilst the time of occurrence of the maximum thermal contrast is the responsible variable for the prediction of the lateral size of defects.

Table 6.2: PLS regression coefficients used for the prediction of depth and lateral size of defects.

	z	**D**
t_{max}	0.1932	40.8808
C_{max}	-0.0787	4.1392
t_{onset}	0.9018	-1.6508

At this stage it is important to note the reduction achieved with PLSR in the number of coefficients required to predict both variables (z and D). With the method proposed by Balageas et al. (1987), the dimension of the regression coefficient matrix is 25×2, while with PLSR the matrix is reduced to 3×2.

Figure 6.9 shows the depth inversion results using PLSR and Eq. (6.1). Both results are plotted against the actual depth and as a function of the lateral size of the defects. Considering the defects with $D = 15mm$, PLSR shows better performance than with the obtained using Eq. (6.1); only the prediction of the defect with $z = 0.2\ mm$ showed better results using the method proposed by Balageas et al. (1987). As long as the lateral size of the defects increases, the performance of PLSR over the C_{max} method increases. In only 24 % (6/25) of the cases, the prediction errors with the C_{max} method were lower than the obtained with PLSR.

The overall performance of PLSR and its ability to predict the defect depth using data contaminated with noise are confirmed with the results showed in Figure 6.9. In spite that the most important prediction errors were found in the defects located at $z = 0.2\ mm$, the results obtained with PLSR showed better accuracy when compared to one of the most traditional method using in quantitative analysis of pulsed thermography. In this regards it is important to remember that the onset time is the most important variable to predict the defect depth (see the regression coefficients showed in Table 6.2) and also it is the most sensible and difficult to obtain specially in shallowest defects, due to the saturation effects present in the first frames of the acquisition. It is because of this difficulties that the most accurate prediction results were achieved with the deeper defects.

The prediction results of the lateral size of defects are depicted Figure 6.10. As in previous cases, the predicted values are plotted against the actual. Results showed that the most important errors between predicted and actual values are in the defects with $z = 0.2\ mm$; this error was expected and already discussed in earlier sections. However, as long as the depth increases, the accuracy of the prediction becomes better. As shown in Figure 6.10c, predictions results for defects with $z = 0.6\ mm$ are quite accurate, even in the defect with the smallest lateral size ($D = 3\ mm$). However, it can be observed a large error when considering the defect with aspect ratio $D/z = 3/1.0$. This error can be explained as a consequence of the poor signal of temperature which can lead to produce errors when computing the thermal contrast.

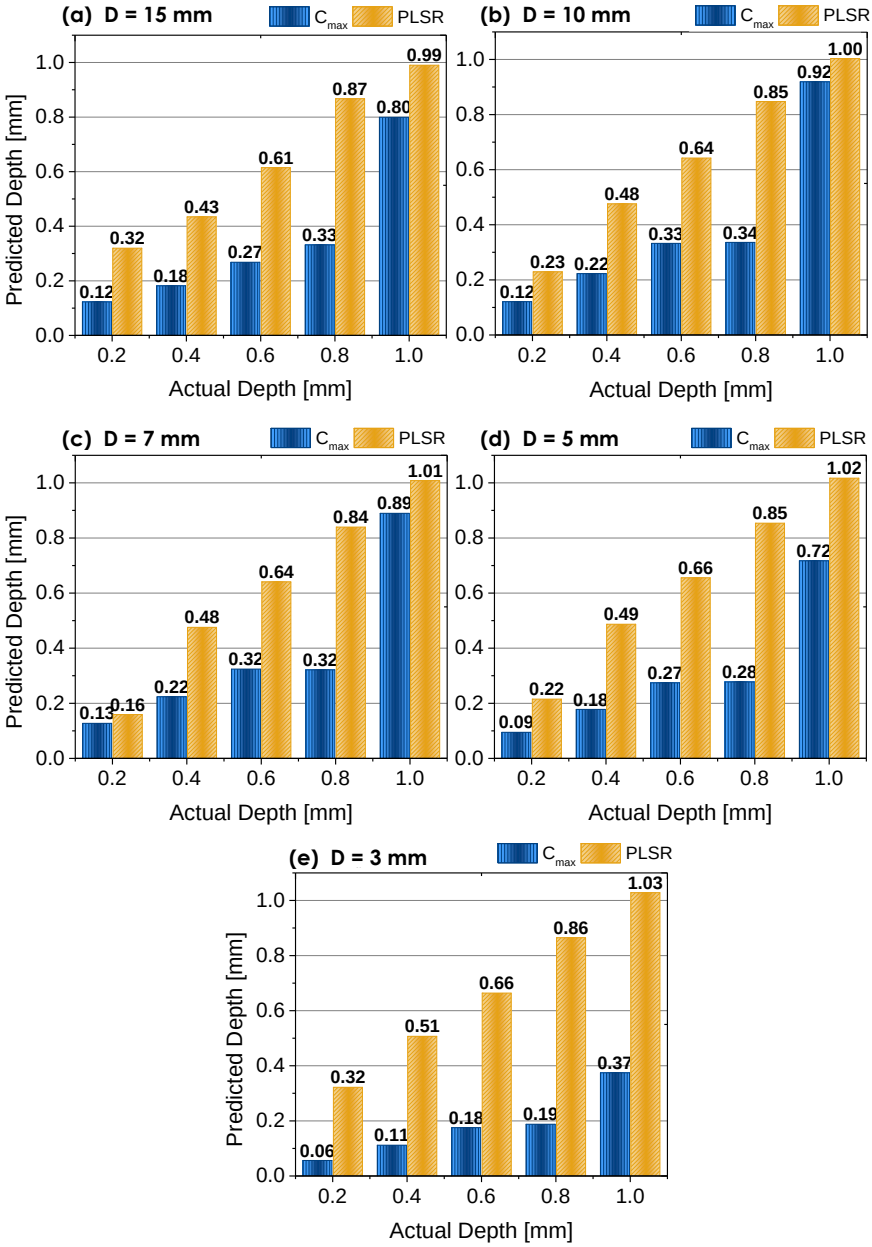

Figure 6.9: Comparison between predicted values of depth computed with the C_{max} method and PLSR.

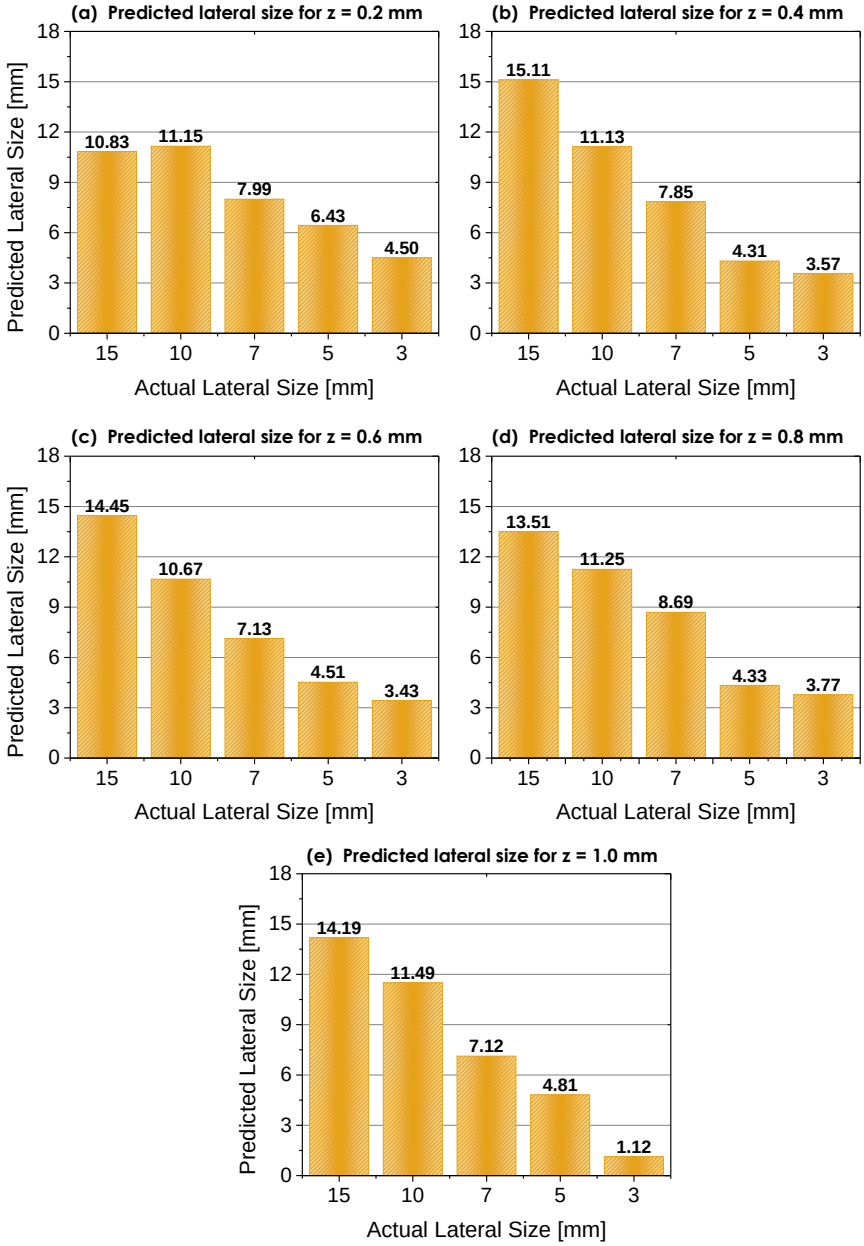

Figure 6.10: Predicted values of lateral size of defects using PLSR.

Table 6.3 shows a comparison of the RMSE (root mean square error) of the fitted response and predicted values of depth [obtained with PLSR and using Eq. (6.1)] and lateral size. It can be observed that the RMSEP for the fitted response of lateral size is higher than the obtained with depth. Since those values are obtained in the absent of experimental noise, it can be concluded that the predictor variables were more effective in predicting the depth (in this case, t_{onset}) than the lateral size of the defects. This issue could represent a beginning in research concerning to other informative parameters that could represent better the lateral size of the defects.

In the other hand, the prediction of depth using PLSR showed to be more effective (in terms of applicability and accuracy) in predicting depth compared to the results obtained via the C_{max} method (0.0602 vs. 0.3274). In spite that the RMSP of the lateral size was higher than the obtained with the depth, PLSR proved to be an effective and a straightforward method for retrieving D in a very anisotropic specimen.

Table 6.3: Root mean square error for prediction of depth and lateral size. All values given in mm.

	Fitted		Predicted		
	z_{PLS}	D_{PLS}	z_{PLS}	z_{Cmax}	D_{PLS}
RMSEP	0.0228	1.0160	0.0602	0.3274	1.2975

6.4 Summary

Quantitative analysis is the final step of the nondestructive testing and evaluation chain. Once the defects has been identified, it is of interest to characterize them quantitatively in order to judge their severity. Defect depth and lateral size are the most commonly parameters studied; however, other parameters such as the thermal properties of the defects are often assessed.

Most of the techniques currently used to characterize defect depth and geometry are based on the analysis of the measured temporal and spatial thermal response obtained during the inspection by PT. The most suitable quantitative methods are derived from the thermal contrast (time based IR data) and phase data. However, these methods present limitations. In the case of the method based on the computation of the maximum thermal contrast, its applicability is limited by the observation time. In the other hand, the inversion of depth using phase data requires complex analysis of the temporal signals in order to reproduce an appropriate response in the frequency domain.

This chapter presented a new inversion method for retrieving depth and lateral of size of defects. The method is based on the correlation between related parameters of the defects (the dependent block) with the informative parameters obtained during the cooling process of the PT inspection (the independent block). Results obtained from numerical simulation were used to built up a calibration model. Using partial least squares regression, the independent block of data (consisting on the 25 values of thermal contrast, its time of occurrence and the onset time) was decomposed into latent variables, from which regression coefficients were obtained and the prediction of depth and lateral size was performed straightforward from a new predictor matrix. The results were compared with traditional methods in order to evaluate its performance. The accuracy of the prediction of depth obtained with the new method was higher than the obtained with the c_{max} method.

Chapter 7

Conclusions, Main Contributions and Future Works

Below are presented the conclusions, main contributions of this thesis and recommendations for future works concerning to infrared thermography (IRT) as a nondestructive testing and evaluation (NDT&E) technique:

7.1 Conclusions

Chapter 2

This chapter reviews the fundamentals concepts of pulsed thermography as a NDT&E technique. The different steps necessary to implement this technique were also discussed. Furthermore, it was presented the inspection system used during the development of this thesis and also it was discussed relevant information concerning to the acquisition and analysis of the thermographic data.

Non-uniform heating and blurring (produced by the lateral heat diffusion) are the most harmful effects that PT has to deal with. Non-uniform heating is caused by several factors, such as different properties on the material surfaces and the uneven heating applied during the thermal excitation. In the other hand, blurring is a problem caused when the heat diffusion process in the lateral directions becomes predominant. Most of the defects will suffer from blurring but deeper defects or those with smaller aspect ratio are the most sensitive. Both - non-uniform heating and blurring - are unavoidable, at least until today. Different techniques has been developed in order to overcome those problems. Most of them transform the thermal data into another domain or space less sensitive to the typical problems arising in the PT inspection.

Chapter 3

In this chapter was described a step−by−step methodology for the development of a thermal-numerical model for the simulation of a pulsed thermography inspection on carbon fiber laminated composites. The numerical simulation tool − which was theoretically and experimentally validated − provided means for the understanding of the heat diffusion interaction with internal defects and the response of the surface thermal pattern. A parametric study was conducted and the analysis was based on the response of the onset time (t_{onset}), maximum thermal contrast (C_{max}) and its time of occurrence (t_{C_max}), when varying parameters related to the geometry of the defects and the external thermal excitation.

The numerical study revealed that non-uniform heating, the irradiation power density and parameters associated with the defect geometry (lateral size and thickness) strongly affect the maximum thermal contrast. On the other hand, the onset time and the time of occurrence of the maximum thermal contrast are not affected by non-uniform heating, the irradiation power or the defect thickness. These results presented herein suggest that the most appropriate quantitative variables that should be considered to determine the defect depths are the onset time and time of occurrence of the maximum thermal contrast. This issue was covered in Chapter 6.

Chapter 4

In this chapter the basic principles of three of the most attractive signal processing techniques have been discussed in details as well as their implementation in PT inspection data of carbon and glass fiber reinforced polymers. Along with experimental and heat transfer concepts, a methodology to study the application and performance of the techniques on two different specimens has been developed. For the case of the CFRP006 specimen, results showed that - even in detectable defects - it is possible to obtain an improvement on defects visibility especially with pulsed phase thermography (PPT) phase images and 1^{st} derivative images. In spite that differential absolute contrast (DAC) provides good signal-to-noise ratio (SNR) for defects with aspect ratio greater than 37, its performance is affected as D/z becomes smaller. This can be due to the deviation from the 1D thermal behavior which affects deeper defects.

The results in glass fiber reinforced polymers showed that 1^{st} derivative and PPT phase images provide in overall the highest SNR at maximum signal contrast, followed by DAC and 2^{nd} derivative images. DAC produced SNR values comparable to PPT and thermographic signal re-

construction (TSR) 1^{st} derivatives in the case of defects with larger aspect ratio.

The study performed in this chapter allows to conclude that in spite that most of the defects can be detected with raw data, the application of a signal processing technique to the pulsed thermography thermal sequences provides an important improvement of signal quality. This signal improvement can prevent to wrongly interpret an artifact as an internal defect (or vice versa), along with a better precision when quantitative analysis is performed. Moreover, it can be concluded that the SNR at maximum signal contrast - and consequently, the performance of each technique - is a function of several factors, being the most important: thermal properties of the specimen, aspect ratio of the defects and especially, the acquisition parameters of the inspection. While thermographic signal reconstruction (TSR) and DAC suffer the potential consequences of undersampling, PPT does not (since its more valuable information is at lower frequencies).

Chapter 5

In this chapter a new method of processing thermographic signals has been proposed and tested on experimental PT data of carbon and glass fiber-reinforced polymer. The technique, which is based on partial least squares regression, produces a new set of thermal images constructed from the decomposition of the original data into latent variables. Through an in-depth analysis of the latent variables, it was possible to identify and separate the components associated to non-uniform heating. Thus, a new sequence of images was created without the harmful effects of non-uniform heating and with a considerable reduction of background noise.

The analysis of the latent variables (or components) was extended to the loadings and scores plots from which it was possible to identify several measurements and samples that are not correlated to each other. The results obtained from this analysis was extremely useful in the quantitative analysis of subsurface defects (see for instance Chapter 6). The performance of the method proposed herein was analyzed using the signal-to-noise ratio. In the case of the CFRP006 PT data, results showed a gain in the SNR values after processing the images with partial least squares (PLSR) in the case of 88 % of the defects. After suppression of the non-uniform heating, the increase in the SNR values was even greater (96 % of the defects). As for the GFRP006 data, it was achieved an increment of the SNR in % 56 of the defects and 64 % when non-uniform heating was suppressed from the synthetic sequence. In spite that the per-

formance of the new processing technique was not good enough when processing GFRP006 thermal data, it provides several advantage over traditional techniques. The most important is the applicability to situations in which the thermal behaviour of defects do not follow the 1D solution of the heat conduction equation. Furthermore, PLSR does not suffers the consequences of under− or over-sampling (conversely to TSR and PPT, respectively).

Chapter 6

In this chapter was developed a new inversion method for retrieving depth and lateral of size of defects. The technique is based on the statistical correlation between related parameters of the defects (the dependent block) with the informative parameters obtained during the cooling process of the PT inspection (the predictor or independent block). A learning or calibration model was built up using numerical simulation results. Using partial least squares regression, the independent block of data (consisting on the 25 values of thermal contrast, its time of occurrence and the onset time) was decomposed into latent variables, from which regression coefficients were obtained and the prediction of depth and lateral size was performed straightforward from a new predictor matrix.

Results showed that onset time is the most important parameter to retrieve the defect depth, whilst the time of occurrence of the maximum thermal contrast represent the most important for the prediction of the lateral size of defects. It was also shown that the new method proved to be effective - in terms of applicability and accuracy - to predict both variables on experimental data. Moreover, the results obtained with the new method showed better performance - evaluated in terms of the root mean square error - than when performing the quantitative analysis using the method proposed by Balageas et al. (1987).

7.2 Main contributions

A computational tool for the simulation of the pulsed thermography inspection on anisotropic materials:

The computational tool meets the most important elements to be taken into consideration when is performed the pulsed thermography inspection. This computational resources is flexible and can be adapted to other types of materials (such as homogeneous materials), structures (multilayered components) and stimulation methods (for instance, lock-in and long-pulse thermography). In addition to be used for the analysis of the

different heat transfer mechanisms, this tool can be used for the technical training.

A methodology to assess the performance of signal processing methods on pulsed thermography data:

The methodology developed allows to conclude - based on quantitative information - the most suitable processing technique given the stimulation method, thermophysical properties of the material and acquisition parameters. Since the SNR is evaluated in the maximum signal contrast, it is possible to determine the maximum level of visibility achieved with different processing algorithms.

A new robust signal processing technique for the analysis of thermographic data:

This new processing method is one the core of this research work. The new technique is robust and flexible, which means that it can be applied to other signals types besides the short-temporal signal obtained in PT. Another important advantage over traditional techniques is its applicability to cases when the heat diffusion is not 1D, conversely to DAC, TSR and PPT. The ability to separate the effects of non-uniform heating represents its major achievement.

A new quantitative method to retrieve depth and lateral size of defects:

This new method allows to correlate the three most important parameters obtained during the cooling process - onset time, maximum thermal contrast and its time of occurrence - to the lateral size and depth of the defects. As in previous cases, this technique addresses the major concern of traditional techniques for the quantitative analysis of defects: their restriction to cases when the heat diffusion process is 1D. Thus, this technique can be applied to deeper defects and longer observation times.

7.3 Recommendations for Future Works

Study the applicability of pulsed thermography to inspect non-planar surfaces:

So far the application of IRT for NDT&E of materials haven been focused on the inspection of planar surfaces. However, there are several situations in which the surface to be assessed is non-planar. For this particular case the inspection by PT present various limitations: the heat emission (was

well as heat absorption) is at its maximum when the normal surface is parallel to the direction of the flow of energy. This variation in the heat transfer problem may lead to reduce the intensity of the signals, producing thus incorrect subsurface defect detection.

Study the applicability of partial least squares regression to other infrared thermography techniques, such as lock-in, vibro- and induction thermography:

The research on PLSR as a signal processing technique was exclusively focussed on the regression and analysis of temporal signatures (i.e., thermal decay curve). However, other stimulation modes require to make the acquisition in steady-state regime (such as LT and modulated VT). It is well known that in the cases of LT and VT, the signals are highly contaminated by higher order oscillation, making more difficult the interpretation process. PLSR can be employed as a means to reconstruct the thermographic signatures and produce smoothed signals.

Include other parameters in the multivariate model – such as thermophysical properties of the material and full-wide half maximum (FWHM) – in order to enhance the accuracy of PLSR as a quantitative technique:

In this research were only used three parameters (maximum thermal contrast, its time of occurrence and the onset time) for the inversion of depth and lateral size of the defects. However, one of the main attraction of PLSR is its ability to deal with a large number of independent variables. This feature can be used in order to improve the accuracy of the prediction results and include in the prediction model other parameters, such as the thermophysical properties of the material and the internal defects.

Bibliography

D.P. Almond and P.M. Patel. *Phothermal Science and Techniques: Physics and its Applications*. Chapman and Hall, London, UK, 1st edition, 1996. 28, 77

N. Avdelidis and D. Almond. Transient thermography as a through skin imaging technique for aircraft assembly: modeling and experimental results. *Infrared Physics & Technology*, 45:103–114, 2004. 28

D. Balageas. Defense and illustration of time-resolved pulsed thermography for nde. In *Proc. of SPIE Vol. 8013, 80130V. Thermosense: Thermal Infrared Applications XXXIII*, Baltimore, 2011. 6

D.L. Balageas, A.A. Déom, and D.M. Boscher. Characterization and nondestructive testing of carbon-epoxy composites by a pulsed photothermal method. *Materials Evaluation*, 45:461–465, 1987. xlii, 21, 118, 133, 134, 142

T. Bergman, A. Lavine, F.P. Incropera, and D.P. DeWitt. *Fundamentals of Heat and Mass Transfer*. John Wiley & Sons, Inc., New York, USA, tth edition, 2011. 37, 38

Clemente Ibarra Castanedo. *Quantitative Subsurface Defect Evaluation by Pulsed Phase Thermography: Depth Retrieval with the Phase*. PhD thesis, Université Laval, 2005. 118, 120

K. Chatterjee, S. Tuli, S. Pickering, and D. Almond. A comparisonofthepulsed, lock-in and frequency modulated thermography nondestructive evaluation techniques. *NDT&E International*, 44:655–667, 2011. 6

D.P. DeWitt and G. Nutter. *Theory and Practice of Radiation Thermometry*. John Wiley & Sons, Inc., New York, 1988. xxi, 158

Eigenvector, 2006. *Chemometrics Tutorial for PLS Toolbox and Solo*. Eigenvector Research Inc., 2006. 97

F. Galmiche and X. Maldague. Depth defect retrieval using the wavelet pulsed phased thermography. In *Proceeding 5th Conference on Quantitative Infrared Thermography (QIRT), Eurotherm Seminar 64*, Reims, France, 2000. 118

W.G. Glen, W.J. Dum III, and D.R. Scott. Principal components analysis and partial least squares regression. *Tetrahedron Computer Methodology*, 2:349–376, 1989. 95

H. Grahn, N. M. Szeverenyi, M. W. Roggenbuck, F. Delaglio, and P. Geladi. Data analysis of multivariate resonance images i. a principal component analysis approach. *Chemometrics and Intelligent Laboratory Systems*, 5:311–322, 1989. 94

E. Grinzato, V. Vavilov, P.G. Bison, S. Marinetti, and C. Bressan. Methodology of processing experimental data in transient thermal nondestructive testing (ndt). In *Thermosense XVII: An International Conference on Thermal Sensing and Imaging Diagnostic Applications*, Orlando, FL, 1995. 22, 80

Abdi, 2003. *Partial Least Squares (PLS) Regression*. H. Abdi., 2003. 124

Ch. Hellier. *Handbook of Nondestructive Evaluation*. McGraww-Hill, NY, 2003. 1

R. Hidalgo-Gato, J. R. Andrés, J. M. López-Higuera, and F. J. Madruga. Quantification by signal to noise ratio of active infrared thermography data processing techniques. *Optics and Photonics Journal*, 3:20–26, 2013. 70

Y.Y. Hung, Y.S. Chen, S.P. Ng, L. Liu, Y.H. Huang, B.L. Luk, R.W.L. Ip, C.M.L. Wu, and P.S. Chung. Review and comparison of shearography and active thermography for nondestructive evaluation. *Materials Science and Engineering R.*, 64:73–112, 2009. 1

Q. Huynh-Thu and M. Ghanbari. Scope of validity of psnr in image/video quality assessment. *Electronic Letters*, 44:800–801, 2008. 81

C. Ibarra-Castanedo and X. Maldague. Defect depth retrieval from pulsed phase thermographic data on plexiglas and aluminum samples. In *SPIE Procedures Thermosense XXVI*, Orlando, FL, 2004. 35, 118

C. Ibarra-Castanedo and X. Maldague. Interactive methodology for optimized defect characterization by quantitative pulsed phase thermography. *Research in Nondestructive Evaluation*, 14:1–19, 2005. 78

C. Ibarra-Castanedo, D. González, F. Galmiche, X. Maldague, and A. Bendada. Discrete signal transforms as a tool for processing and analyzing pulsed thermographic data. In *Proc. of SPIE, Vol. 6205*, Orlando, FL, 2006. 72

C. Ibarra-Castanedo, A. Bendada, and X. Maldague. Thermographic image processing for ndt. In *IV Conferencia Panamericana de END*, Buenos Aires, 2007a. 79

C. Ibarra-Castanedo, M. Genest, J. M. Piau, S. Guibert, A. Bendada, and X. Maldague. *Ultrasonic and Advanced Methods for Nondestructive Tesing and Material Characterization - Chapter 4: Active Thermography Techniques for the Nondestructive Testing of Materials*. World Scientific Publishing, MA, USA, 2007b. xix, 5, 14, 77, 155

C. Ibarra-Castanedo, J. Piau, S. Guilbert, N. Avdelidis, M. Genest, A. Bendada, and X. Maldague. Comparative study of active thermography techniques for the nondestructive evaluation of honeycomb structures. *Research in Nondestructive Evaluation*, 20:1–31, 2009. 5, 35, 70, 72, 80, 126

M.T. Klein, C. Ibarra-Castanedo, X.P. Maldague, and A. Bendada. A straightforward graphical user interface for basic and advanced signal processing of thermographic infrared sequences. In *Proceedings of the SPIE, Thermosense XXX, Vol. 6939*, Orlando, FL, 2008. 73

J.-C. Krapez, X. Maldague, and P. Cielo. Thermographic nondestructive evaluation: Data inversion procedures.part ii: 2-d analysis and experimental results. *Research in Nondestructive Evaluation*, 3:101–124, 1991. 14, 21, 28

A. Krishnan, L. J. Williams, A. R. McIntosh, and H. Abdi. Partial least squares (pls) methods for neuroimaging: A tutorial and review. *NeuroImage*, 56:455–475, 2011. 94

S. K. Lau, D. P. Almond, and P. M. Patel. Transient thermal wave techniques for the evaluation of surface coatings. *Journal of Physics D: Applied Physics*, 24:428–436, 1991. 6, 28

F. Lopez, V. Nicolau, and X. Maldague. Pulsed phase thermography applied on complex structures: modelling and numerical analysis. In *11th International Conference on Quantitative InfraRed Thermography*, Naples, 2012. 38

F. López, X. Maldague, and C. Ibarra-Castanedo. Enhanced image processing for infrared non-destructive testing. In *Proc. 12th Advanced Infrared Technology and Applications (AITA)*, Turin, Italy, 2013. xiii, 3

F. López, C. Ibarra-Castanedo, X.P. Maldague, and Nicolau V. Pulsed thermography signal processing techniques based on the 1d solution of the heat equation applied to the inspection of laminated composites. *Materials Evaluation*, 72:91–102, 2014. 126

X. Maldague. *Theory and Practice of Infrared Thermography for Nondestructive Testing*. John Willey & Sons, New York, 2001. 2, 4, 5, 14, 15, 21, 22, 120

X. Maldague and J.P. Couturier. Review of pulse phase infrared thermography. In *Proceeding* 4^{th} *International Workshop on Advanced Infrared Technology and Applications (AITA)*, Firenze, Italy, 1997. 118

X. Maldague and C. Ibarra-Castanedo. Defect depth retrieval from pulsed phase thermographic data on plexiglas and aluminum samples. In *Proceedings of the SPIE, Thermosense XXVI, Vol. 5405*, Orlando, Florida, 2004. 78

X. Maldague and C. Ibarra-Castanedo. *Handbook of Technical Diagnistics - Infrared Thermography*. Springer-Verlag Berlin Heidelberg, Berlin, Germany, 2013. xiii, 15

X. Maldague and S. Marinetti. Advances in pulsed phase thermography. *Infrared Physics and Technology*, 42:175–181, 2002. 5, 7, 77

C.R. Maliska. *Transferência de Calor e Mecânica dos Fluidos Computacional*. Livros Técnicos e Científicos Editora S.A., Rio de Janeiro, 2004. 38

S. Marinetti, E. Grinzato, P. Bison, E. Bozzi, M. Chimenti, G. Pieri, and O. Salvetti. Statistical analysis of ir thermographic sequences by pca. *Infrared Physics & Technology*, 46:85–91, 2004. 101

H. Martens. Reliable and relevant modelling of real world data: a personal account of the development of pls regression. *Chemometrics and Intelligent Laboratory Systems*, 58:85–95, 2001. 94

MathWorks, 2010. *Matlab: The Lenguage of Technical Computing*. The MathWorks Inc., 2010. 43

G. Mayr, B. Plank, J. Sekelja, and G. Hendorfer. Active thermography as a quantitative method for non-destructive evaluation of porous carbon fiber reincorced polymers. *NDT& International*, 44:537–543, 2011. 6

M. Modest. *Radiactive Heat Transfer*. Academic Press, United States, 2nd edition, 2003. 154

D. Montgomery and G. Runger. *Applied Statistics and Probability for Engineers*. John Wiley & Sons, Inc., United States of America, 3rd edition, 2003. 48

L. Mujica, J. Vehi, M. Ruiz, M. Verleysen, W. Staszewski, and K. Worden. Multivariate statistics process control for dimensionality reduction in structural assessment. *Mechanical Systems and Signal Processing*, 22: 155–171, 2008. 94

T. Naes, T. Isaksson, T. Fearn, and T. Davies. *A User-Friendly Guide to Multivariate Calibration and Classification*. NIR Publications, UK, 1996. 94, 96

M. Omar and Y. Zhou. A quantitative review of three flash thermography processing routines. *Infrared Physics & Technology*, 51:300–306, 2008. 6

B. Oswald-Tranta and S.M. Shepard. Comparison of pulse phase and thermographic signal reconstruction processing methods. In *Proc. of SPIE, Vol. 8705*, Baltimore, MA, 2013. 72

C. Pan and H. Hocheng. The anisotropic heat-affected zone in the laser grooving of fiber-reinforced composite material. *Journal of Materials Processing Technology*, 62:54–60, 1996. 32

S. V. Patankar. *Numerical Heat Transfer and Fluid Flow*. Taylor & Francis Group, New York, NY, 1st edition, 1980. xiv, 42, 45

M. Pilla, M. Klein, X. Maldague, and A. Salerno. New absolute contrast for pulsed thermography. In *QIRT*, Dubrovnik, 2002. 7, 73

N. Rajic. Principal component thermography for flaw contrast enhancement and flaw depth characterisation in composite structures. *Composite Structures*, 58:521–528, 2002. 101, 107

F.L. Rodriguez and V.P. Nicolau. Inverse heat transfer approach for ir image reconstruction: Application to thermal non-destructive evaluation. *Applied Thermal Engineering*, 33:109–118, 2012. 14, 37, 38

R. Rosipal and N. Kramer. Overview and recent advances in partial least squares. In *Proceedings of Statistical and Optimization Perspectives Workshop*, Bohinj, Slovenia, 2005. 96

S. Shepard. Advances in pulsed thermography. In *The International Society of Optical Engineering, Thermosense XXVIII*, Orlando, FL, 2001. 7, 75

S. Shepard, J. Lhota, B. Rubadeux, T. Ahmed, and D. Wang. Enhancement and reconstruction of thermographic ndt data. In *The International Society for Optical Engineering, Thermosense XXIX*, Orlando, FL, 2002. 75, 126

S. M. Shepard. Flash thermography of aerospace composites. In *IV Conferencia Panamericana de END*, Buenos Aires, 2007. 76

R. Siegel and J. Howell. *Thermal Radiation Heat Transfer*. Taylor and Francis, New York, 4th edition, 2002. xxi, 158

S.W.M. Sjostrom and L. Eriksson. Pls-regression: a basic tool of chemometrics. *Chemometrics and Intelligent Laboratory Systems*, 58:109–130, 2001. 96

M. Susa, C. Castanedo-Ibarra, and X. Maldague. Pulsed thermography applied on a complex structure sample: comparison and analysis of numerical and experimental results. In *IV Conferencia Panamericana de END*, Buenos Aires, Argentina, 2007. 28

S. Vallerand and X. Maldague. Defect characterization in pulsed thermography: a statistical method compared with kohonen and perceptron neural networks. *NDT&E International*, 5:307–315, 2000. 117

V. Vavilov. Thermal nondestructive testing: short history and state-of-art. In *QIRT92 - Eurotherm Series 27*, Paris, 1992. 2

V. Vavilov. Modelling thermal ndt problems. In *18th World Conference on Nondestructive Testing*, Durban, South Africa, 2012. 28

V. Vavilov, X. Maldague, B. Dufort, F. Robitaille, and J. Picard. Thermal nondestructive testing of carbon epoxy composites: detailed analysis and data processing. *NDT&E International*, 26:85–95, 1993. 28

J. Wang, J. Carson, M. North, and D. Cleland. A new approach to modelling the effective thermal conductivity of heterogeneous materials. *International Journal of Heat and Mass Transfer*, 49:3075–3083, 2006. 34

M. Weiser, M. Rollig, R. Arndt, and B. Erdmann. Development and test of a numerical model for pulse thermography in civil engineering. *Heat Mass Transfer*, 46:1419–1428, 2010. 28

S. Wold. Personal memories of the early pls development. *Chemometrics and Intelligent Laboratory Systems*, 58:83–84, 2001. 94

S. Wold, H. Martens, and H. Wold. The multivariate calibration problem in chemistry solved by the pls method. In *Proceedings of the Conference Matrix Pencils*, Heidelberg, Germany, 1984. 94

Appendix A

Fundamentals of Thermal Radiation

A.1 The nature of thermal radiation

The propagation of thermal radiation (as well as in visible light, ultraviolet and so on) can be described from two different points of view: as waves −more specifically as electromagnetic waves with specific frequency and energy− or consisting of massless energy parcels called *photons* (as predicted by *quantum-mechanics*). Neither point of view is able to describe completely all radiative phenomena that have been observed. It is, therefore, customary to use both concepts interchangeable. In general terms, radiative properties of liquid and solids (surfaces) are more easily predicted using electromagnetic wave theory, while radiative properties of gases are more conveniently obtained from quantum mechanics. However, as will be showed below, both concepts are linked each other.

All electromagnetic waves, or photons, are known to propagate through any medium at a high velocity. Since light is a part of the electromagnetic wave spectrum, this velocity is known as the *speed of light*, c. The speed of light depends on the medium through which it travels, and may be related to the speed of light in vacuum, c_o, by the formula:

$$c = \frac{c_o}{n} \tag{A.1}$$

where n is known as the refractive index of the medium (the speed of light in vacuum is also related to the vacuum permittivity ε_o and the vacuum permeability μ_o by $c = 1/\sqrt{\varepsilon_o \mu_o}$). By definition, the refractive index of vacuum is $n \equiv 1$. For most gases the refractive index is very close to unity, for example, air at room temperature has $n = 1.00029$ over the visible spectrum. Therefore, light propagates through gases nearly as fast

as through vacuum. Electromagnetic waves travel considerably slower through dielectrics (electric nonconductors), which have refractive indices between approximately 1.4 and 4, and they hardly penetrate at all into electrical conductors (metals) (Modest, 2003). Each wave may be identified by its frequency, ν (measured in $cycles/s = s^{-1} = Hz$); wavelength, λ (measured in $\mu m = 10^{-6}\ m$ or $nm = 10^{-9}\ m$); wavenumber, η (measured in cm^{-1}) or its angular frequency, ω (measured in $radian/s = s^{-1}$). All four quantities are related one to another by the following equation:

$$\nu = \frac{\omega}{2\pi} = \frac{c}{\lambda} = c\eta \tag{A.2}$$

Each wave or photon carries with it an amount of energy, e, determined from quantum mechanics as:

$$e = h\nu = \frac{hc}{\lambda} \tag{A.3}$$

where h is the Planck's constant. The physical quantities present in Equations (A.1)-(A.3) are listed in Table A.4.

The frequency of light does not change when light penetrates from one medium to another since the energy of photon must be conserved. On the other hand, wavelength and wavenumber do, depending on the values of the refractive index of two media. Sometimes electromagnetic waves are characterized in terms of the energy that photon carries, $h\nu$, using unit *electron volt* ($1\ eV = 1.6022$ x $10^{-19}\ J$). Thus, light with a photon energy (or frequency) of $a\ eV$ has a wavelength (in vacuum) of,

$$\lambda = \frac{hc_o}{h\nu}\nu\frac{(6.626\times10^{-34}Js)(2.998\times10^{8}m/s)}{a(1.6022\times10^{-19}J)} = \frac{a(1.240)}{1}\mu m \tag{A.4}$$

Since electromagnetic waves of vastly different wavelengths carry vastly different amount of energy, their behavior is often quit different. Depending on their behavior or occurrence, electromagnetic waves have been grouped into a number of different categories (classified according to the photon energy, frequency and wavelength) as shown in Figure A.1. The wavelength region of interest here is the thermal radiation band, which comprises the long-wave portion of the ultraviolet, the visible region from approximately 0.4 to 0.74 μm, and the infrared region from beyond the red end of the visible spectrum to approximately 1000 μm .

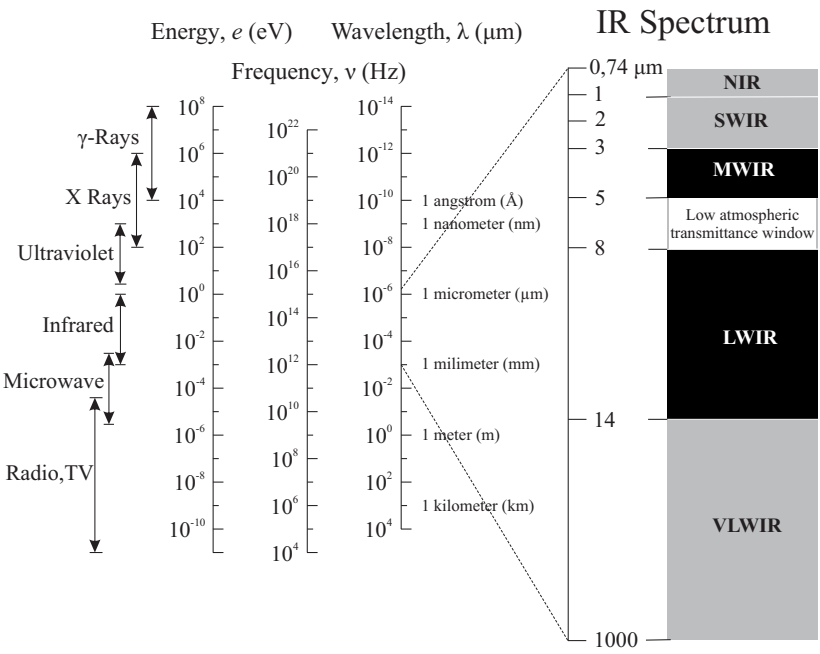

Figure A.1: Electromagnetic spectrum including the different infrared spectral bands. (Adapted from Ibarra-Castanedo et al., 2007b.)

The infrared spectrum can be further subdivided into five parts: near infrared (NIR) from 0.74 to 1 μm; short wavelength infrared (SWIR) from 1 to 3 μm; medium wavelength infrared (MWIR) from 3 to 5 μm; long wavelength infrared (LWIR) from 8 to 14 μm; and very long wavelength infrared (VLWIR) from 14 to 1000 μm. However, for infrared imaging, only two spectral ranges are typically defined: midwave region from 3 to 5 μm; and long-wave region from around 8 to 14 μm. Commercial cameras are available for these two ranges. The restrictions of these wavelength follows from considerations of the amount of thermal radiation to be expected, from the physics of the detector and from the transmission properties of the atmosphere.

A.2 Plank's Law

In thermography, the most important process is the so-called thermal radiation. The term *thermal radiation* implies that every body at a temperature $T > 0\ K$ ($-273.15\ ^oC$) emits infrared thermal radiation. The intensity of this radiation depends on wavelength λ and the body's temperature, phenomenon that il well-described by the Plank's law. It describes the spectral intensity of a perfect emitter (blackbody) as a function of the wavelength for a given temperature,

$$I_{\lambda,b}(\lambda,T) = \frac{2hc_o^2}{\lambda^5[\exp(hc_o/\lambda k_b T)-1]} \tag{A.5}$$

Since the blackbody is a diffuse emitter, its emissive power is given by:

$$E_{\lambda,b}(\lambda,T) = \pi I_{\lambda,b}(\lambda,T) = \frac{C_1}{\lambda^5[\exp(C_2/\lambda T)-1]} \tag{A.6}$$

being C_1 and C_2 the first and second radiation constants (see Table A.4 at the end of this section). Equation (A.6) is plotted for different temperatures in Figure A.2. Important features should be noted from this figures: the emitted radiation varies continuously with wavelength; at any wavelength the magnitude of the emitted radiation increases with increasing temperature and; the spectral region in which the radiation is concentrated depends on temperature, with comparatively more radiation appearing at shorter wavelengths as the temperature increases.

A.3 Stefan-Boltzmann Law

Integrating the emissive power [Eq. (A.6)] over all wavelengths, is obtained the total emissive power of blackbody E_b:

$$E_b(T) = \int_0^\infty E_{e,\lambda}(T)d\lambda = \frac{2k_b^4\pi^5}{15c_o^2h^3}T^4 = \sigma T^4 \tag{A.7}$$

where σ is the Stefan-Boltzmann constant. Thus, the total radiant flux emitted by a blackbody per unit surface element increases with the fourth power of temperature, which is known as the Stefan-Boltzmann law.

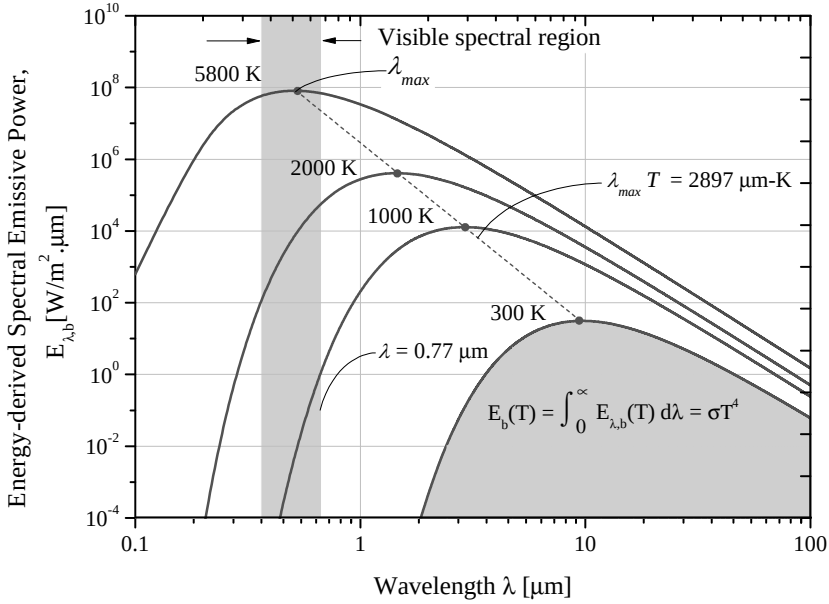

Figure A.2: Spectral energy-derived emissive power of a blackbody for different temperatures range.

A.4 Wien's Displacement Law

It can be noted from Figure A.2 that the blackbody spectral distribution has a maximum and that the corresponding wavelength λ_{max} depends on temperature. The nature of this dependence may be obtained by differentiating Eq. (A.6) with respect to λ and setting the result equal to zero, resulting in:

$$\lambda_{max} T = C_3 \tag{A.8}$$

being C_3 the third radiation constant (see Table A.4).

Equation (A.8) is known as the Wein displacement law. According to this result, the maximum spectral emissive power is displaced to shorter wavelengths with increasing temperature. With increasing temperature, shorter wavelengths become more prominent, until eventually significant emission occurs over the entire spectrum.

Table A.1: Radiation constants and values of physical quantities of interest. (Adapted from DeWitt and Nutter, 1988; Siegel and Howell, 2002).

Quantity	Symbol	Value	Units
Speed of light in vacuum	c_o	2.99792458×10^8	m/s
Permeability of vacuum	μ_o	$4\,\pi \times 10^{-7}$ $= 12.566370614 \times 10^{-7}$	N/A^2
Permittivity of vacuum	ε_o	$8.854187817 \times 10^{-12}$	F/m
Planck constant	h	6.626076×10^{-34}	$J{\cdot}s$
Boltzmann constant	k_b	1.380658×10^{-23}	J/K
Stefan-Boltzmann constant	σ	5.67051×10^{-8}	$W/(m^2{\cdot}K^4)$
Constant in Planck's spectral energy distribution, $C_1 = 2hc_o^2$	C_1	$1.1910439 \times 10^{-16}$	$W{\cdot}m^2$
Constant in Planck's spectral energy distribution, $C_2 = hc_o/K$	C_2	1.438769×10^4	$\mu m{\cdot}K$
Constant in Wien's displacement law	C_3	2897.7	$\mu m{\cdot}K$

Appendix B

Publications List

This research work has been the source of several scientific publications in both: journals and conference proceedings. Next paragraphs enumerate some of the main contributions published and under review:

- **Peer Reviewed Journal Papers:**

  Lopez, F., Ibarra-Castanedo C., Nicolau V. and Maldague X. P. Optimization of pulsed thermography inspection by partial-least squares regression, NDT&E International, v.66, p. 128-138, 2014.

  Lopez, F., Ibarra-Castanedo C., Maldague X. P. and Nicolau V. Pulsed thermography signal processing techniques based on the 1D solution of the heat equation applied to the inspection of laminated composites Materials Evaluation, v. 72, No. 1, p. 91-102, 2014.

  Lopez, F., Nicolau V., Ibarra-Castanedo C. and Maldague X. P. Thermal-numerical model and computational simulation of pulsed thermography inspection on carbon fiber reinforced composites, Submitted in January 2014 to International Journal of Thermal Sciences. Accepted for publication in June, 2014.

  Lopez F., Maldague X.P. and Ibarra-Castanedo C. Enhanced Image Processing for Infrared Non-destructive Testing, Review article submitted in April 2014 to Opto-Electronics Review. Currently in review process.

  Lopez, F., Nicolau, V.P. Inverse heat transfer approach for IR image reconstruction: application to thermal non-destructive evaluation, Applied Thermal Engineering, v. 33-34, p. 109-118, 2012.

- **Peer Reviewed Conferences Proceedings:**

  Lopez, F., Ibarra-Castanedo, C., Nicolau, V.P., Sfarra, S. and Maldague X. Comparative study of thermographic signal reconstruction and partial least-squares thermography for detection and evaluation of subsurface defects. In: 12th International Conference on Quantitative Infrared Thermography, Bordeaux, France. 2014.

  Bisson, P., Bortolin, A., Cadelano, G., Ferrarini, G., Lopez, F. and Maldague, X. Evaluation of frescoes detachments by partial least squares thermography. In: 12th International Conference on Quantitative Infrared Thermography, Bordeaux, France. 2014.

  Bisson, P., Bortolin, A., Cadelano, G., Ferrarini, G., Lopez, F. and Maldague, X. Comparison of image processing techniques for the on-site evaluation of damaged frescoes, SPIE - The International Society for Optical Engineering, Thermosense XXXVI, Baltimore, MD, 2014.

  Lopez, F., Ibarra-Castanedo, C., Nicolau, V.P. and Maldague X., Data Processing and Quantitative Methods in Pulsed Thermography, ASNT 23rd Research Symposium, Minneapolis, USA. March, 24-27, 2014.

  Lopez, F., Nicolau, V.P., Maldague X., and Ibarra-Castanedo C. Multivariate Signal Processing Technique by Partial-Least Squares Thermography, 16th International Symposium on Applied Electromagnetics and Mechanics (ISEM16), Quebec City (Quebec) Canada, July 31 - August 2, 2013.

  Lopez F., Ibarra-Castanedo C., Maldague X. P. and Nicolau V. Analysis of signal processing techniques in Pulsed Thermography, SPIE - The International Society for Optical Engineering, Thermosense XXXV, Baltimore, MD, April 29- May 3, 2013, Eds. Gregory R. Stockton and Fred P. Colbert, 8705:8705W.

  Lopez, F., Nicolau, V.P. and Maldague X. Pulsed Phase Thermography applied on complex structures: modeling and numerical analysis, Proceeding of 11th International Conference on Quantitative Infrared Thermography, paper number QIRT2012-260. Naples. Naples, Italy, June 11-14, 2012.

Lopez, F., Nicolau, V.P., Oshiro H., Tancredi, D. Non-destructive Evaluation of Composites Materials by Pulsed-Phase Thermography, Proceeding of 21st International Congress of Mechanical Engineering, paper number: COB25761. Natal, Brazil, October 24-28, 2011.

Lopez, F., Ferreira, J.P., Nicolau, V.P., Albertazzi, A., Willemann, D. Comparison of infrared thermography and shearography for non-destructive evaluation of composites materials by pulsed-heating excitation, 5th Conferencia Panamericana de Ensayos no Destructivos, Cancun, Mexico, October 2-6, 2011.